Stochastic Aspects of Crack Propagation: Experiments and Cohesive-zone Modeling

by

Fanbo Meng

A dissertation submitted in partial fulfillment
of the requirements for the degree of
Doctor of Philosophy
(Mechanical Engineering)
in the University of Michigan
2018

Doctoral Committee:

Professor Michael Thouless, Chair
Professor Jame Barber
Assistant Professor Neil Dasgupta
Professor Richard Robertson

Fanbo Meng

fanbo@umich.edu

ORCID iD: 0000-0003-4979-1344

I dedicate this thesis to my family for nurturing me with affections and love; to my fiancee for your constancy and sacrifice; to my friends for your support and encouragement.

ACKNOWLEDGMENTS

Foremost, I would like to express my heartfelt gratitude to my advisor Prof. Michael Thouless for the continuous support of my Ph.D study and research. This thesis would not have been possible without his help, motivation and patience. He set an excellent example as a research scientist to all the students with his earnest, preciseness and enthusiasm in research and his immense knowledge. It has been an honor to be his student.

I would like to thank to my committee members, Prof. James Barber, Prof. Richard Robertson and Prof. Neil Dasgupta, for their time, incisive questions and insightful comments. The three years' experience as a graduate student instructor in Prof. Thouless and Prof. Barber's solid mechanics class was enjoyable and invaluable in my academic life.

My sincere thanks to my collaborators Dr. Mark Nichols from Ford Motor Company and Dr. Jennifer David from Momentive Performance Materials, for the financial and technical support of my Ph.D study over these years.

I sincerely thank my family and my friends. I am grateful for all of your supports and encouragements over the years; and I sincerely believe these will keep supporting me throughout the rest of my life. A special thanks to my parents. Thank you for your endless amounts of love, and unimaginable sacrifices (even when I probably didn't deserve it). Thank you for always being there for me, listening to me rant and ramble over the phone. Thank you for everything.

TABLE OF CONTENTS

LIST OF FIGURES

LIST OF TABLES

LIST OF ABBREVIATIONS

AFM atomic-force microscopy

DCB double-cantilever beam

DIC digital-image-correlation

DMA dynamic-mechanical analysis

FIB focused ion-beam

LEFM linear-elastic fracture mechanics

SEM scanning-electron microscopy

ABSTRACT

Crack behaviors with stochastic characteristics have been studied in this dissertation. Kinetic crack growth is known as a thermally-activated process associated with statistical mechanics. Techniques to measure the relationship between crack velocity and energy-release rate for kinetic channeling cracks in thin films and coatings are presented in Chapter 2. The approach uses linear-elastic fracture mechanics to relate the crack spacing, material properties and geometry to the energy-release rate of a channeling crack, by means of detailed finite-element calculations. The velocities of individual cracks are monitored and related to their distance to nearest neighbors as part of these calculations. Other parameters that were identified as being important in determining the energy-release rate were the depth below the surface to which the crack penetrated, and the residual strain in the cracked layer. A technique to determine the crack depth was developed which involved focused-ion beam milling of the specimen, followed by electron microscopy. The residual strain in the crack layer was determined by measuring the crack-mouth opening using atomic-force microscopy, and comparing this to numerical analyses. These approaches were used to analyze a multi-layer system consisting of a polymeric, colloidal-silica nano-composite layer and a primer layer coating a polycarbonate substrate.

In Chapter 3, a stochastic cohesive-zone model has been developed in which the probability of a cohesive element breaking depends on the level of the work done against the tractions, above a equilibrium value. This concept has been used to model a kinetic crack growth using a cohesive-zone. Although the model was originally formulated in terms of

a discrete mesh size, it was shown that the results become mesh insensitive, and the cohesive length combining with a parameter associated with the activation energy becomes the characteristic dimension for the fracture. In particular, if the cohesive length is sufficiently small such that the requirements of linear-elastic fracture mechanics are satisfied, the cohesive-zone model gives an good representation of a classical kinetic-crack growth model controlled by the energy-release rate. A lower bond population in the cohesive-zone corresponds to a higher activation energy and a narrower region of bond rupture near the crack tip. Conversely, a low activation energy gives rise to a more diffused region of bond rupture, however, still much smaller than the cohesive length. The characteristics of crack behavior, in general, remains unchanged. However, for large cohesive-length scales, the crack advance is controlled by the cohesive strength rather than the energy-release rate.

A cohesive-zone model is demonstrated in Chapter 4 to explore the rate-dependent instabilities in crack growth in rubber-toughened polymers. Quasi-static crack growth was interrupted by stochastic occurrences of dynamic crack jumps, which was owing to a competition between the rate of toughening, driven by rubber cavitation, and the crack velocity. By coupling the classical void nucleation theory to a cohesive-zone model, in which the cohesive elements were allowed to make a re-selection of traction-separation law if a toughened mode was triggered, the crack exhibited similar behavior as that was experimentally observed. Under a displacement-controlled double-cantilever beam geometry, at low loading rates or high volume contents of rubber, fracture tended to progress in a stable fashion. As the loading rate was increased or the volume of rubber was reduced, the crack could suddenly become unstable and jump forward. Stochastic nature of crack behavior in this system was also captured, with a further assumption of spatial discrepancy in rubber content density.

CHAPTER 1

Introduction

The Griffith theory of brittle fracture states that crack growth occurs when the energy available to create unit area of new crack surface exceeds a critical value [1]. Specifically, the energy-release rate, or crack-driving force, defined as $\mathcal{G} = -\partial\Pi/\partial A$, where Π is the potential energy of the elastic body and A is the crack area, is the energy available to propagate a crack. The toughness, Γ, is defined as the energy consumed in creating unit area of crack surface under equilibrium conditions. If $\mathcal{G} > \Gamma$, it is thermodynamically possible for a crack to propagate. Conversely, if $\mathcal{G} < \Gamma$, it is thermodynamically possible for a crack to heal. In the framework of continuum linear elasticity, in a homogeneous solid the normal stress along the extension direction of a sharp crack is asymptotically in inverse proportion to the square root of distance from the crack tip, resulting in a singularity at the crack tip. The cohesive-zone model developed by Dugdale [2] and Barenblatt [3] eliminates this stress singularity by introducing a region in which the cohesive stress is activated, which is described as a function of the relative displacement of crack faces, commonly referred to as stress-displacement or traction-separation law. It has been proved that the cohesive-zone approach is equivalent to the Griffith theory in linear [4] and nonlinear[5, 6] materials, when the cohesive-zone is small enough comparing with other geometrical length scales.

In fracture models that follow the Griffith approach, there are two types of behavior: unstable and stable crack growth. Unstable behavior is typical with geometries under load control, for which the energy-release rate often increases with crack length. Under these conditions, fracture becomes unstable once the Griffith condition is met, and the crack propagates at dynamic speeds. Stable behavior can occur with geometries under displacement control, for which the energy-release rate often decreases with crack length. Under these conditions, it may be possible for equilibrium to be maintained, with quasi-static crack growth occurring at just the correct velocity to match the loading rate imposed by the displacement boundary conditions, but the Griffith theory itself does not imply any corre-

lation between the energy-release rate and crack velocity.

It is frequently observed experimentally that another condition exists where the cracks grow kinetically. This is characterized by a range of energy-release rates, $\mathcal{G}$, over which a crack can grow in a quasi-static fashion, with the crack velocity, v, being very sensitive to $\mathcal{G}$, but slow enough for dynamic effects to be ignored. This can occur because of time-dependent effects in the fracture process itself, or because of time-dependent effects in the material surrounding the crack-tip. If there is no significant time-dependence in the material surrounding a crack, quasi-static behavior can be modelled by introducing a phenomenological, velocity-dependent toughness, either from a continuum perspective [7, 8, 9, 10], or from a cohesive-zone perspective [11, 12]. If the material surrounding the crack has rate-dependent constitutive properties corresponding to creep, visco-elasticity or visco-plasticity [13, 14, 15, 16, 17, 18, 19, 20], fracture can't be modelled by a Griffith approach [21]. A length scale needs to be introduced into the fracture process. This can be done explicitly [13, 22, 23, 24, 25], or by a cohesive-zone [26], in which the cohesive strength becomes an additional fracture parameter that can be combined with the toughness to create a length scale.

A different type of time-dependent problem is related to thermally-activated, kinetic-crack growth [27]. They are typified by the observations of Weiderhorn and others on environmental effects, including temperature, on cracking in glass [28, 29, 30]. The time dependence of these phenomena arises from the interaction between a physical length scale associated with discrete possible positions for the crack-tip, an attempt frequency for crack advance, and the statistics of whether these attempts will be successful. The generalization of Griffith theory by Rice [31] laid the foundation for the analysis of this type of kinetic crack growth, in terms of crack-tip trapping by discrete energy barriers [32, 33]. These were built upon by Lawn [34, 35] with the aid of statistical mechanics, to produce a mathematical expression for the crack velocity as a function of energy-release rate and the aforementioned material properties. In this formulation, there exists a lower threshold, $\mathcal{G} = \Gamma_{\text{th}}$, corresponding to the condition that the rate of crack healing equals to the rate of extension at the crack tip. A quasi-equilibrium is maintained, resulting in a zero crack velocity. Above this threshold, the crack velocity is exceedingly sensitive to the energy-release rate, temperature and other environmental parameters (humidity, acidity etc.). As the energy-release rate increasing, the active environmental species are increasingly hard to keep up with the crack tip, and hence an upper threshold exists such that the mechanism is dominated by a transport process afterwards. There also exists a higher threshold at

$\mathcal{G} = \Gamma^+$, corresponding to dynamic crack growth. Even in the absence of environmental effects, the crack growth can be a time-dependent phenomenon as well since the bond rupture and pullout of molecules are also thermally-activated processes. A consensus is achieved between this kinetic model and the Griffith model by letting $\Gamma_{\text{th}} = \Gamma^+ = \Gamma$, showing that the classical Griffith theory actually gives a description to an ideal case that the kinetic portion of crack growth is negligible. Crack healing occurs when the energy-release rate is below Γ_{th}, which is beyond the scope of this dissertation.

The engineering systems consist of thin films or coatings bonded to a substrate has been widely used in various areas such as automotive and electronics industries. In these system, cracking induced by uniaxial tensile stress in the coating occurs by a mechanism know as channeling; this results in a series of parallel cracks propagating across the coating. The basic fracture mechanics for this problem in an elastic system is well understood. For example, for a single crack channeling across a coating on a tough substrate, if the crack has extended to a length that is much greater than the film thickness, the crack is channeling in a steady-state such that its energy-release rate is independent of crack length but only depends on the modulus, Poisson's ratio, toughness and thickness mismatches between the coating and substrate [36, 37]. Therefore, the crack propagates at a constant kinetic speed if the steady-state energy-release rate falls in the regime: $\Gamma_{\text{th}} < \mathcal{G} < \Gamma^+$. In contrast, for a freestanding sheet of coating, the energy-release rate increases with crack length and will exceed the upper boundary, Γ^+, when the crack reaches a critical size. Dynamic propagation occurs afterwards, leading to a catastrophic failure. Therefore, the understanding of the nature of time-dependent kinetic crack channeling is crucial for a coating/substrate system, especially for the reliability under prolonged service conditions. In Chapter 2, the behavior of channel cracks in a nano-composite coating on polycarbonate is explored in details. We developed a technique to measure crack velocities as a function of energy-release rate, which was in good agreement with Lawn's kinetic model. Therefore, material parameters associated with the fracture process could be estimated.

In regard to these experimental observations, a question may arise that if such a driving-force sensitive, time-dependent crack growth can be simulated by finite-element cohesive-zone models. Since the classical cohesive-zone analysis of fracture is in a framework of Griffith criterion [4, 5, 6], the crack growth rate is indefinite above the equilibrium state. Therefore, for the modeling of kinetic cracks, a probability based on statistical mechanics have to be introduced to the failure of cohesive elements, in order to manifest the time-dependence. Details are provided in Chapter 3. The model was originally formulated in

terms of a discrete mesh size, however it has been shown that the results become mesh insensitive, and the cohesive length combining with a parameter associated with the activation energy becomes the characteristic dimension for the fracture. In particular, if the cohesive length is sufficiently small comparing with geometrical length scales, such as crack length, the problems is controlled by singular stress field and the linear-elastic fracture mechanics (LEFM) requirements are satisfied. In this regime, the cohesive-zone model gives an good representation of a classical kinetic-crack growth model controlled by the energy-release rate. If the amount of bonds in the cohesive-zone is low, the bond-rupture activation energy is correspondingly high such that the bonds tend to break in a limited region near the crack tip. Conversely, a low activation energy gives rise to a more diffused region of bond rupture, however, still smaller than the cohesive length. For large cohesive-length scales, the crack advance is controlled by the cohesive strength rather than the energy-release rate. In this case, the cohesive-zone model provides some additional insight for a regime beyond the assumptions of the original kinetic model.

Kinetic crack growth is associated with accumulation of thermally-activated molecular-level crack tip jumps following the Boltzmann statistics. In fracture mechanics, other mechanisms associated with time or rate-dependent stochastic natures have also attracted the attention of the researchers, For example, crack growth in rubber-toughened polymers sometimes exhibits stochastically occurred instabilities. It is observed that in a double-cantilever beam (DCB) geometry, quasi-static crack growth can suddenly be interrupted by dynamic crack tip jumps [38, 39, 40, 41, 42], without any additional work applied to the system. Occurrences of these dynamic jumps are stochastically in general, but more likely to appear at higher loading rates or with lower rubber particle contents. The toughening mechanism in rubber-modified polymers is always attributed to rubber cavitation, and scanning-electron microscopy (SEM) examinations of fracture surface [43, 39, 42] indicate a sign of abrupt stop of cavitation when the dynamic fracture occurs. Since the void nucleation process is time-dependent, it is reasonable to attribute the two different types of crack behaviors to the competition between the toughening and cleavage in the volume of material near the crack tip, and a cohesive-zone model based on this assumption is developed in Chapter 4. In this model, we coupled the classical void nucleation theory to the cohesive-zone analysis, which allowed the element to calculate the current level of voiding, and accordingly, select between a toughened, associated with the quasi-static growth, and an untoughened, associated with the dynamic fracture, traction-separation laws. This model captured most important characteristics of crack behaviors in this system and by a further assumption of nonhomogeneity in the distribution of rubber particles in the polymer, the dynamic jumps

also exhibited stochasticity in its frequency.

CHAPTER 2

Kinetics of channeling cracks in nano-composite polymeric coatings

2.1 Introduction

The replacement of glass by transparent polymers, such as polycarbonates, has many advantages for automotive applications. Lower densities permit lighter-weight, energy-efficient structures. Alternative processing routes allow for more creative designs. There are, however, two major limitations with the use of polymers for automotive glazing. The first is their vulnerability to ultra-violet light, which can cause embrittlement and discoloration. The second is their relative softness, which results in them being very easy to scratch. Both of these limitations can be overcome by the application of nano-composite coatings containing a hard wear-resistant phase and ultra-violet absorbers. However, the intrinsic hardness of these coatings makes them vulnerable to failure by fracture over prolonged service conditions [44]. Therefore, it is of importance to explore the phenomenon of time-dependent fracture in nano-composite coatings on polymer substrates, which motivated the study presented in this chapter.

As described in Chapter 1, channeling crack can be induced by uniaxial tensile stresses in the coating. When a single steady-state crack channeling across a coating of thickness h_c on a very tough substrate of thickness H, and subjected to a uniform tensile strain of ε_o, the energy-release rate is of the form [36, 37]

$$\mathcal{G} = \varepsilon_o^2 \bar{E}_c h_c \; f_D\left(\tilde{\alpha}, \tilde{\beta}, h_c/H\right). \tag{2.1}$$

In this equation, $\bar{E}_c = E_c/(1-\nu_c^2)$, is the plane-strain Young's modulus of the coating, ν_c is Poisson's ratio, and $f_D\left(\tilde{\alpha}, \tilde{\beta}, h_c/H\right)$ is a function of the two Dundurs' parameters, $\tilde{\alpha}$ and $\tilde{\beta}$, which are measures of the elastic mismatch between the coating and substrate, and

the ratio of coating and substrate thicknesses. The Dundurs' parameters are given by [45]

$$\tilde{\alpha} = \frac{\bar{E}_c - \bar{E}_s}{\bar{E}_c + \bar{E}_s} \tag{2.2}$$

and

$$\tilde{\beta} = \frac{\bar{E}_c(1-\bar{\nu}_s) - \bar{E}_s(1-\bar{\nu}_c)}{2(\bar{E}_c + \bar{E}_s)} \tag{2.3}$$

where, $\bar{\nu}_c = \nu_c/(1-\nu_c)$ is the plane-strain Poisson's ratio for the coating, and $\bar{E}_s$ and $\bar{\nu}_s$ are the plane-strain modulus and the plane-strain Poisson's ratio, respectively, for the substrate. A single crack propagates if the energy-release rate exceeds the toughness of the coating, Γ_c. Additional cracks can grow at higher levels of the energy-release rate, forming patterns of parallel cracks. The density of the cracks increases with applied strain [46, 47, 48]; it also depends on the modulus ratio [49] and toughness [50] mismatch between the coating and substrate, and on the statistics of the initial flaw population [51].

A coating will remain crack-free during service, provided the value of the energy-release rate (Eqn. 2.1) is always less than the toughness of the coating. However, cracks can develop during service for a variety of reasons. A build up of stress could increase the energy-release rate. Degradation of the coating could decrease the toughness. Cyclic loading could result in sub-critical fatigue-crack initiation and growth. Stress-corrosion, creep, or visco-elastic effects could induce time-dependent crack growth. It is the time-dependent and fatigue aspects of the problem that were explored in this study.

Time-dependent crack growth can occur if the constraint on a coating is gradually relaxed by creep of the substrate, or of the primer layer [52, 53]. This is because both creep and visco-elastic relaxation lower the effective modulus of a material, and the energy-release rate for channeling in a coating increases with the compliance of the material beneath it [36]. For example, if one were to model the substrate as a standard-linear solid, one could consider two limiting values for its modulus [54]: a higher, unrelaxed modulus at short time scales, and a lower, relaxed modulus at long time scales. If the energy-release rate for channeling associated with the unrelaxed substrate modulus exceeds the coating toughness, Γ_c, spontaneous fracture occurs. If the energy-release rate for channeling associated with the relaxed substrate modulus is less than Γ_c, fracture will never occur. In between this range of energy-release rates, the crack will channel across the coating at a steady-state velocity associated with a time scale corresponding to the effective modulus that makes $\mathcal{G} = \Gamma_c$.

Time-dependent crack growth associated with visco-elastic effects in the coating itself would not seem to be possible, although it does occur in visco-elastic materials under load control. Under these conditions, a lower threshold for crack growth is associated with the fully-relaxed modulus of the coating, and an upper threshold for crack growth is associated with the unrelaxed modulus [26]. However, under the strain-controlled conditions of a visco-elastic coating bonded to an elastic substrate, the drop in modulus with time would not result in such behavior, as it would cause the energy-release rate to decrease with a drop in crack velocity.

Stress-corrosion cracking can cause time-dependent crack growth [28]. This has been shown to occur in silica-containing coatings [55] and in silicon-nitride films [56, 57]. It has also been shown to be an issue for delamination of silica-containing films [58, 59, 60]. Like visco-elastic crack growth, stress-corrosion cracking occurs within a limited range of energy-release rate. There is an upper threshold when the crack grows so quickly that there is no time for the crack tip to interact with the environment (such as water vapor). There is a lower threshold when the crack grows so slowly that the crack tip is essentially in equilibrium with the environment. corresponding to slow crack growth in which the environment (such as water vapor) can interact with the bonds at the crack tip, essentially lowering the toughness of the coating. Between these limits the crack velocity depends either on how quickly the environment can reach the crack tip, or on the rate of reaction between the environment and the atoms or molecules at the crack tip [61, 35]. There is also a higher threshold, corresponding to crack growth in a vacuum. Stress-corrosion cracking can be identified by any observed effect of the environment on crack velocity, and by the existence of these upper and lower thresholds.

Crack growth in solids is always associated with the rupture of bonds or the pullout of molecules. These are thermally-activated processes, so crack growth is inherently a time-dependent phenomenon, even in the absence of environmental effects. For example, while stress-corrosion cracking is a thermally-activated process, so is crack growth in a vacuum [29]. However, the activation energies and other parameters may not always be in a range for the time-dependent nature of crack growth to be manifested. A thermodynamic model of fracture has been developed by Lawn [34]; this relates the crack velocity, v, to the energy-release rate, $\mathcal{G}$, and the threshold toughness of the coating, Γ_{th}. In this model, the driving force for thermally-activated rupture at the crack tip is the difference between the energy-release rate and the intrinsic toughness of the material. At equilibrium, the

energy-release rate equals the toughness, and the rate of bond rupture equals the rate of bond healing, so no crack propagation occurs. This corresponds to a threshold energy-release rate for fracture. Above this threshold, the driving force for rupture increases, and the crack velocity increases exponentially with energy-release rate. Thermal-activation of rupture also results in an exponential increase in velocity with temperature. The crack velocity is given by

$$v = c_1 \exp\left(-Q/k_{\mathrm{B}}T\right) \sinh\left[c_2 \left(\mathcal{G} - \Gamma_{\mathrm{th}}\right)/k_{\mathrm{B}}T\right] , \tag{2.4}$$

where k_{B} is Boltzmann's constant, T is the absolute temperature, Q is the activation energy for the rupture process. The parameters c_1 and c_2 are related to the discrete increments of length over which rupture can occur, such as atomic spacing, both in the direction of crack advance and perpendicular to it. The parameter c_1 is given by $c_1 \approx k_{\mathrm{B}}Td_x/\pi\hbar$, where d_x is the characteristic length in the direction of crack growth and $\hbar$ is the Dirac constant. The parameter c_2 is given by $c_2 \approx d_x d_y/2$, where d_y is the characteristic length parallel to the crack tip. In the absence of environmental effects, this kinetic model exhibits only a lower threshold associated with equilibrium.

In this chapter, we explore channel cracking in a nano-composite coating on polycarbonate. Empirical observations had shown that exposure to service conditions resulted in the formation of such cracks after a period of time. This provided the original motivation behind the study: to try and elucidate what might be the nature of any time-dependent crack growth. Therefore, we developed a technique, based on fracture mechanics, to measure crack velocities as a function of energy-release rate in coatings. We showed that the crack velocity had the form expected from Lawn's kinetic model, for which we could obtain material parameters associated with the fracture process. From a practical perspective, we also demonstrated that there was no fatigue or stress-corrosion cracking in the particular system described in this study.

2.2 Experiments

2.2.1 Material properties

Clear polycarbonate sheets with a thickness of 3.0 ± 0.02 mm were coated with a thermally-cured, silicone topcoat (or hardcoat) on a polyacrylate-based primer (Fig. 2.1). The topcoat was filled with colloidal silica, and had a thickness of 6.1 ± 0.6 µm; the primer had a thickness of 1.4 ± 0.4 µm.

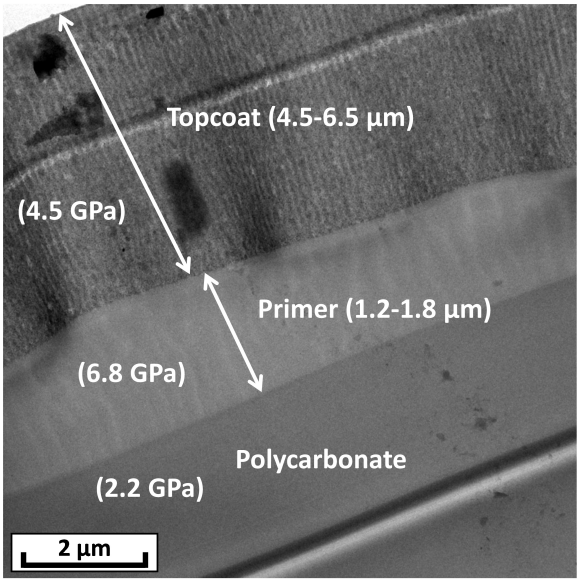

Figure 2.1: The system studied in this chapter consists of a polycarbonate substrate, a polyacrylate-type primer, and a silicone topcoat containing colloidal silica.

Single layers of the topcoat and primer were coated on polished, 16-gauge, brass discs to measure the temperature-dependent mechanical properties of the layers. Brass was used to ensure good thermal transfer between the heating stage and the material being tested. The fabrication procedures for these specimens were identical to those used for preparing coatings on the polycarbonate substrates, but the thickness of each coating was approximately 6 µm, to facilitate the measurements. Dynamic indentation tests were performed using a Hysitron TI 950 TriboIndenter^{TM} with a diamond Berkovich probe, at testing depths of approximately 5% of the layer thicknesses. The measurements were conducted at frequencies of 10 Hz and 200 Hz, over a temperature range of 25 °C to 120 °C. The resultant values for the storage modulus and loss tangent of both layers are given in Fig. 2.2.

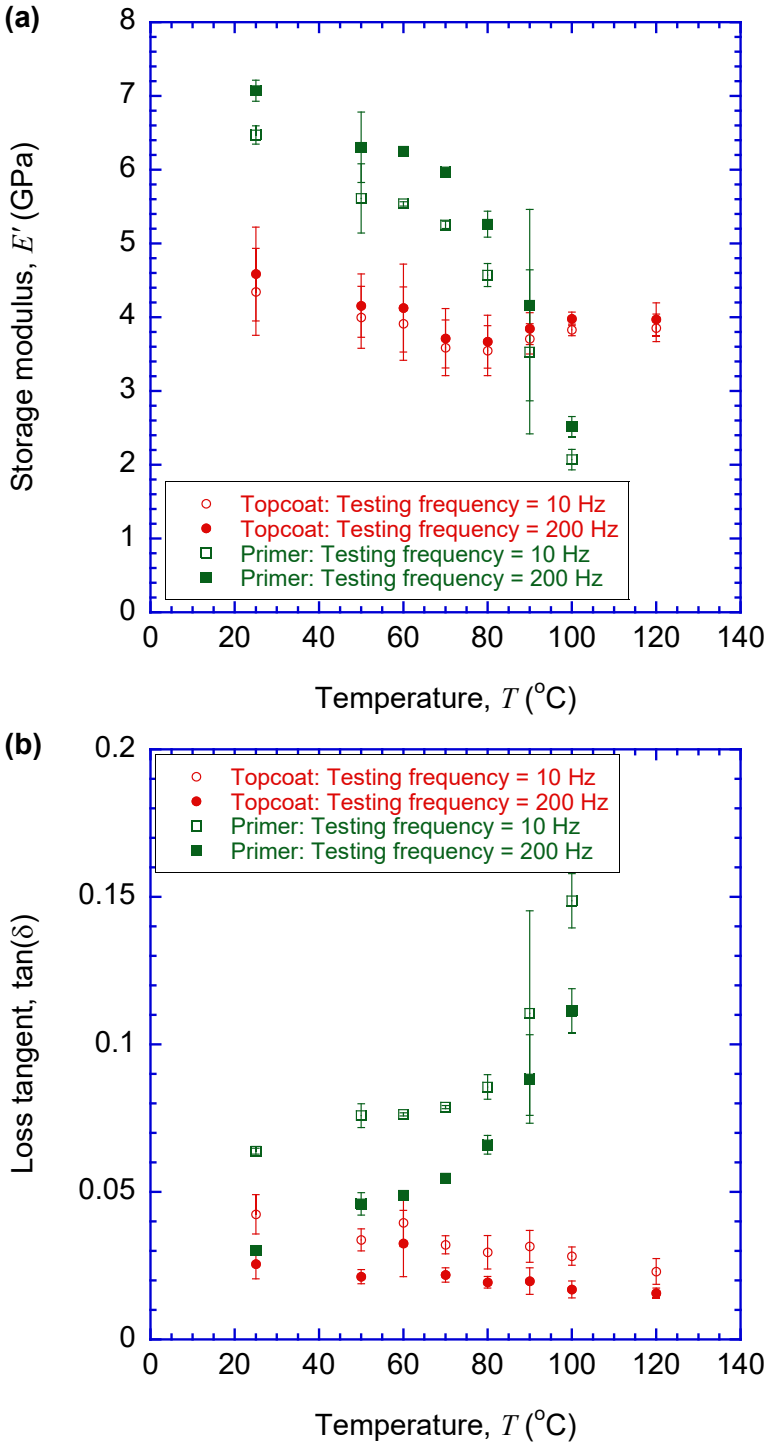

Figure 2.2: Dynamic indentation temperature sweeps for the topcoat and primer: **(a)** storage modulus, and **(b)** loss tangent. The glass-transition temperature of the primer is about 90 °C, in this frequency range. The glass-transition temperature for the topcoat appears to be at least higher than 130 °C.

The temperature-dependent properties of the substrate were measured by dynamic-mechanical analysis (DMA), using a TA Instruments® RSA3 solid analyzer. A sinusoidal compressive load at a frequency of 1 Hz was applied to an uncoated substrate, inducing compressive strains between 0.8% and 0.1%. The loss modulus, the storage modulus, and the loss tangent corresponding to this frequency are presented in Fig. 2.3 for a range of temperatures up to 150 °C.

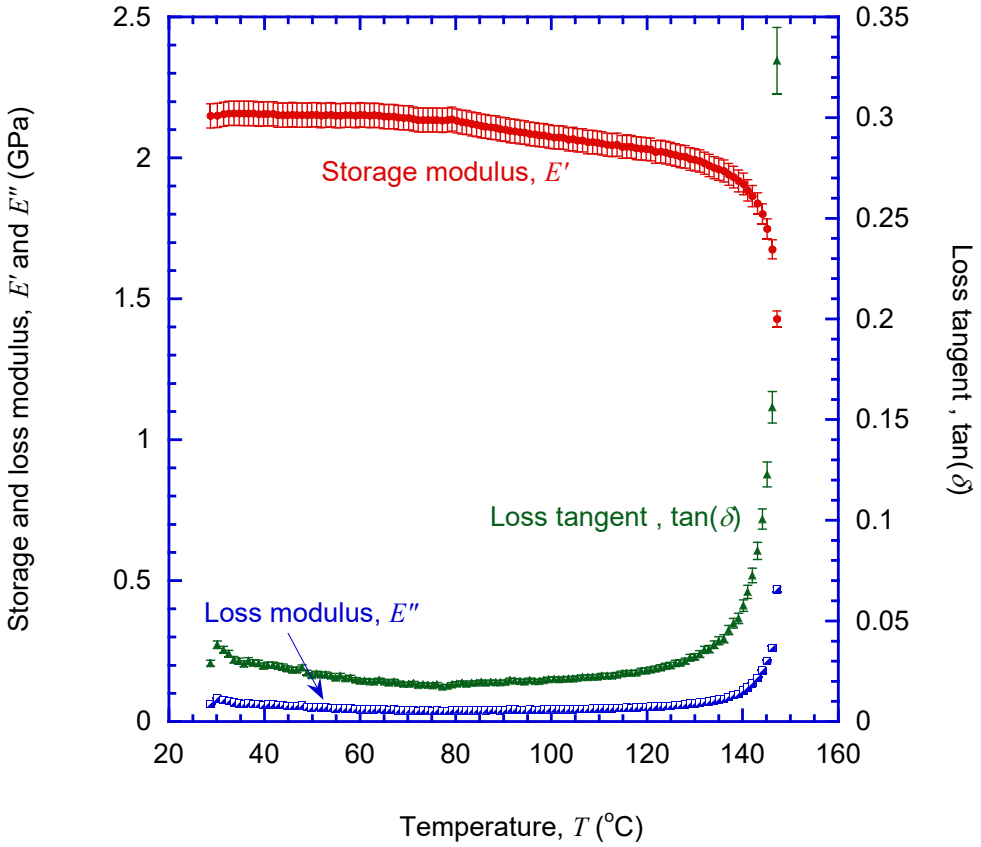

Figure 2.3: Typical temperature sweep at a frequency of 1 Hz for the polycarbonate substrate. The storage modulus, loss modulus and loss tangent exhibited a limited temperature dependence below 135 °C. Above this temperature, there was a dramatic decrease in the storage modulus, and a corresponding increase in the loss modulus and loss tangent.

2.2.2 Crack velocity

The coated sheets of polycarbonate were cut into 22 mm $\times$ 155 mm rectangular sections, and the cut edges were milled. An MTS 858 Bionix II tensile machine was used to apply a uniaxial tensile strain in the range of 0.75% to 1.65%. The strain was applied at different nominal strain rates over the range of 0.5×10^{-4} s^{-1} to 2×10^{-4} s^{-1}, and then held at different levels while crack growth occurred. The experiments were conducted at temperatures of 25 ± 2 °C, 48 ± 2 °C, 65 ± 3 °C and 89 ± 3 °C, at ambient relative humidity (which varied from 16% to 33%). An additional set of experiments was conducted to investigate the effects of humidity at room temperature, using three different humidities of $19 \pm 3\%$, $29 \pm 4\%$ and $61 \pm 4\%$. No obvious effects of humidity were observed from these experiments.

A series of optical micrographs were taken during the course of the experiments, both during the loading process, and while the strain was held constant. The strains in the coatings were determined by digital-image-correlation (DIC), with the relative displacement of markers on the surfaces of the coatings being analyzed using a commercial software package (MetaMorph®). The crack spacings were measured from the optical images. The crack velocities were determined by measuring the changes in position of crack tips as a function of time. The crack velocities for a given crack were fairly constant, although some minor variations were observed that probably corresponded to local changes in the thickness of the topcoat.

Examples of the type of images used for the optical measurements are given in Fig. 2.4. In this figure, two cracks can be seen propagating in opposite directions between two established cracks. The energy-release rate, and hence the crack speed, depends on the distance of a propagating crack from its nearest neighbors. For a given level of applied strain, the energy-release rate is higher when the spacing is larger, as discussed in Section 2.3. In the example shown in Fig. 2.4, the cracks slowed down after the tips of the propagating cracks passed one another, because their own interactions formed a new nearest-neighbor spacing.

Cyclic loading may cause cracks to propagate by fatigue. However, to verify fatigue, the effects of kinetic growth need to be deconvoluted from any possible fatigue growth. To do this, one needs to determine whether the crack velocity under cyclic conditions is faster than would be expected by merely integrating the kinetic contribution to crack growth, and whether there is any effect of frequency on the velocity. Possible effects of fatigue were investigated by measuring the crack velocities while cycling the specimen under zero-to-

tension conditions at 1 Hz, 2 Hz and 5 Hz with mean strains of $0.97 \pm 0.03\%$ at 24 ± 1 °C. The crack velocities observed in these experiments were compared to the crack velocities measured in the static experiments at a corresponding level of average strain. No effect of fatigue greater than the level of the experimental uncertainties was found for these samples.

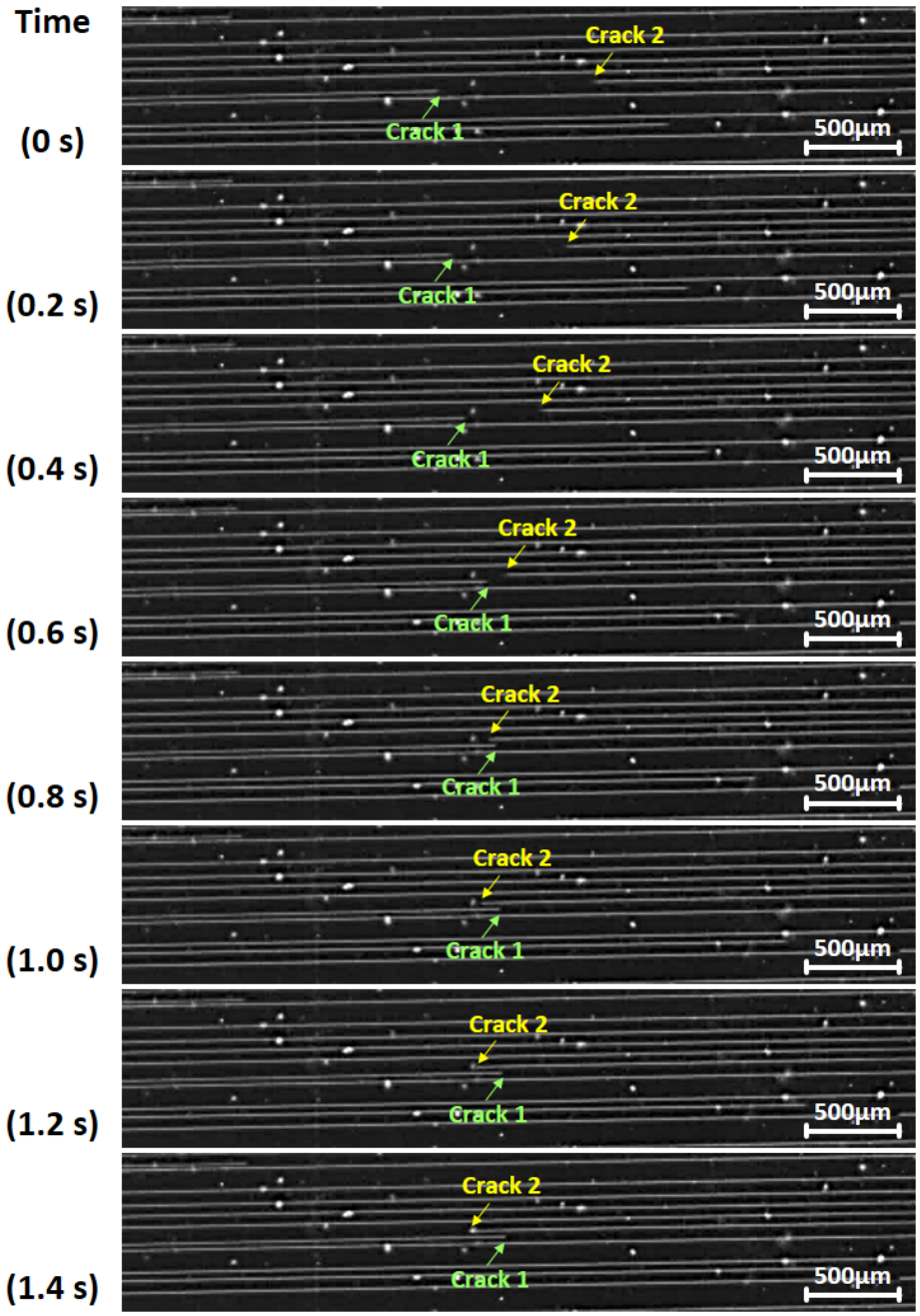

Figure 2.4: A sequence of images at 0.2 s intervals for two cracks (with tips labeled "1" and "2") propagating between two existing cracks. The energy-release rate depends on the distance of a propagating crack from its two nearest neighbors. For a given level of effective strain, the energy-release rate (and crack velocity) is higher when the spacing is larger. It can be seen that the two cracks slowed down after they passed each other, because their own interaction formed new nearest neighbors for each of them. This figure was taken at an applied strain of 1.58%.

2.2.3 Crack depth

The energy-release rate for channeling depends on the crack depth. Therefore, it is important to know whether the cracks penetrate beyond the topcoat, into the primer or substrate. The crack depth was found by using a focused Ga-ion beam (5.0 kV voltage and 0.4 nA) to make cross-sections through cracked portions of the coating, and examining the section by SEM. An example of a resulting image is shown in Fig. 2.5 for a specimen with a 6.3 μm thick topcoat and a 1.4 μm thick primer. This image clearly shows that the channeling crack terminated at the interface between the topcoat and primer. This observation was consistent between several such sections. It should also be noted that the observation that the crack does not extend into the primer is consistent with the predictions of LEFM [36], in that the modulus of the topcoat is slightly lower than that of the primer.

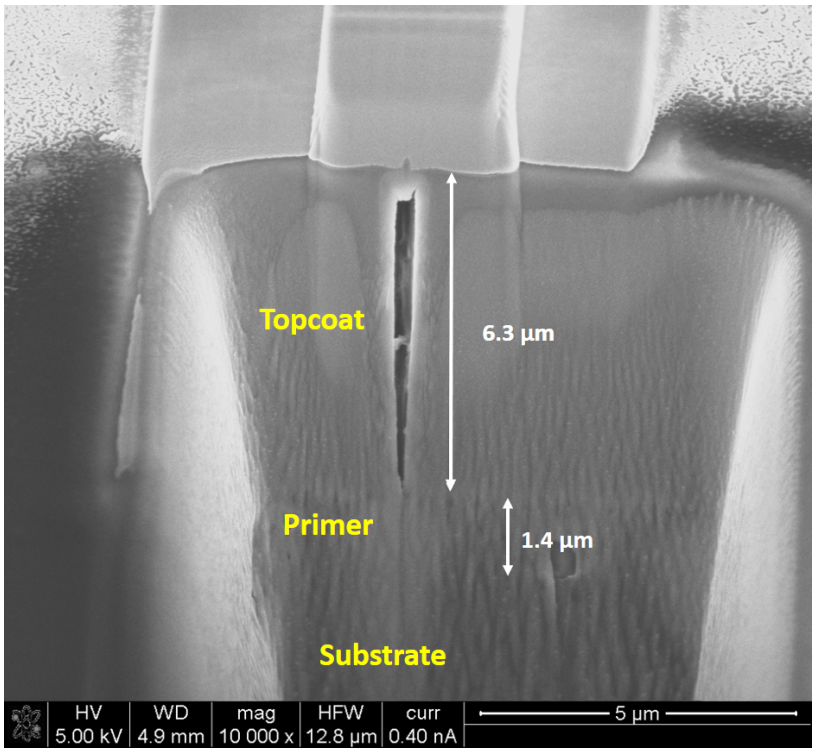

Figure 2.5: A scanning-electron micrograph of a channeling crack formed at room temperature, taken in cross-section from a sample with a 6.3 μm topcoat and a 1.4 μm primer in thickness. This image shows that the channeling cracks terminated at the interface between the topcoat and primer.

2.2.4 Residual tension

Accurate calculations for the energy-release rate of channeling cracks requires a knowledge of the residual strain in the coating caused by the initial curing and processing. This was estimated at room temperature by using atomic-force microscopy (AFM) to measure residual crack openings at the surface of the coating, after the applied strain had been removed. Samples were examined with a Bruker© Multimode AFM equipped with a Nanoscope® V controller in tapping mode, using TESP tips. An example of the experimental results is shown in Fig. 2.6. The AFM trace corresponds to a line across the middle crack in a set of three (identified as crack "2" in Fig. 2.6(a)). It should be noted that the crack opening can be measured quite accurately by AFM, but the crack profile shown in Fig. 2.6(b) is not accurate, because of the finite size of the AFM tip. The crack is relatively narrow, and the AFM tip cannot penetrate very far into the crack. However, this doesn't matter because it is only the crack-mouth opening that is used to deduce the residual tension.

In addition to the crack opening, the distance to each neighboring crack was measured. These values were used as parameters in a plane-strain, finite-element model, using the appropriate elastic properties of the system, and assuming the three cracks penetrated to the interface between the topcoat and primer. The residual strain at room temperature was then deduced by calculating what strain would be required to match the finite-element results to the measured crack opening.

The opening of crack "2", shown in Fig. 2.6, was 98 nm. The finite-element calculations indicated that this opening for a crack, situated as it was between its two nearest neighbors, corresponded to a residual strain of 0.24%. The experiments and analyses were repeated for five different specimens loaded between 1.0% and 1.4%. There was no effect of applied strain on the calculated residual strain. This implies that the system was elastic, and that the crack opening was caused by residual strain, rather than plasticity. This residual strain was determined to be $0.22 \pm 0.02\%$ at room temperature.

For the tests conducted at elevated temperatures, the mismatch in thermal expansion between the substrate and the topcoat provides an additional component to the residual strain. The thermal-expansion coefficient of the polycarbonate substrate is 67.5×10^{-6} °C^{-1}, as given in the datasheet [62]. The thermal-expansion coefficient of the topcoat was determined using a Toho Technology FLX2320-S system to measure how the curvatures of 500 ± 25 μm thick, fused-quartz wafers coated with the topcoat varied with temperature, over the range 25 °C to 130 °C. The thickness of the topcoat in these experiments

was 5.4 ± 0.1 μm. The thermal-expansion coefficient of fused quartz was assumed to be 5.5×10^{-7} °C $^{-1}$, resulting in a measured thermal-expansion coefficient for the topcoat of $32.1 \pm 1.1 \times 10^{-6}$ °C $^{-1}$. Neither the residual stresses nor the thermal expansion of the primer affect the mechanics of the problem, since the substrate was relatively thick and the cracks terminated at the interface between the primer and topcoat.

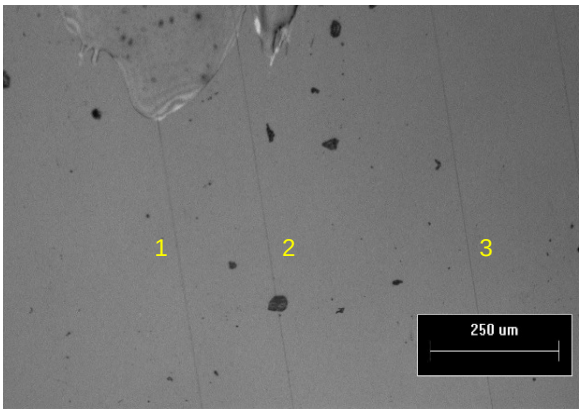

(a)

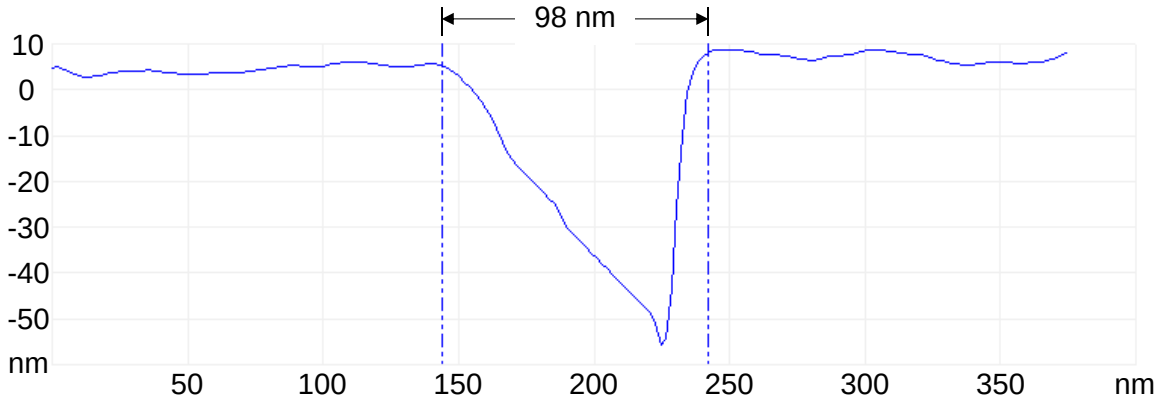

(b)

Figure 2.6: **(a)** Three cracks were selected for analysis from a sample that had been strained to 1.03 %. The distances from the central crack to its nearest neighbors were measured, and used as parameters for the numerical model shown in Fig. 2.8. **(b)** The opening at the surface of the topcoat of the center crack labelled as "2" was measured by AFM to be 98 nm. The numerical analysis then indicated that the residual strain that would result in such an opening is $0.24 \pm 0.02\%$.

2.3 Numerical analysis

The experimental data for crack growth consisted of crack velocities measured as a function of effective strain and the distance between the two nearest neighbors. To convert these data to plots of crack velocity against energy-release rate required finite-element calculations for the energy-release rates at the tips of the growing cracks. These calculations were conducted using the measured distances to the nearest neighbors, the specific geometry and material properties of the system, and an assumption of linear elasticity.

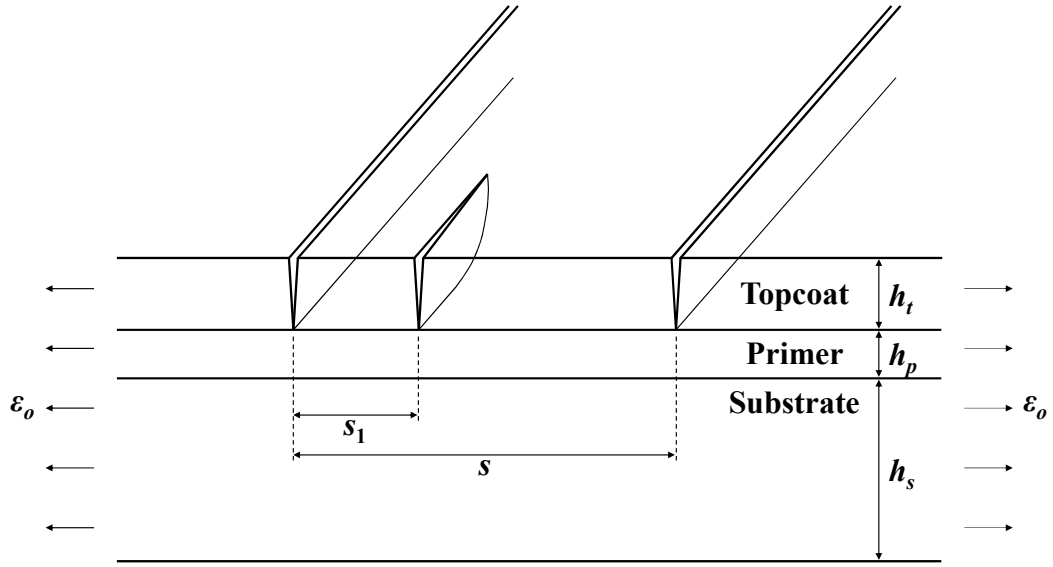

Figure 2.7: A schematic of the problem discussed in this chapter. The system has three layers with two thin films (called topcoat and primer in this chapter) on top of a substrate. A crack propagates in the topcoat between two pre-existing cracks, under an effective tensile strain of ε_o, which consists of strain applied to the substrate plus an additional residual strain within the topcoat. The two pre-existing cracks are at a distance of s apart, and the distance between the channeling crack and its closest neighbor is s_1.

A schematic illustration of the geometry assumed for this problem is shown in Fig. 2.7. There are three elastic layers: a topcoat of thickness h_t and plane-stress modulus E_t, a primer of thickness h_p and plane-stress modulus E_p, and a substrate of thickness h_s and plane-stress modulus E_s. A crack channels between two pre-existing flaws separated by a distance s, under an effective strain of ε_o, arising from both the residual tension and the applied strain. The propagating crack is located at a distance s_1 from its nearest neighbor. We made a further assumption that only the distances to the nearest neighbor on each side

are important, and that the cracks are long enough to be propagating under steady-state conditions. Under these conditions, the energy-release rate can be calculated from a 2-D finite-element calculation, following the approach given in Refs. [36, 50]. The commercial finite-element program ABAQUS was used. Plane-strain elements were used, with a mesh-sensitivity analysis being performed to ensure that any numerical uncertainties were smaller than experimental uncertainties. The ratio of h_t/h_p was set to 4.37, and the ratio of h_t/h_s was set to 0.0020, to be consistent with the experimental geometry. The ratio of E_t/E_p was set to 0.66, and the ratio of E_t/E_s was set to 2.05. The Poisson's ratio for all three layers was set to a value of 0.37, which is the Poisson's ratio of the polycarbonate sheet given in [62].

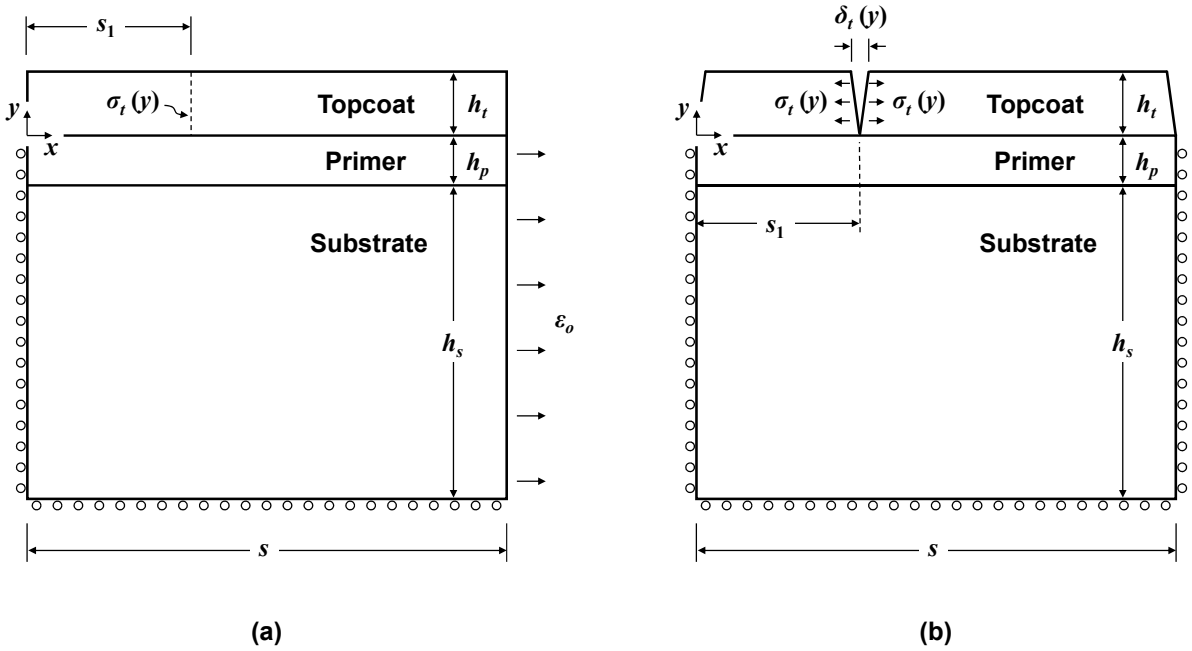

Figure 2.8: Energy-release rate of crack between two neighbors can be calculated by comparing the change in strain energy of a segment of the system as a crack passes through it. Specifically, the calculation was done by **(a)** calculating the stress $\sigma_t(y)$ in the uncracked topcoat system at the location where the crack propagates and **(b)** computing the crack-opening, $\delta_t(y)$, after the crack has passed through this plane, by applying the stress distribution obtained in (a) but in opposite direction on the crack surface.

The first step in determining the energy-release rate for channeling was to calculate the stress distribution through the thickness of the topcoat, at the location where the intermediate crack propagates (Fig. 2.8(a)). Examples of how this stress varies through the thickness of the topcoat are shown in Fig. 2.9 for different values of s_1/h_t, and for a fixed value of

$s_1/s = 0.5$, corresponding to the mid-point between two pre-existing cracks. When the crack spacing is large enough, the stress distribution is approximately uniform. As s_1/h_t decreases, the stresses decrease, and become more non-uniform, even becoming negative on the surface in the extreme case of $s/h_t = 1$, owing to bending.

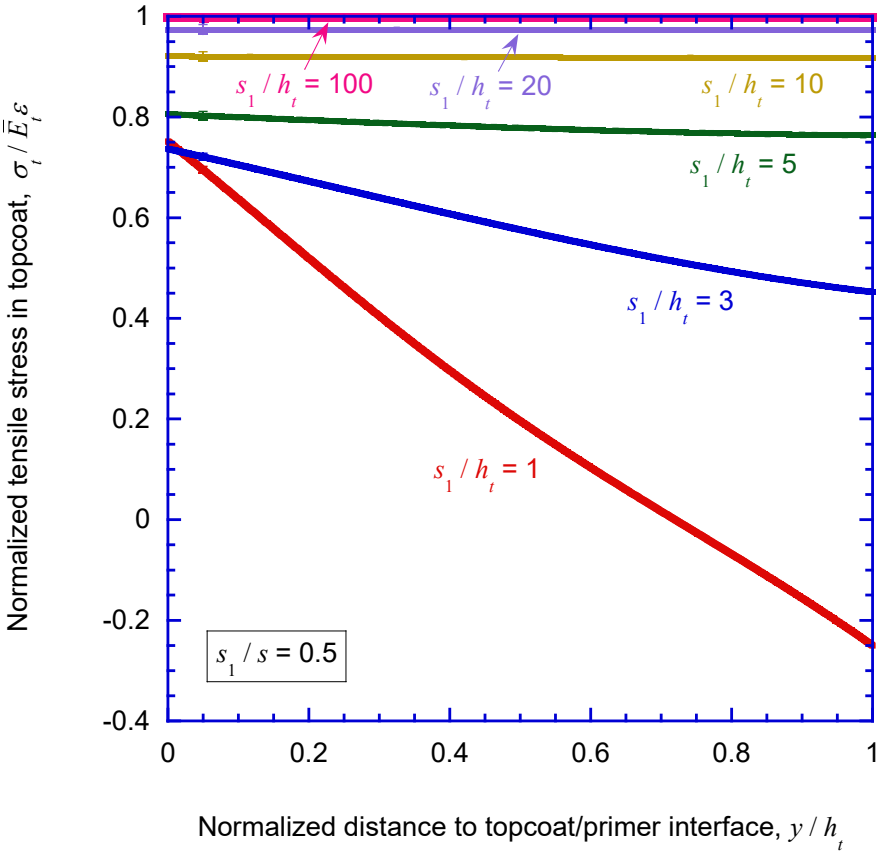

Figure 2.9: The stress in the film as a function of distance from the interface between the topcoat and primer interface to the free surface. The stresses have been plotted for a fixed value of the ratio $s_1/s = 0.5$, but for different values of s_1/h_t. The stresses have been normalized by the product of the plane-strain modulus of the topcoat ($\bar{E}_t$) and the effective strain in the topcoat of ε_o. The other non-dimensional geometrical and material parameters in these calculations were set to $E_t/E_p = 0.66$, $E_t/E_s = 2.05$, $h_t/h_p = 4.37$, $h_t/h_s = 0.0020$, and $\nu = 0.37$ for all three layers.

The second step in determining the energy-release rate for channeling was to compute the crack-opening displacement, $\delta_t(y)$, for a crack located at $x = s_1$ (Fig. 2.8(b)). The

energy-release rate for channeling was then calculated from

$$\mathcal{G} = \frac{1}{2h_t} \int_0^{h_t} \sigma_t(y)\delta_t(y)dy \ . \tag{2.5}$$

This results in a non-dimensional expression for the energy-release rate of the form,

$$\frac{2\mathcal{G}}{\pi\varepsilon_o^2 \bar{E}_t h_t} = g\left(\tilde{\alpha}_t, \tilde{\beta}_t, \tilde{\alpha}_p, \tilde{\beta}_p, \frac{h_t}{h_p}, \frac{h_t}{h_s}, \frac{s}{h_t}, \frac{s_1}{s}, \right) \ . \tag{2.6}$$

where $\tilde{\alpha}_t$, $\tilde{\beta}_t$, $\tilde{\alpha}_p$, and $\tilde{\beta}_p$ are the two Dundurs' parameters for the topcoat and for the primer relative to the substrate, respectively.

Figure 2.10 illustrates how the energy-release rate varies with the crack spacing (s_1/s and s/h_t), for a set of material and geometrical properties corresponding to the current system of interest. These results were used to analyze the experiments. Every crack for which the velocity had been measured was identified by three parameters: the separation of its two nearest neighbors, s, the distance to its closest neighbor, s_1, and the effective strain, ε_o, calculated from the measured applied strain and the estimated residual strain. From these three parameters, the energy-release rate was obtained from calculations similar to those presented in Fig. 2.10, and identified with the corresponding crack velocity. Details of these results are presented in Section 2.4.

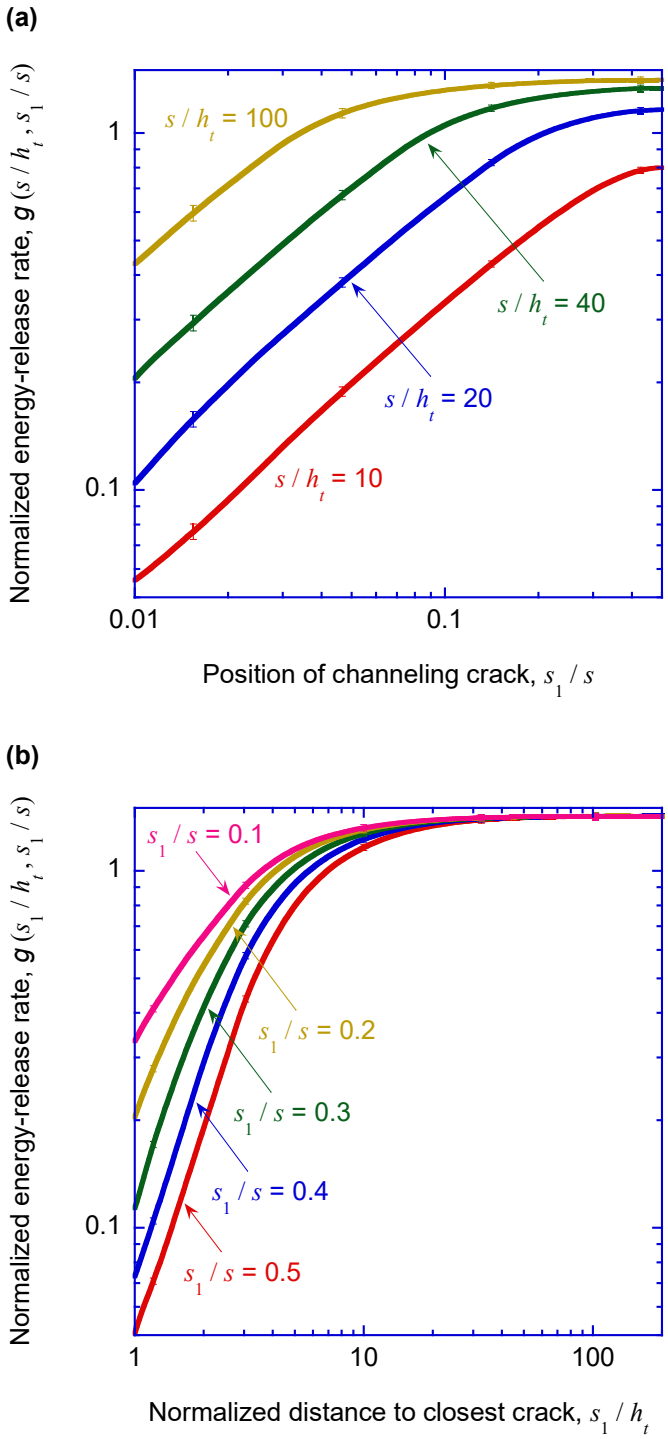

Figure 2.10: **(a)** As expected, the energy-release rate is highest when the crack propagates at the mid-point between its two neighbors ($s_1/s = 0.5$). **(b)** If s_1/h_t is greater than about 20, the energy-release rate is equal to that of an isolated crack channeling across the film, and independent of the crack spacing s_1/s. However, for values of s_1/h_t less than about 10, the energy-release rate is very sensitive to the spacing, and accurate interpretation of the experimental data requires the spacing to be known reasonably accurately.

2.4 Results and discussion

The experimental observations and finite-element calculations described above were used to produce plots relating the crack velocity to the energy-release rate. The appropriate storage moduli for the coatings and the substrate (as given in Figs. 2.2 and 2.3) and the effects of thermal expansion (Section 2.2.1), at the temperature of each test, were included in the calculations. The results are summarized in Figs. 2.12 and 2.11. These figures show the effects of humidity (Fig. 2.11) and temperature (Fig. 2.12). The data were collected from 62 cracks on 14 samples at applied true strains ranging from $0.75\% \pm 0.03\%$ to $1.65\% \pm 0.05\%$. All the cracks had lengths that were more than 50 times greater than the topcoat thickness, so the assumptions of steady-state were met. As can be seen from Fig. 2.12, the threshold energy-release rate for channel cracking was 6.6 ± 0.8 J/m^2 at room temperature, with a lowest recorded velocity of 3.0 nm/s.

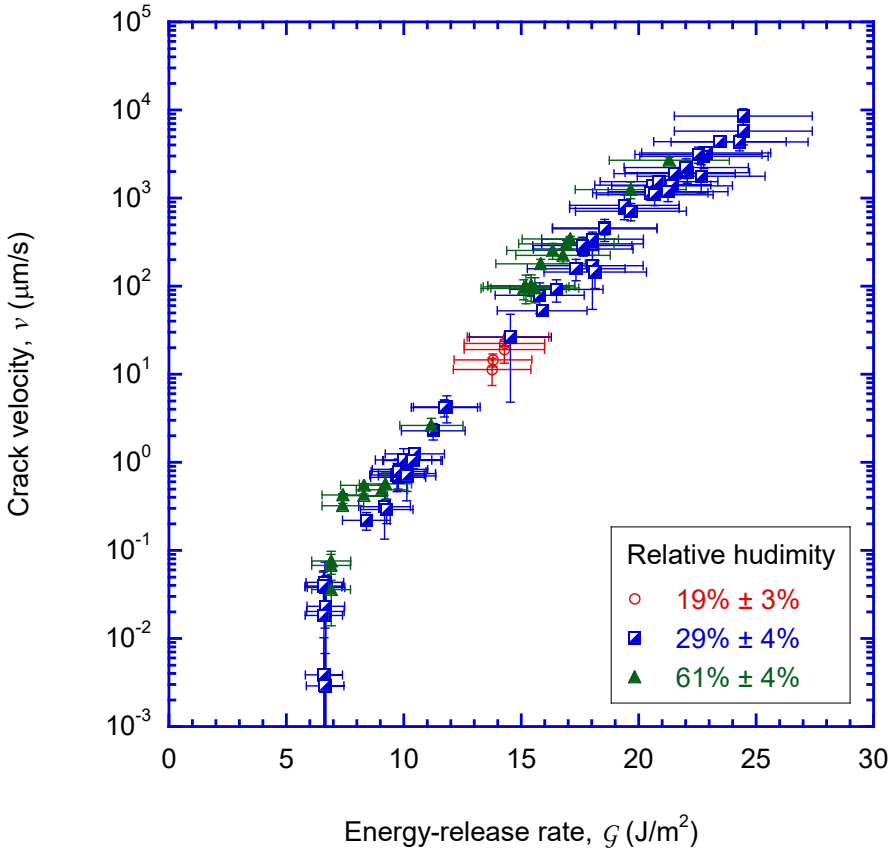

Figure 2.11: The crack velocity - energy-release rate curves at room temperature of 25 ± 2 ^{o}C, and relative humidities of $19 \pm 3\%$, $29 \pm 4\%$ and $61 \pm 4\%$. Within the uncertainties of the experiment, there were no obvious discrepancies between these curves, showing that in this range, the relative humidity did not have a significant effect on the crack velocity.

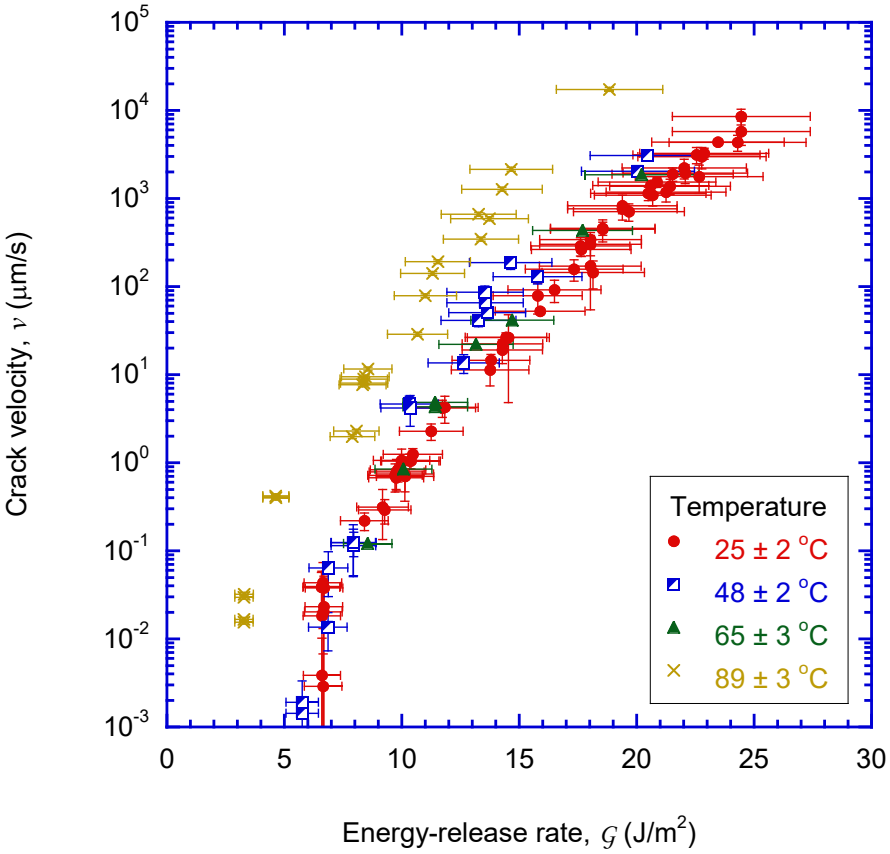

Figure 2.12: The results of the finite-element calculations (Section 2.3) were used with the experimental observations of crack spacing and velocity described in Section 2.2.2 to construct a graph of how the crack velocity depends on energy-release rate at temperatures of 25 ± 2 °C, 48 ± 2 °C, 65 ± 3 °C and 89 ± 3 °C. The relative humidity varied between 16% and 33%.

Figure 2.11 shows that the effects of humidity were negligible in this system over the range of the experiments studied. Figure 2.12 indicates that there was not a strong effect of temperature up to 65 ± 3 °C. However, the crack velocity appeared to be higher for the test at 89 ± 3 °C with the difference being more significant at higher energy-release rates. A slight decrease in the threshold energy-release rate was also observed at the highest temperature. The trends shown by these high-temperature data continued in few exploratory and unreported experiments conducted at 105 °C.

The nano-indentation DMA results of Fig. 2.2 indicate that the glass-transition temperature of the primer is about 90 °C. Therefore, at higher temperatures, it is possible that creep of the primer layer provides additional relaxation of the stresses when the topcoat cracks. This could increase the energy-release rate for channeling [52, 53] and, hence, in-

crease the crack velocity for a given applied strain. In addition, Figure 2.13 shows that the cracks penetrated into the primer when tests were conducted at high temperatures. This is consistent with a drop in the modulus of the primer, and would also provide an additional contribution to the energy-release rate that was not included in the calculations used to generate the results of Fig. 2.12.

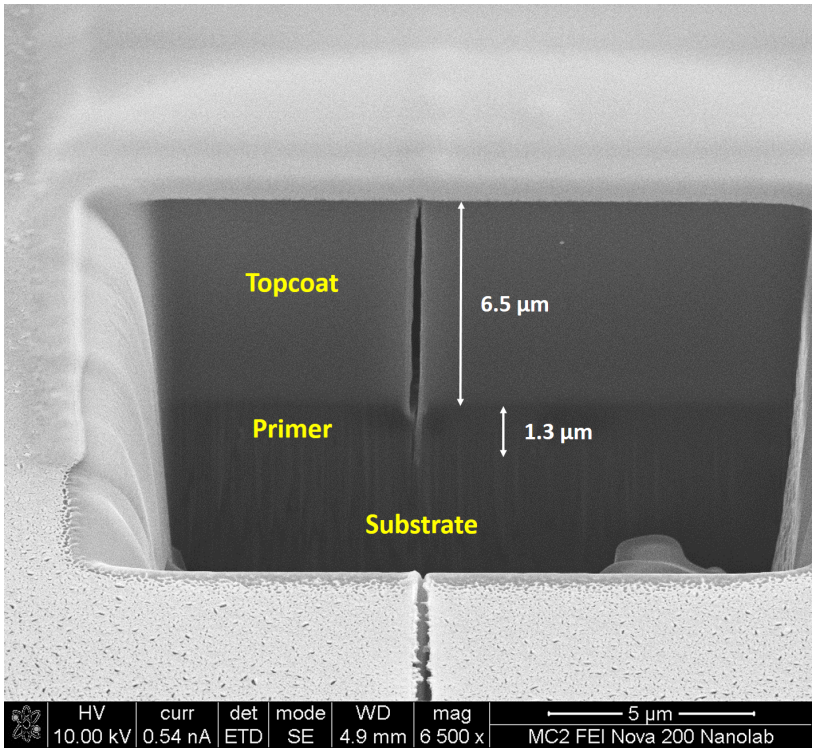

Figure 2.13: A scanning-electron micrograph of a cross-section through the topcoat and primer where a crack had channeled across the sample at a temperature 89 ± 3 °C. It will be noted that there is evidence of flow in the primer, and the crack tip has penetrated into the primer. This figure should be contrasted with Fig. 2.5, corresponding to cracking at room temperature.

Although any effects of temperature are probably dominated by softening of the primer, which precludes being able to deduce a thermal activation energy for kinetic crack growth, it is of interest to see whether the form of Eqn. 2.4 is in general agreement with the experimental data. A curve fit of this equation to the data obtained at 25 $\pm$ 2 °C is provided in Fig. 2.14, with $c_1 \exp(-Q/k_{\rm B}T) = 0.22 \pm 0.08$ µm/s, and $c_2 = 2.7 \pm 0.3 \times 10^{-21}$ m^2. It will be observed that this describes the data very well. If we further assume that the

two in-plane, characteristic lengths for rupture are identical and equal to d_o, we get a value of $d_o = 0.73 \pm 0.4$ Å for the topcoat, and a corresponding activation energy of $Q = 55 \pm 1$ kJ/mol (0.57 ± 0.01 eV / bond). While the characteristic length, in particular, seems to be a bit low, these values are certainly within a reasonable range of the values one might expect for rupture of a polymeric film.

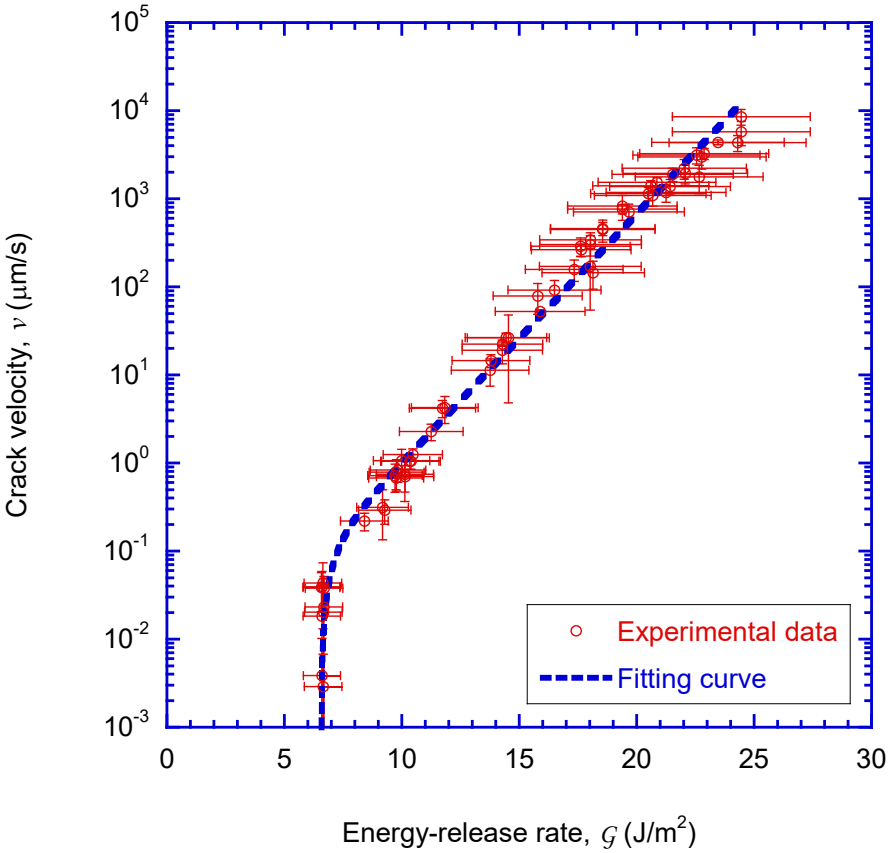

Figure 2.14: The data of Fig. 2.11 fitted to kinetic-rupture model of Eqn. 2.4, with $c_1 \exp(-Q/k_B T)$ and $c_2/k_B T$ having the values of 0.22 ± 0.08 μm/s and 0.65 ± 0.07 m^2/J respectively.

To investigate whether there is any fatigue crack growth in this system, the average crack velocity was measured for three cracks, each being tested at three different fatigue frequencies (1, 2 and 5 Hz) at 24 ± 1 °C. The average velocities at each frequency were then compared to the velocities that would be predicted by integrating Eqn. 2.4 (with the experimentally measured values) over each cycle. The results are provided in Table. 2.1, from which it will be seen that there was no obvious effect of frequency on crack velocity at room temperature. Plastic ratcheting in a primer layer or substrate [63, 64] has been invoked to explain effects of fatigue in brittle coatings [65, 66, 67]. However, it appears that

the primer is sufficiently brittle in this system, at room temperature, to avoid fatigue effects. We did not explore the possibility of fatigue at higher temperatures, where the primer may be above its glass-transition temperature.

Table 2.1: Comparisons between measured crack velocities under cyclic loading and the velocities predicted by integration of Eqn. 2.4 over a cycle. The observations and predictions are essentially identical. Furthermore, there was no significant effect of loading frequency on crack velocity. These results indicate that fatigue was not a significant factor for room-temperature crack propagation in this system.

Crack 1		
Frequency (Hz)	**Measured crack velocity (μm/s)**	**Predicted average crack velocity in each cycle (μm/s)**
1	0.12 ± 0.02	0.14 ± 0.05
2	0.11 ± 0.05	0.14 ± 0.05
5	0.09 ± 0.03	0.13 ± 0.04

Crack 2		
Frequency (Hz)	**Measured crack velocity (μm/s)**	**Predicted average crack velocity in each cycle (μm/s)**
1	0.15 ± 0.05	0.16 ± 0.06
2	0.13 ± 0.04	0.16 ± 0.06
5	0.10 ± 0.03	0.14 ± 0.05

Crack 3		
Frequency (Hz)	**Measured crack velocity (μm/s)**	**Predicted average crack velocity in each cycle (μm/s)**
1	0.19 ± 0.03	0.18 ± 0.07
2	0.16 ± 0.03	0.18 ± 0.07
5	0.14 ± 0.02	0.16 ± 0.06

2.5 Summary

In this chapter we have demonstrated a technique to analyze the velocity of channeling cracks in coatings and thin films, as a function of energy-release rate. This technique relies on a recognition of how the energy-release rate of a channeling crack is very sensitive to the depth to which it penetrates, its interactions with neighboring cracks, and the geometry and material properties of the system. The approach requires verification of the crack depth to determine through how many layers the crack penetrates. This can be done by focused ion-beam (FIB) milling followed by electron microscopy. The energy-release rate has to be calculated for individual cracks, using finite-element calculations and the measured distances from their nearest neighbors. The levels of residual strain in the cracked layer also need to be determined. This can be done by measuring the crack-opening displacements of cracks at known distances from their neighbors, and comparing them to numerical calculations.

These techniques have been used to explore the time-dependent crack propagation in a polymeric nano-composite system used as a hard coating on polycarbonates for automotive glazing applications. It was demonstrated that the particular system exhibited neither fatigue-crack growth, nor stress-corrosion cracking. Furthermore, the form of the velocity / energy-release rate curve was not consistent with models of visco-elastic crack growth. However, the behavior did fit a thermally-activated fracture process, with a very low threshold toughness of about 7 J/m^2, with an estimated activation energy of about 0.6 eV/bond.

CHAPTER 3

Application of cohesive-zone analysis to kinetic crack growth in brittle solids

3.1 Introduction

The Griffith theory of brittle fracture predicts that if the energy-release rate, $\mathcal{G}$, of a crack is greater than the toughness, Γ, then it is thermodynamically possible for the crack to propagate. This is a criterion rooted in the first law of thermodynamics, which deals with an equilibrium state but not the details of the crack propagation process. For example, for a mode-I crack opened by an uniaxial tensile stress, the energy-release rate increases monotonically with crack length. As a result, in the classical Griffith description, the crack starts to grow at $\mathcal{G} = \Gamma$ and then propagate indefinitely, leading to a catastrophic fracture.

It has been demonstrated in Chapter 2 and other experiments [28, 29, 56, 57, 68] that kinetic crack growth is noteable in many brittle solids. A kinetic crack propagates at finite velocity which is very sensitive to the energy-release rate, and sufficiently low such that dynamic effects are negligible. This is beyond the classical Griffith description, which is limited by the binary criterion at exactly the equilibrium state. The generalization of Griffith theory by Rice [31] eliminates this restriction by considering the second law of thermodynamics in irreversible fracture processes, which laid a solid theoretical foundation for the analysis of these kinetic crack growth problems. A satisfying approach to the crack velocity and energy-release rate correlation was finally built up by focusing on the discreteness of matter at the atomic or molecular levels [32, 33]. In this model, the crack tip is considered to be trapped by discrete energy barriers owing to atomic bonds or inter-molecule forces, and there exists a quasi-static regime such that the crack tip moves forwards (growth) or backwards (closure) by thermally-activated jumps over these energy barriers. The energy barriers for forward motion U^+ and backward motion U^- are biased

by the energy-release rate as

$$U^{\pm}(\mathcal{G}) = Q \pm \frac{1}{2N}\left(\Gamma_{\text{th}} - \mathcal{G}\right) \ , \tag{3.1}$$

where $Q = (U^+ + U^-)/2$, N is the density of these barriers and Γ_{th} is a threshold value of energy-release rate such that $U^- = U^+$. If the energy-release rate of a crack falls in the region bounded by two limits, Γ^- and Γ^+, given by $U^-(\mathcal{G}) = 0$ and $U^+(\mathcal{G}) = 0$, respectively, such that

$$\Gamma^{\pm} = \Gamma_{\text{th}} \pm 2NQ \ , \tag{3.2}$$

then the crack is referred to as "lattice-trapped" and propagates or heals with a kinetic speed depending on $\mathcal{G}$.

There a two noticeable facts in this formulation. Firstly, $U^- = U^+$ when $\mathcal{G} = \Gamma_{\text{th}}$, corresponding to the condition that the crack propagation and healing are the same favorable and lead to an zero overall crack velocity. Second, if we further assume $U^+ = U^- = Q = 0$, then $\Gamma_{\text{th}} = \Gamma^- = \Gamma^+$ and such a lattice-trapping effect is inexistent. In this case, the crack propagates or closes indefinitely if the energy-release rate was greater or less than the fracture toughness, this is in consensus with the Griffith criterion.

Explicit expression of crack velocity can be formulated by interacting the physical length scale associated with discrete possible positions for the crack-tip, d_o, an attempt frequency, ν_o, for crack advance, and the statistics of whether these attempts will be successful [34, 35]. The Boltzmann statistic gives that for each attempt, the difference between probabilities of bond breaking and healing is given by

$$\Delta p = \exp\left(-\frac{U^+(\mathcal{G})}{k_{\text{B}}T}\right) - \exp\left(-\frac{U^-(\mathcal{G})}{k_{\text{B}}T}\right) \ . \tag{3.3}$$

where k_{B} is Boltzmann's constant and T is the absolute temperature. Substituting Eqn. 3.1 into this, we have

$$\Delta p = 2\exp\left(-\frac{Q}{k_{\text{B}}T}\right)\sinh\left(\frac{\mathcal{G} - \Gamma_{\text{th}}}{2Nk_{\text{B}}T}\right). \tag{3.4}$$

and hence the explicit expression of kinetic crack velocity is in the form

$$v(\mathcal{G}) = 2\nu_o d_o \exp\left(-\frac{Q}{k_{\mathrm{B}}T}\right) \sinh\left(\frac{\mathcal{G}-\Gamma_{\mathrm{th}}}{2Nk_{\mathrm{B}}T}\right)^{*} \quad . \tag{3.5}$$

It is notable that in this mechanism, there is a probability of failure arising from statistical mechanics. Therefore, from the perspective of cohesive-zone modeling, the key phenomenon we analyze in this chapter is how to include the stochastic nature of fracture into the model, which permits a utility of this model in the simulation of time-dependent fractures. Generally, cohesive-zone models assume a binary fracture criterion in which the element fails if the work done against tractions reaches a critical value. This failure criterion can also be posed in terms of a critical displacement or traction. Here, we investigate the ability of cohesive-zone models to model fracture phenomena that have a probabilistic aspect to them, such as kinetic crack growth.

*This equation is in the same form as Eqn. 2.4 by letting $c_1 = 2\nu_o d_o$ and $c_2 = 0.5N$.

3.2 Cohesive-zone model

In a mode-I cohesive-zone model of interfacial fracture, the behavior of the material in the interfacial region can be be characterized by a traction-separation law of the form $\sigma = f(\delta)$, where σ is the traction across the interface, and δ is the normal displacement. The traction vanishes at a critical displacement, δ_c, resulting in decohesion. The cohesive work absorbed per unit area is calculated as

$$\mathcal{W} = \int_0^{\delta} f(\delta) d\delta \quad . \tag{3.6}$$

If the upper limit of integration is the critical displacement, the resultant work is proved to be equivalent to the toughness of the interface [4].

A quantity, termed the cohesive length, can be defined at the crack tip as [69, 70]:

$$\xi_o = \frac{\bar{E}\delta_o^2}{\mathcal{W}_o} \tag{3.7}$$

where $\bar{E}$ is the effective modulus for a bi-material system [70]. In plane stress, $\bar{E}$ is equal to the Young's modulus, E, and in plane strain, $\bar{E}$ is equal to $E/(1-\nu^2)$, where ν is Poisson's ratio. The subscript "o" denotes a value at the tip of the cohesive crack, so that δ_o is the relative displacement across the interface at the cohesive crack-tip, and $\mathcal{W}_o$ is the work done against the crack-tip tractions. It will be noted that this quantity has units of length. When normalized by an appropriate geometrical length scale inherent to the problem, ξ_o indicates whether the crack-tip stress field is controlled by singular stresses (when the normalized value is small) or not [69, 70, 71]. When the normalized cohesive length is very small, typically much less than 0.4, then the stresses are singular, and, if the surrounding material is linear elastic, the limitations of LEFM are met. When the normalized cohesive length is larger, typically much greater than 0.4, then the stresses tend to be uniform ahead of the crack. An equivalent way of expressing these statements is to say that in the former case the transition flaw size is small, and the system tends to be flaw-sensitive, and in the latter case the transition flaw size is large, and the system tends to be flaw-tolerant.

A more general formulation of the traction-separation law, which allows fracture before the tractions have reduced to zero, can be expressed as

$$\sigma = \iota f(\delta) \quad , \tag{3.8}$$

where ι usually takes the value of $\iota = 1$, but where it can be assigned a value of $\iota = 0$, representing decohesion. This formulation can be used in mixed-mode problems where it is assumed that shear deformations do not directly affect the level of the normal tractions, but that a mixed-mode failure criterion may induce fracture before the crack-tip work reaches the toughness [72]. This approach is relevant to the kinetic crack growth problem considered in this chapter through the ability to give ι a value of 1 or 0 stochastically, since the molecular level bond-breaking process follows Boltzmann statistics with a probability that depends on the magnitude of the work done against the molecular bonding across the interface [34, 35].

3.3 Numerical approach

In this section, we will explore whether a cohesive-zone model with an appropriate probabilistic algorithm can be used to model kinetic-fracture. The problem will be set up with an inherent length scale associated with the finite-element mesh and element size of the cohesive-zone to mimic the concept of atomic spacing. However, it will be demonstrated that the results become mesh insensitive provided the mesh size is much smaller than the cohesive length. Initially this will be done under LEFM conditions (with the normalized cohesive length being sufficiently small) to verify that that it yields the expected results of Lawn [34, 35]. Then this will be expanded to large cohesive lengths to explore the physics of the regime where Lawn's model is not valid.

The calculations were performed using the finite-element program ABAQUS/Standard in a plane-stress implicit static mode. The properties of the cohesive elements were defined through a user-defined subroutine in the FORTRAN programming language [72]. Figure 3.1 shows the linear traction-separation law with a stiffness of k_s, adopted in this study. This law was chosen for its simplicity, and the fact that its cohesive length, given by $\xi_o = 2\bar{E}/k_s$, is independent of load [70], and constant along the interface. If the critical traction at which the element is possible to fail is $\hat{\sigma}$, the corresponding threshold toughness is $\Gamma_{\text{th}} = \hat{\sigma}^2/2k_s$. The ability of such a traction-separation law has been attested to describe accurately all aspects of LEFM when ξ_o is sufficiently low, provided the mesh size, l, is sufficiently small compared to ξ_o have been met, is described elsewhere [69]. Following Eqn. 3.8, this law can be expressed as

$$\sigma = \iota k_s \delta \quad , \tag{3.9}$$

with the work done against the tractions being given as

$$\mathcal{W} = \frac{\sigma\delta}{2} = \frac{k_s\delta^2}{2} \quad , \tag{3.10}$$

while $\iota = 1$. In the absence of statistical effects, $\iota = 1$ while $\mathcal{W}$ is less than a critical value of Γ, defined as the interfacial toughness, and $\iota = 0$ for larger values of $\mathcal{W}$. Failure under such conditions always occurs at the crack tip where the value of $\mathcal{W} = \mathcal{W}_o$ is a maximum, and the crack advances steadily across the geometry.

In the present study, we introduce a statistical aspect to determining the value of ι. We still assume that $\iota = 1$ if $\mathcal{W} < \Gamma$, but if $\mathcal{W} \geq \Gamma$ the probability that $\iota = 0$ and a cohesive

element fails is given by statistics of kinetic bond breaking from Lawn's model [34]. We ignore the possibility of bond healing, so in a single computational time step, Δt, the probability that $\iota = 0$ is given by

$$p_f = \alpha \sinh\left(\frac{\mathcal{W} - \Gamma_{\text{th}}}{\beta^*}\right) = \alpha \sinh\left[\frac{\Gamma_{\text{th}}}{\beta^*}\left(\frac{\mathcal{W}}{\Gamma_{\text{th}}} - 1\right)\right] \quad , \tag{3.11}$$

where α and β^*/Γ are non-dimensional material parameters that can be correlated to Lawn's model [34, 35]. In particular, one can equate (i) the attempt period, $1/\nu_o$, to the computational time step, Δt, (ii) the increments of crack advance, d_o, to the mesh size, l, (iii) the activation-energy term $2\exp(-Q/k_{\text{B}}T)$ to α, and (iv) the normalizing group $2Nk_{\text{B}}T$ to β^*.

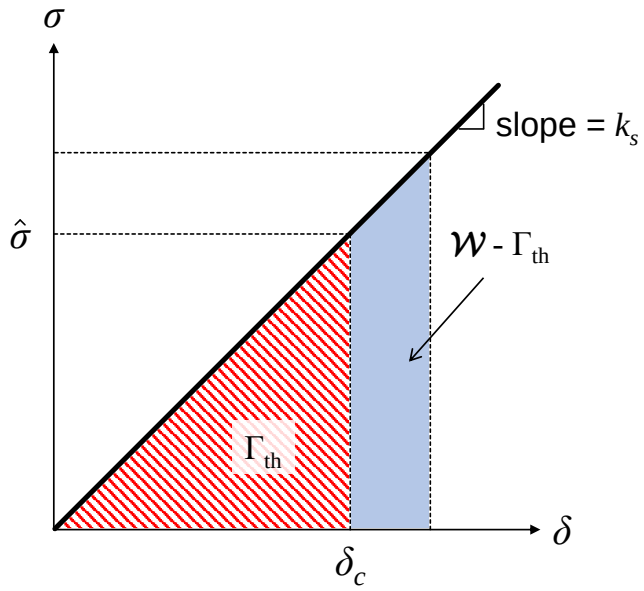

Figure 3.1: Linear traction-separation law with a stiffness of k_s is adopted for the modeling of kinetic crack growth. The cohesive length is always equal to $\xi_o = 2\bar{E}^*/k_s$. The critical traction and displacement at which the element is possible to fail are $\hat{\sigma}$ and δ_c, respectively, corresponding to a threshold toughness of $\Gamma_{\text{th}} = \hat{\sigma}^2/2k_s$.

The specific geometry used for the calculations is shown in Fig. 3.2. It consists of a center-cracked sheet with a height of $2H_o$, a width of $2L_o$, and an initial crack of length $2a_i$ in the middle of an interface that runs along the horizontal central plane and is bonded by linear cohesive elements. The size of the cohesive elements, l, was less than $0.01\xi_o$ to ensure accurate values of stresses ahead of the crack [69]. The lengths, H_o and L_o, were

greater than $50a_i$, and any crack growth was limited to be less than $0.02a_i$, to ensure that the crack length was the controlling geometrical length and that the geometry remained essentially invariant during the calculations. The surrounding material was homogeneous and linear elastic, with a modulus of $\bar{E} = E$ under plane-stress. For computational efficiency, only half the problem was modeled, with symmetrical boundary conditions being applied along the vertical plane of symmetry (Fig. 3.2(a)).

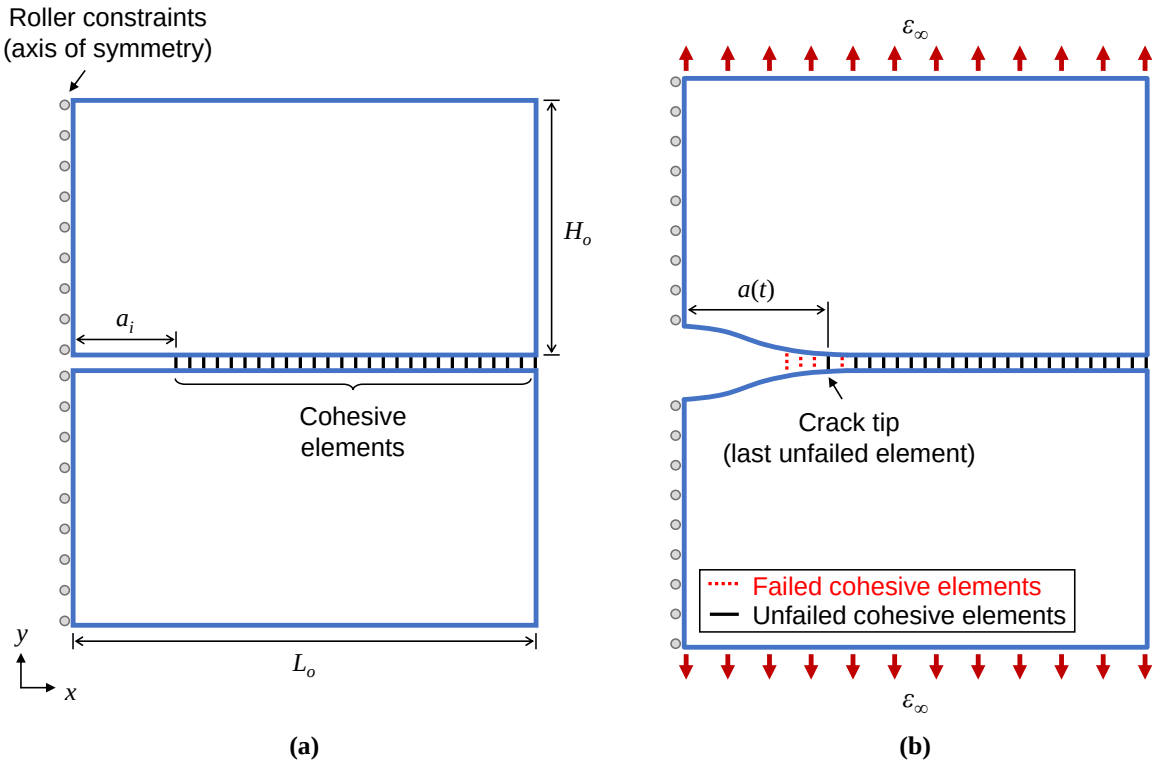

Figure 3.2: **(a)** Homogeneous geometry with a central crack of initial length $2a_i$ is used for the cohesive-zone modeling of kinetic crack growth, where $L_o, H_o \geq 50a_i$. Only half of the geometry is presented due to symmetry. **(b)** At time $t = 0$, a constant strain ε_∞ is remotely applied to the specimen, leading to a mode-I crack propagation in the x-direction along the interface of cohesive elements. The crack-tip is defined as being the location of the last unfailed element in this study.

A fixed displacement corresponding to a given strain of ε_∞, was applied to the remote boundaries of the specimen at time $t = 0$, and held constant as the crack propagated under mode-I conditions (Fig. 3.2(b)). For the specific calculations conducted in this study, a range of crack sizes and cohesive properties were studied such that $0.004 \leq \xi_o/a_i \leq 10^4$.

Therefore, at the lowest end of this range, the problem was well within the regime where linear-elastic fracture mechanics is valid [71, 70], in accordance with the assumptions of Lawn's kinetic crack growth model. At the highest end of this regime. the problem was well within a regime where the failure criterion is a strength-based criterion, not an energy-based criterion [71, 70].

The calculations proceeded by generating a random variable, r_f, uniformly distributed between 0 and 1, for every cohesive element along the interface during each computational step. The total work done against cohesive tractions was calculated for each element during each computational step. This allowed p_f to be computed from Eqn. 3.11. The random variable r_f for each cohesive element was then compared to the value of p_f for the corresponding element. If $r_f \leq p_f$, then ι was set to 0, and the element failed. If $r_f > p_f$, then ι was set to 1, and the element survived for the next computational increment. It will be noted that, elements ahead of the cohesive crack tip could fail before the element at the crack tip, allowing for a diffuse crack-tip region (Fig. 3.2(b)). The crack velocity was computed in terms of the average time for last element at the crack-tip to fail, t_f, and the element size, l, as $v = l/t_f$.

3.4 Results and discussion

3.4.1 Crack growth and determination of crack velocity

Figure 3.3 shows how the crack extends as a function of time, $\Delta a(t) = a(t) - a_i$, for a calculation done for $\Gamma_{\text{th}}/\beta^* = 3.3$, with a very small mesh size, $\xi_o/l = 2000$, and well within LEFM conditions, $\xi_o/a_i = 0.008$. The computational time step increment is equated to $1/\nu_o$, therefore the non-dimensional quantity $t\nu_o$ is equal to the number of computation steps numerically. It is observed that the crack length grows approximately linearly with time, despite small oscillations associated with the stochastic nature of the algorithm. The crack velocity, $v = \mathrm{d}a/\mathrm{d}t$, can be computed from the slope of this curve.

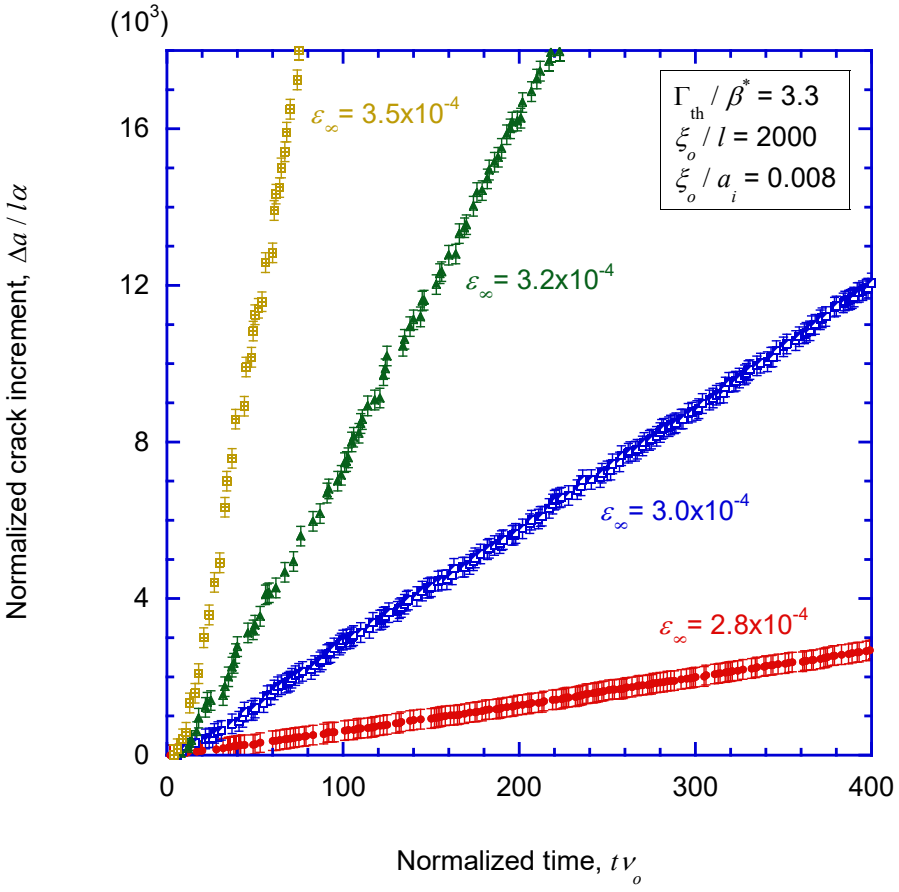

Figure 3.3: Non-dimensional increment in crack length is plotted as a function of time, for $\xi_o/a_i = 0.008$, $\Gamma_{\text{th}}/\beta^* = 3.3$ and $\xi_o/l = 2000$. The crack velocity is almost constant despite small oscillations due to the stochasticity in the algorithm, which can be determined by measuring the slope of each curve.

3.4.2 Crack growth the LEFM regime

The crack velocity is of the non-dimensional form:

$$\frac{v}{l\alpha\nu_o} = F_v\left(\frac{\pi\varepsilon_\infty^2\bar{E}a_i}{\Gamma_{\text{th}}}, \frac{\Gamma_{\text{th}}}{\beta^*}, \frac{\xi_o}{l}, \frac{\xi_o}{a_i}\right) \quad , \tag{3.12}$$

where the first term on the right-hand side is the ratio of the nominal energy-release rate that controls fracture in the LEFM limit to the toughness. The function was computed from the numerical data illustrated in Fig. 3.3 and is plotted in Fig. 3.4 with respect to $\pi\varepsilon_\infty^2\bar{E}a_i/\Gamma_{\text{th}}$ for three different values of ξ_o/a_i, for $\Gamma_{\text{th}}/\beta^* = 3.3$ and the mesh size was kept at $\xi_o/l = 2000$. In this plot, all thee cohesive-length scales were kept in the LEFM range, to be consistent with the assumptions of Lawn's model [34], so they do not affect the crack growth, since ξ_o/a_i has no effect on fracture under LEFM conditions. As expected, the form of the plots is identical to that predicted by Lawn's model [34], exhibiting a crack-velocity threshold at $\pi\varepsilon_\infty^2\bar{E}a_i/\Gamma_{\text{th}} = 1$.

Although the non-dimensional quantity $v/l\alpha\nu_o$, which is the average frequency of crack-tip jumps between cohesive elements, is independent of the size of the cohesive-zone within the LEFM regime, as was shown in Fig. 3.4, it does depend on the mesh density, ξ_o/l, at the crack tip (Fig. 3.5). However, an analysis of these data reveals that an alternative normalization of the crack velocity, using the crack-tip cohesive length, ξ_o, rather than the mesh size gives a mesh-independent result (Fig. 3.6). Within the LEFM regime, the crack velocity can be written as

$$\frac{v}{\xi_o\alpha\nu_o} = F_v\left(\frac{\pi\varepsilon_\infty^2\bar{E}a_i}{\Gamma_{\text{th}}}, \frac{\Gamma_{\text{th}}}{\beta^*}\right) \quad . \tag{3.13}$$

For $\Gamma_{\text{th}}/\beta^* = 3.3$, there is no dependence on the mesh size if the mesh is smaller than about 1% of the cohesive length. This criterion is comparable to, and smaller than, the 2% criterion of Sills and Thouless [70] for the mesh size required to ensure that the stresses within a cohesive-zone are described accurately by a cohesive-zone model. A more restrictive criterion is required for higher values of $\Gamma_{\text{th}}/\beta^*$, which is a parameter scaling the effect of cohesive work in the exponential term in Eqn. 3.11.

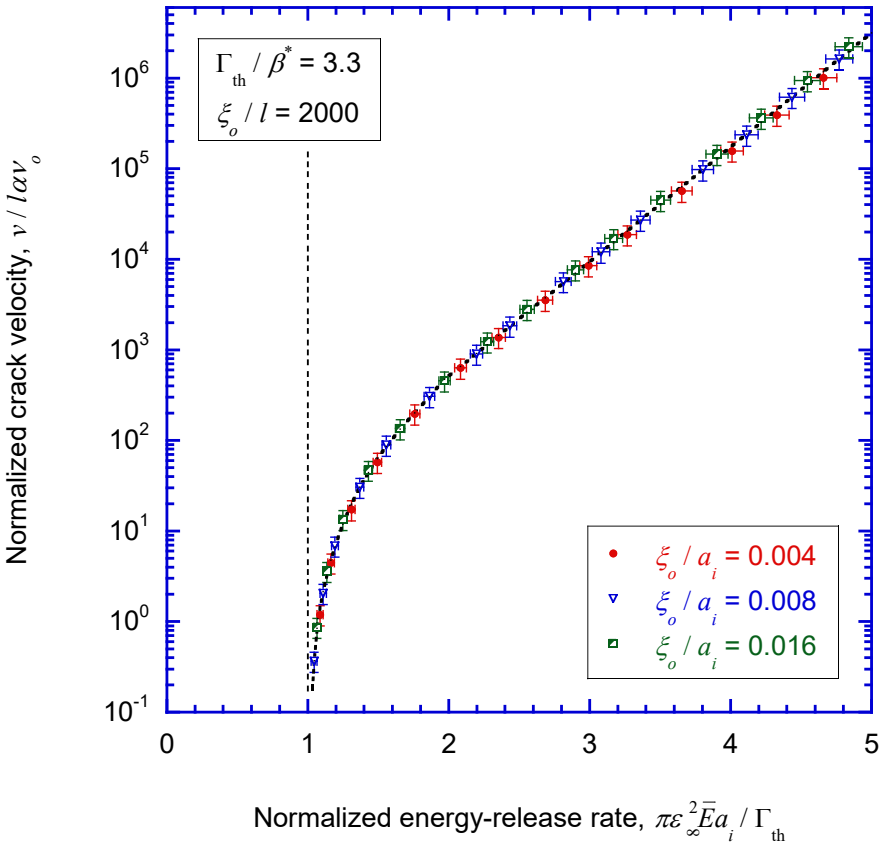

Figure 3.4: Normalized crack velocity is plotted as a function of nominal energy-release rate. Within a regime that is clearly under LEFM conditions (low values of ξ_o/a_i), and mesh size kept at $\xi_o/l = 2000$, there is no effect of ξ_o, and the problem is described by LEFM, with the crack velocity being a unique function of the applied energy-release rate, and a crack-growth threshold at $\pi\varepsilon_\infty^2 \bar{E} a_i/\Gamma = 1$, as expected.

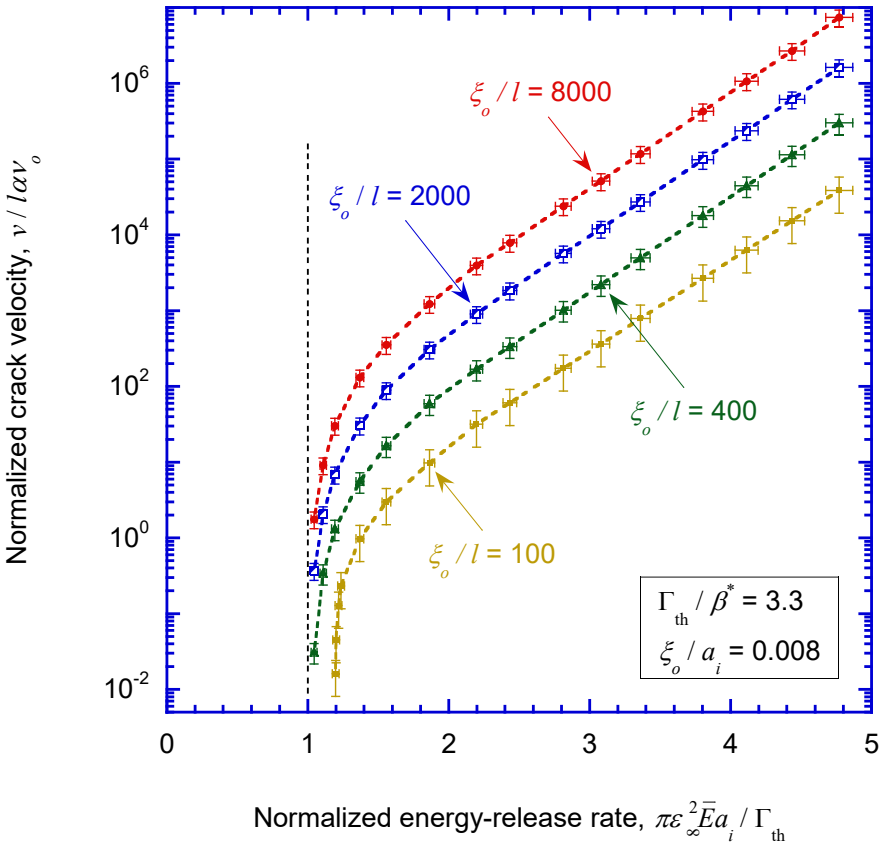

Figure 3.5: Normalized crack velocity is plotted as a function of energy-release rate within the LEFM regime. As expected from the way the model was initially formulated, the normalized crack velocity, which is the average frequency of crack-tip jumps between cohesive elements, depends upon the mesh size, and scales with mesh density in the cohesive-zone.

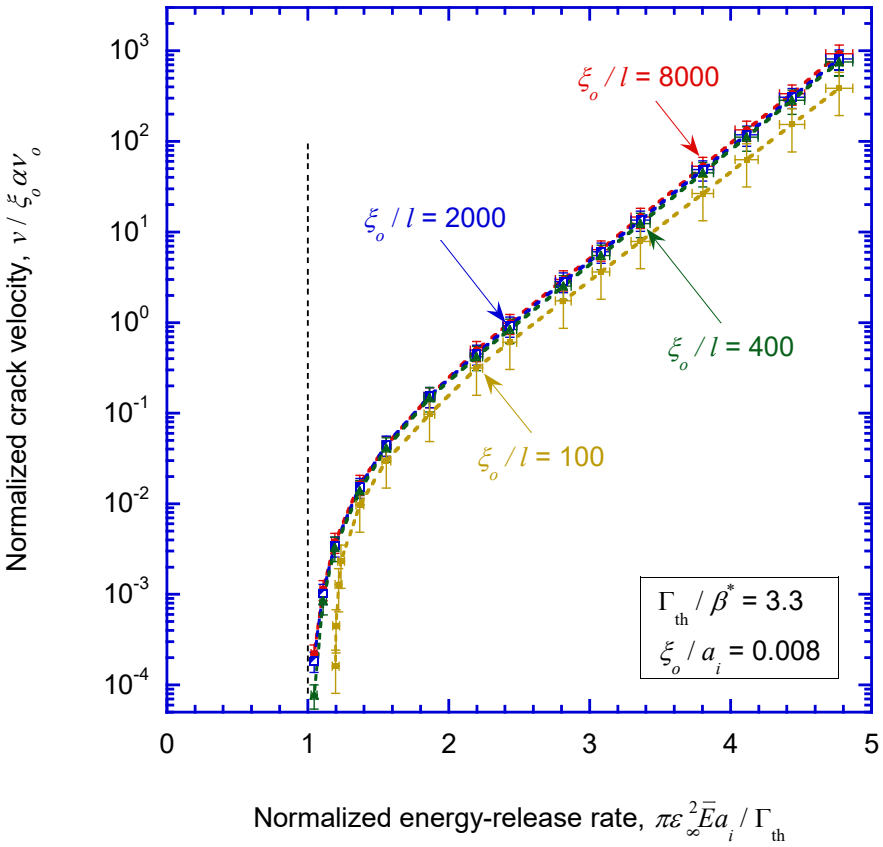

Figure 3.6: Provided the mesh is small enough, the crack velocity is independent of the mesh size. The characteristic length for the crack velocity becomes the cohesive length, not the mesh size, even though the problem was originally formulated in terms of the mesh. Mesh sensitivity only becomes an issue if the mesh is larger than about 1% of the cohesive length.

Figure 3.7 displays representative plots of normalized cohesive work, $\mathcal{W}/\Gamma_{\text{th}} - 1$, and normalized failure probability, p_f/α, with respect to the normalized distance $\tilde{x} = x_o/\xi_o$, where x_o is the horizontal distance measured from the crack tip (Fig. 3.7(a)). Although these functions are too complicated to be analytically expressed, the plots still reflect characteristics of Eqn. 3.13. Firstly, under the same remote strain, if the meshing is sufficiently fine, the cohesive work is a function only depends on the normalized distance $\tilde{x}$. This is consistent with the form of Eqn. 3.13, showing that it is meaningful to normalize the crack velocity by the cohesive length instead of the mesh size. It is manifested in Fig. 3.7(b) and (c) that the cohesive elements tend to fail within a very narrow region at the crack tip, even though the algorithm allows failure to appear at any point along the cohesive interface if the cohesive work exceeds the threshold. The failure region decreases in size as the value of $\Gamma_{\text{th}}/\beta^*$ is increased. We were also able to estimate the size of this region by defining a cut-off position, $\tilde{x}_c$, corresponds to 10% of the failure probability at the crack tip, $P_{f_o}/\alpha = \sinh\left[(\pi\varepsilon_\infty^2 \bar{E} a_i - \Gamma_{\text{th}})/\beta*\right]$. The value of $\tilde{x}_c$ is plotted as a function of $\Gamma_{\text{th}}/\beta^*$ in Fig. 3.8.

The crack velocity exhibits expected behavior in Fig. 3.9, for three different values of $\Gamma_{\text{th}}/\beta^*$. By restricting the failure within a narrower region at the crack tip, we observed that the slope of the log-linear plot has a tendency of approaching the value of $\Gamma_{\text{th}}/\beta^*$, as expected by Lawn's model [34]. Fitting curves in Fig. 3.10 demonstrate that Eqn. 3.13 could be explicitly estimated, in the form of Lawn's model, as

$$\frac{v}{\tilde{x}_c \xi_o \alpha \nu_o} = \sinh\left(\frac{\mathcal{G} - \Gamma_{\text{th}}}{\beta^*}\right) \quad . \tag{3.14}$$

where $\mathcal{G} = \pi\varepsilon_\infty^2 \bar{E} a_i$ since the LEFM conditions are satisfied, and $\tilde{x}_c$ is determined in Fig. 3.8 such that $\tilde{x}_c \approx 0.0104, 0.0029$ and 0.001 for $\Gamma_{\text{th}}/\beta^* = 3.3, 10$ and 33.3, respectively. These results indicate that the cohesive length, ξ_o, multiplied by a coefficient $\tilde{x}$ depending on the value of β^*, forms a characteristic length for the kinetic crack growth. Referring to Eqn. 3.1, β^* is a parameter associated with the bond density in the cohesive-zone, which affects the activation-energy, U^+ (and U^-), of bond rupture (and healing) process. A lower value of β^*, or equivalently higher value of $\Gamma_{\text{th}}/\beta^*$, corresponds to the condition that the cohesive-zone contains less bonds. This permits the fracture to occur sufficiently close to the cohesive crack tip, and the crack propagation is more precisely described by Lawn's kinetic model [34]. On the other hand, the crack velocity moves slightly away from Lawn's description with higher values of β^*, corresponding to the case that the cohesive-zone, although small enough comparing with geometrical lengths, contains

greater amount of bonds, which leads to a more diffused region of bond rupture.

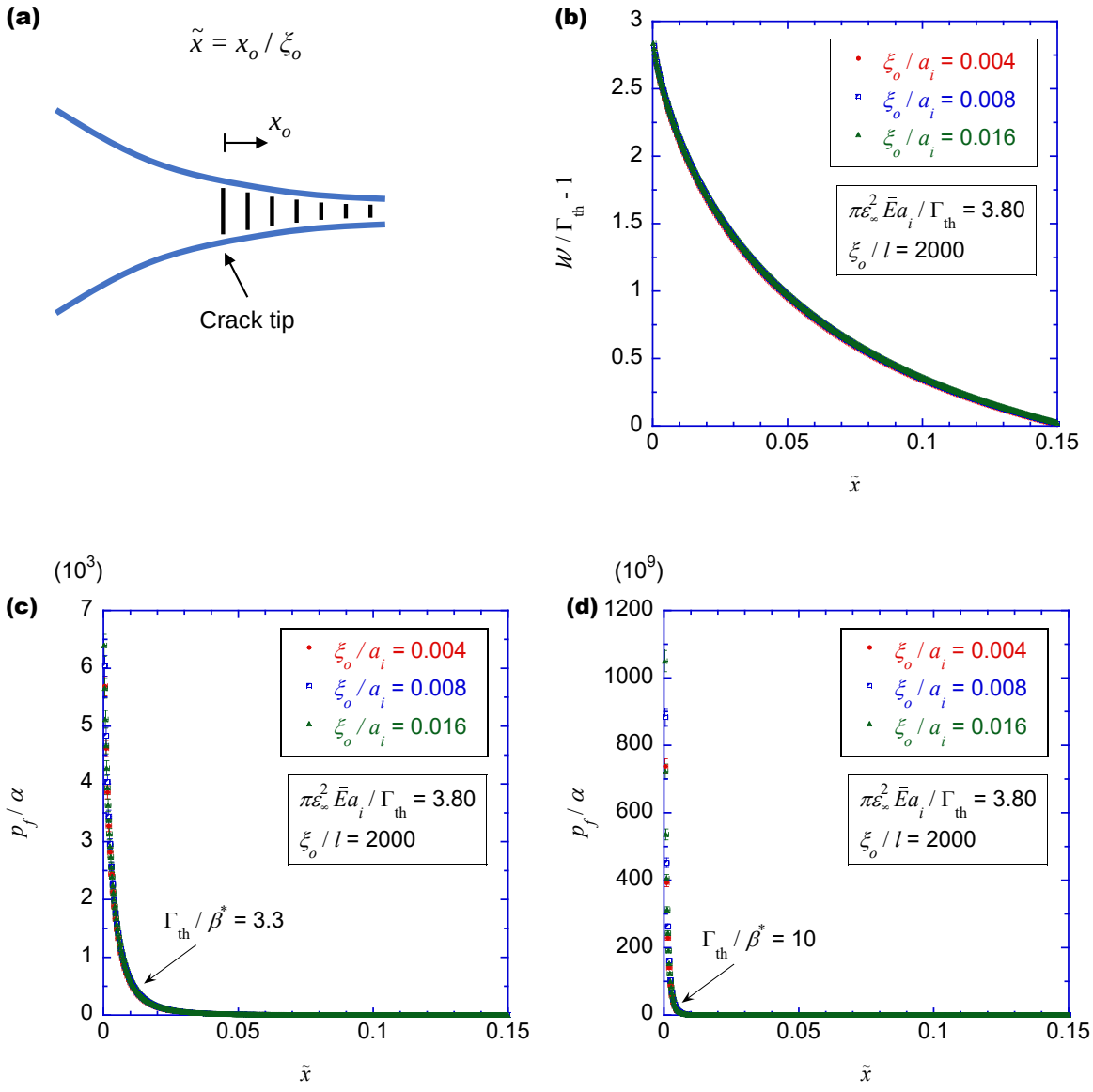

Figure 3.7: Representative plots of **(b)** the normalized cohesive work, $\mathcal{W}/\Gamma_{\text{th}} - 1$, and **(c)(d)** the failure probability, p_f/α, plotted as functions of a normalized distance, $\tilde{x} = x_o/\xi_o$, where x_o is the distance measured from the crack tip. If the cohesive lengths are kept within the LEFM regime with sufficiently fine meshing, both functions are only dependent on the normalized distance $\tilde{x}$. Plots **(b)** and **(c)** show that failure tends to occur within a very narrow region near the crack tip. This failure region decreases in size for higher $\Gamma_{\text{th}}/\beta^*$ values.

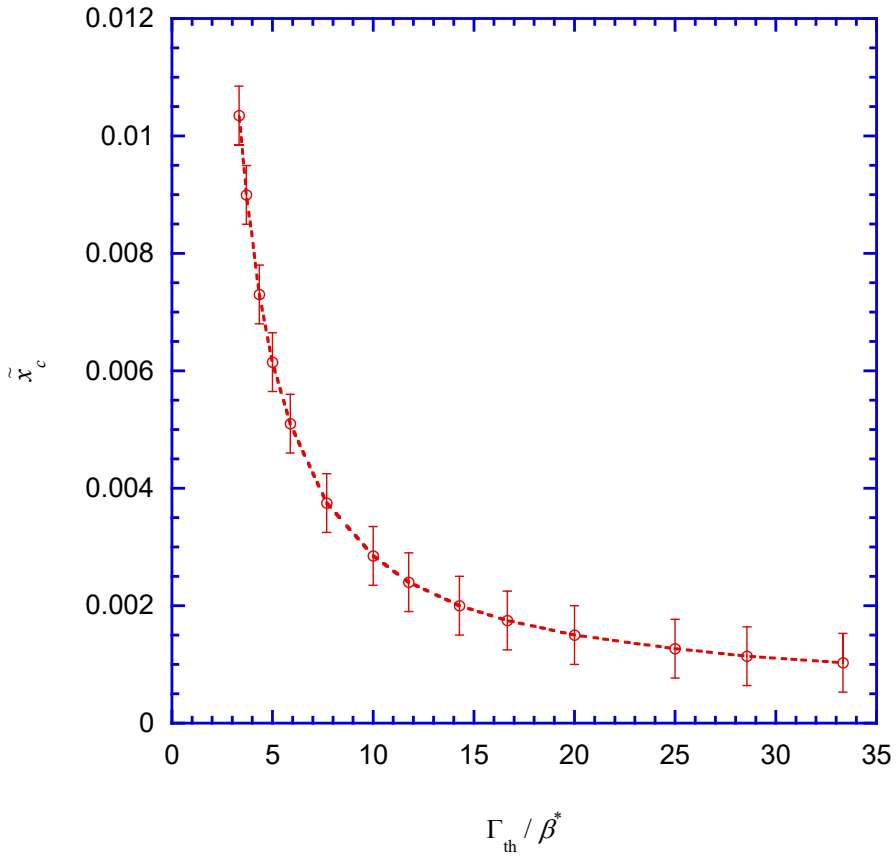

Figure 3.8: Size of the region in which the failure probability is greater than 10% of the probability at the crack tip: $P_{f_o}/\alpha = \sinh\left[(\pi\varepsilon_\infty^2 \bar{E} a_i - \Gamma_{\text{th}})/\beta*\right]$.

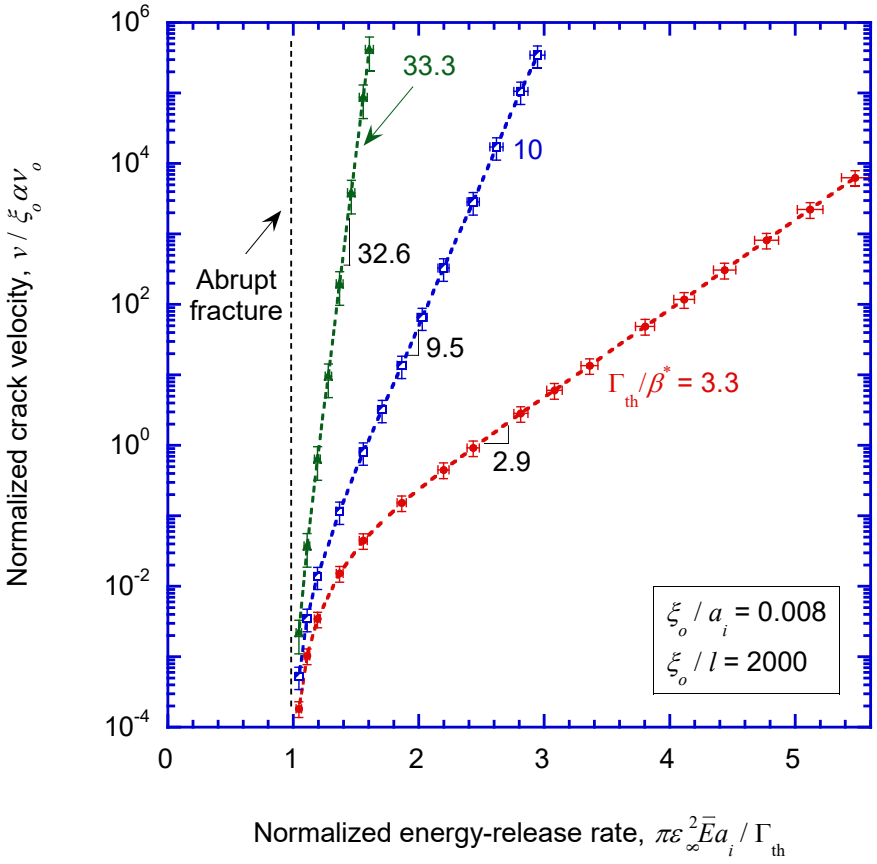

Figure 3.9: An increase in the value of Γ/β^* leads to an increase in the slope of the linear region away from the threshold on the log-linear plot. As $\beta^* \to 0$, abrupt fracture occurs at $\pi\varepsilon_\infty^2 \bar{E} a_i = \Gamma$ as described by the classical Griffith theory; as $\beta^* \to \infty$, crack velocity exhibits weak dependence on the loading.

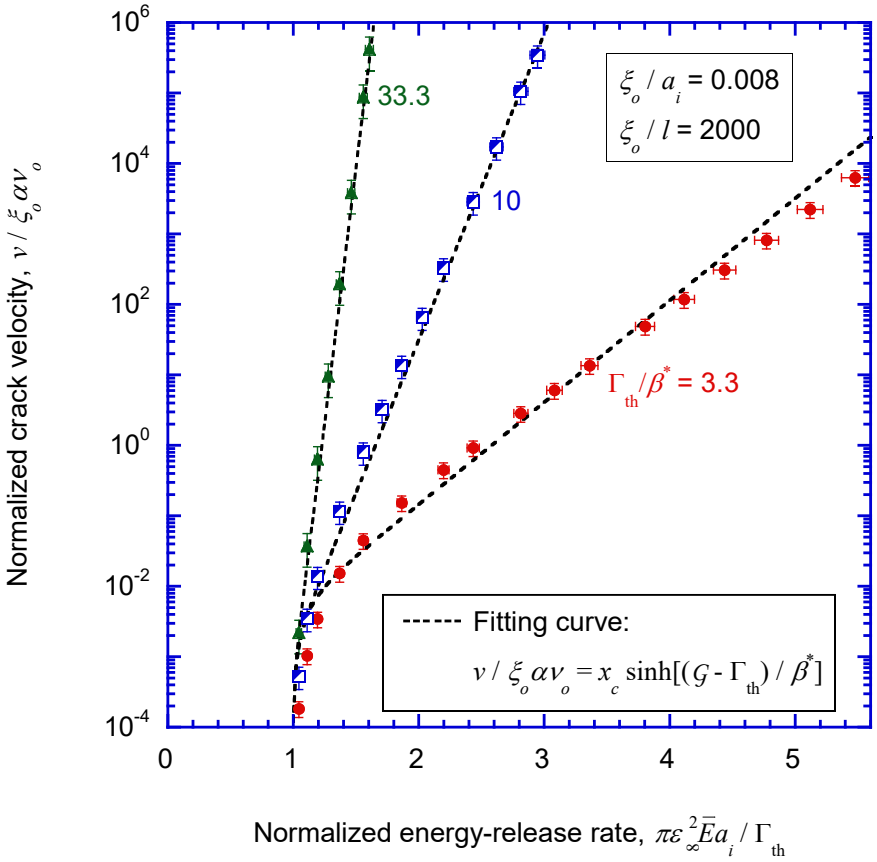

Figure 3.10: Comparison between the fitting curve estimated by Eqn. 3.14 and the results presented in Fig. 3.9.

3.4.3 Crack growth out of the LEFM regime

We have, in Section 3.4.2, shown that a model that was originally based on a mesh dimension as being the characteristic length for crack advance can be re-scaled into a problem that is mesh independent. It is noted that there are other examples of small-scale yielding, in which the crack-tip stress field is controlled by a stress-intensity factor, but fracture requires the introduction of a length parameter in addition to a toughness. Creep or viscoelastic crack growth exhibits such behavior, and it has been shown that a cohesive-zone model can be used to introduce such a length [26]. In the present case, the characteristic length takes on the product of the cohesive length, ξ_o, and a coefficient term, $\tilde{x}$, which physically associated with the bond density in the cohesive-zone. The cohesive length needs to be small compared to any geometrical length scale to ensure a singular crack, and the LEFM requirements; and also needs to be not too large compared with atomic spacings such that the bonds tend to break sufficiently close to the cohesive crack tip, in accord with assumptions of Lawn's model [34].

The discussion of the previous paragraph raises the obvious question of what happens when the activation energy is small, leading to a large cohesive length scale and a diffuse zone ahead of the crack with broken bonds. The results of calculations with a large variation of cohesive-length scales are shown in Fig. 3.11. The crack velocity is plotted as a function of the nominal energy-release rate – the parameter that controls the crack velocity when ξ_o/a_i is small, in Fig. 3.11(a). It will be observed that as the cohesive-length scale increases, the crack velocity increases at a given level of this parameter. In particular, crack growth can occur for values of the normalized energy-release rate smaller than one. This is consistent with previous cohesive-zone results that make it clear that an LEFM prediction provides an upper bound for the strength of a cracked body [71, 70]. These same results also suggest that as the cohesive-length scale increases, fracture transitions from being controlled by the toughness of an interface to the strength of an interface. Therefore, the results of Fig. 3.11(a) have been replotted in Fig. 3.11(b) in terms of the nominal strength of the interface in the limit of a huge cohesive-length scale – the limit where the interface moves apart in a uniform fashion, so the theoretical strength would be

$$\hat{\sigma} = \epsilon_\infty \bar{E}(1 + a_i/L) \tag{3.15}$$

where $\hat{\sigma}$ is the value of the cohesive tractions corresponding to when the work done against them is Γ_{th}. As discussed in Ref. [71], this strength limit is an upper bound to the strength of an interface in the limit of very large cohesive-length scales. One can see from the

plot of Fig. 3.11(b), that the equilibrium limit tends to this theoretical maximum for large cohesive-length scales tends, and is reduced as the cohesive-length scale gets smaller. Contour plots in Fig. 3.12 show the different fracture behaviors with small and large cohesive lengths.

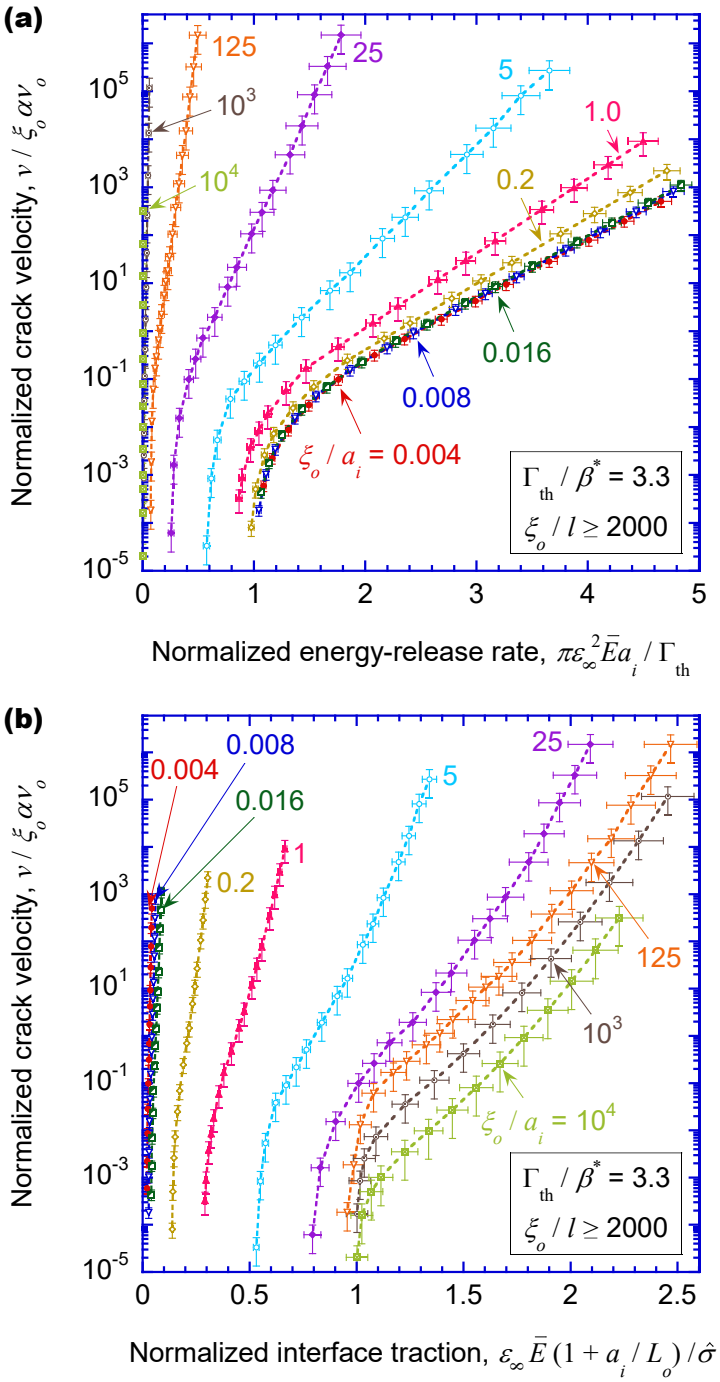

Figure 3.11: The effects of increasing the normalized cohesive length, ξ_o/a_i, on the crack velocity plotted against **(a)** energy-release rate and **(b)** strength criterion.

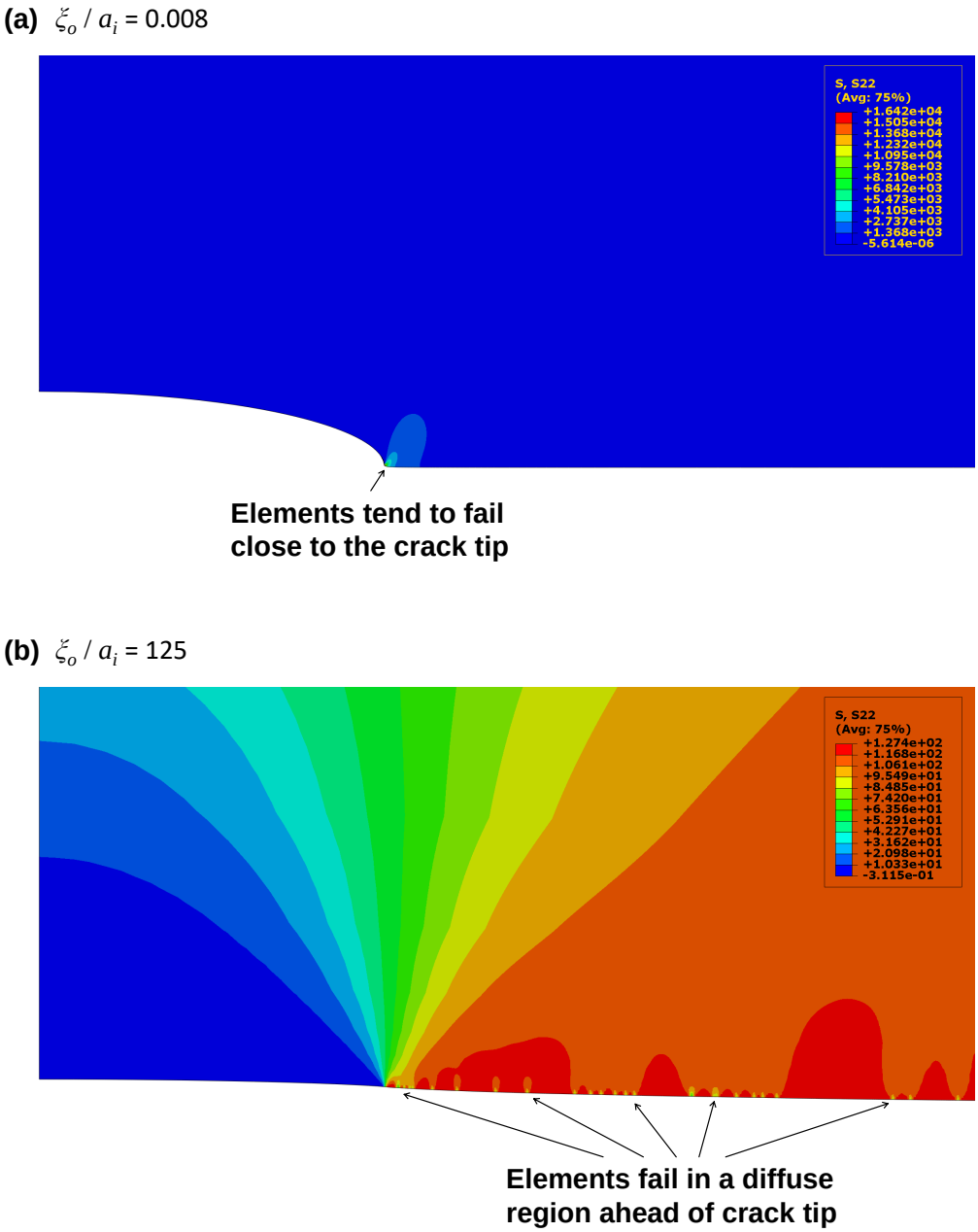

Figure 3.12: Contour plots show that fracture occurs **(a)** in a limited region at the crack tip for small cohesive-zone ($\xi_o/a_i = 0.008$), and **(b)** in a diffused region for large cohesive-zone ($\xi_o/a_i = 125$).

3.5 Summary

In this chapter, we have outlined a use of stochastic cohesive-zone model to simulate kinetic crack growth. Although this model was originally formulated in terms of the dimensions of the finite-element mesh representing the discrete nature of crack advance, we have shown that if the mesh is sufficiently small compared to the cohesive length, a mesh independent result can be obtained, in which the length parameter required to model fracture is provided by the cohesive length. Physically, from a kinetic-crack perspective, the characteristic length represented by the product of the cohesive length and a coefficient associated with the bond density and activation energy of bond rupture.

Within the LEFM regime, the cohesive-length needs to be sufficiently small, comparing with the geometrical length scales, such as the crack length. In this case, if the amount of bonds in the cohesive-zone is low, then the bond-rupture activation energy is high. As a result, fracture occurs only near the crack tip, and the problem is described very well by the kinetic model of Lawn [34]. Conversely, if the cohesive-zone has a dense population of bonds, the activation energy is accordingly low and there is a diffuse region of bond breaking ahead of the crack tip. The crack velocity is less accurately agree with Lawn's expression in this case, but the characteristics of crack behavior are still unchanged.

For large cohesive-length scales, the problem is no longer controlled by the singular stress field, and, crack advance is controlled by the strength rather than the nominal toughness. Here the use of a cohesive-zone model to analyze kinetic crack growth provides some additional insight for a regime beyond the assumptions of the original kinetic-crack-growth model [34, 35].

CHAPTER 4

Application of cohesive-zone analysis to brittle-ductile transitions in toughened polymers

4.1 Introduction

In Chapter 3, we have shown that incorporating stochastic effects into cohesive-zone method allows one to model kinetic crack growth. Although the problem was initially formulated in discrete terms invoking a finite mesh size, we showed that the results could be recast in a mesh-independent form, with the cohesive length providing the required length scale. The kinetic crack growth is regarded as an accumulation of time-dependent, thermally-activated crack tip jump at molecular levels, which follows the Boltzmann statistics. In this chapter, we will demonstrate the modeling of another type of crack growth involving stochastic crack tip jumps at macroscopic levels.

Crack growth in polymers can sometimes exhibit "stick-slip" behavior [73, 17, 74, 75]. In the use of this terminology, the crack behavior is described as intermittent occurrences of crack arrest (stick) and dynamic crack propagation (slip). The interpretations of this phenomenon are various. The instability could be ascribed to a decrease in toughness with fast crack speed [16, 20, 10]; or alternatively, the abrupt dynamic propagation of a stationary crack could be referred to a demand of additional driving force for the initiation of growth [73].

However, in rubber-toughened polymers, experimental observations of transitions between quasi-static, rubber-toughened crack growth and dynamic, brittle crack growth [38, 39, 40, 41, 42] show significantly differences from the classical form of "stick-slip" behavior of periodic crack arrest and propagation [40, 41]. At low loading rates or high volume percentage of rubber, fracture tends to progress in a stable fashion, with the toughening

mechanisms in operation. However, as the loading rate is increased or the volume of rubber is reduced, the crack can suddenly become unstable and jump forward, dissipating very little energy. Under displacement control, this untoughened crack is eventually arrested and can then start growing in a toughened mode again until it undergoes another transition to a brittle mode. The fracture surfaces exhibit characteristic signs of both toughened and untoughened fracture. However, most significantly for this present chapter, the transitions to the brittle mode appear to be completely random. While there is an increasing tendency for the brittle mode to occur at higher loading rates or reduced rubber contents, there is no obvious critical rate at which this transition occurs, and the toughness of the steady-state mode appears to be unaffected by the crack velocity. The cohesive parameters were extracted from the experimental observations for both modes of failure [41], however detailed modeling was still need to be developed to explain the transitions.

The study of toughening mechanism for rubber-toughened polymers has been given exclusive attention by the researchers. Cavitation of rubber particles is believed to be the most important characteristic associated with the toughening mechanism based on the SEM examination of fracture surfaces [43]. The increase in toughness is attributed to the relaxation of constraints in the transverse direction near the crack tip. If the volume content of rubber particles is sufficiently high [42], the state of stress changes from plane-strain to plane-stress [76]. As a result, the size of plastic zone in the surrounding matrix increases, which permits more energy-absorption ahead of the crack tip and hence increases the fracture toughness [77, 78, 79, 76]. Such a cavitation process is observed to cease abruptly along the fracture surface, when the transition from quasi-static to dynamic crack growth occurs [39, 42]. Toughness of the modified polymer is measured to be similar to that of the untoughend polymer in this case. Correlating the rate-dependence in the occurrences of these instabilities, a reasonable hypothesis is that the transition in fracture modes could be attributed to the competition between the voiding process in the cavitation zone and the rate of crack propagation. In other words, the possibility of occurrence of an instability depends on whether the volume of material around the crack tip has enough time to be sufficiently toughened to prevent a fast brittle fracture.

In this chapter, we demonstrate a finite-element modeling of crack behaviors in toughened polymers by coupling the classical void nucleation theory [80, 81, 82] to a cohesive-zone model. Instead of a deterministic traction-separation law, the cohesive elements were allowed to be toughened during the loading process and finally switch from a brittle mode to a toughened mode, associated with a re-selection of corresponding traction-separation

law. We showed that the instabilities in crack growth with similar characteristics to experimental observations could be naturally captured in this model. And it is also demonstrated that by a further assumption of spatial discrepancy in rubber concentration, the crack exhibited stochastic signs in behavior.

4.2 Numerical approach

4.2.1 Cohesive-zone

In the model developed in this chapter, it is assumed that void nucleation within the adhesive layer, triggered by a tensile stress, allows relaxation of the hydrostatic stress state at the crack tip and permits plastic deformation that results in an enhanced toughness of the adhesive layer [76, 83]. The rubber particles within a toughened epoxy are expected to cavitate in response to a local hydrostatic pressure. However since we focus on normal tractions across an interface within the framework of a cohesive-zone model, we adapt the model with formulation in terms of normal stresses [80, 81, 82]:

$$\dot{\varrho} = \Omega(\sigma)\varrho_r \exp\left(-\frac{4\gamma^3 F_v}{\sigma^2 k_{\mathrm{B}} T}\right) \quad , \tag{4.1}$$

where σ is the normal traction, $\Omega(\sigma)$ is a traction dependent probability of nucleation, ϱ_r is the number of rubber particles per unit volume, γ is the free-surface energy associated with void growth, F_v is a dimensionless quantity geometrical factor dependent upon the nucleation site. Although the exact forms of $\Omega(\sigma)$ are slightly different in each model, there is a consensus that the exponential term had a dominant influence in the nucleation rate. The exponential term is associated with thermal activation.

In this study, we adapt the model developed by Raj [81] such that $\Omega(\sigma)$ was inversely proportional to σ. It is assumed that the toughening mechanism occurs when the voids reach a critical density ϱ_o; if the conditions for matrix failure occur before the critical void density is reached, then brittle fracture occurs. Therefore, Eqn. 4.1 can be rewritten in the form of:

$$\frac{\dot{\varrho}}{\varrho_o} = \frac{\varrho_r}{\varrho_o}\frac{\omega}{\sigma} \exp\left(-\frac{\phi}{\sigma^2}\right) \quad , \tag{4.2}$$

where ω and ϕ are material constants controlling the nucleation rate. Spatial nonhomogeneity in rubber particle density, ϱ_r, is further assumed in our model, which leads to a nonuniform distribution of nucleation rate in the polymer. At each point, the time of occurrence of the brittle-toughened transition, t_T, is given implicitly by

$$\frac{\varrho}{\varrho_o} = \int_0^{t_T} \chi \frac{\omega}{\sigma(t)} \exp\left(-\frac{\phi}{\sigma^2(t)}\right) dt = 1 \quad , \tag{4.3}$$

where ϱ is the current void density and $\sigma(t)$ is the stress history at this position. This nucle-

ation mechanism was embedded in to the property definition of cohesive elements through the user-defined subroutine, where $\chi = \varrho_r/\varrho_o$ was assigned as a dimensionless, uniformly distributed random variable between zero to maximum, with a mean of χ_m.

Numerical simulations on the DCB geometry were conducted with ABAQUS/Standard in a plane-stress, implicit dynamic mode. The geometry for the finite-element calculations is shown in Fig. 4.1. Two identical elastic beams with Young's modulus, $\bar{E}$, and density, ρ, are clamped on one side, and the ends on the other side are separated with a finite displacement rate $\dot{\Delta}$. A layer consists of cohesive elements was placed between the two beams from the clamped end to the position at a distance $a_0 = 20h$ from the other end in the unloaded geometry (Fig. 4.1(a)), where h was the thickness of each beam. The toughened polymeric adhesive layer was modelled with cohesive elements. Due to the symmetry conditions of the geometry, only mode-I fracture need to be taken into consideration in this study. The cohesive layer was assigned a finite thickness, h_c, such that $h_c/h = 5 \times 10^{-4}$. As the crack propagating along the interface, the crack length was measured as the horizontal distance from the crack-tip to the end of each beam, as shown in Fig. 4.1(b).

Traction-separation laws associated with the brittle and toughened modes are shown in Fig. 4.2. A linear-hardening cohesive law $\sigma = f_b(\delta)$ is assigned to the brittle mode. If the loading-rate is high enough, then void nucleation would not have enough time to trigger the toughened mode such that the traction reaches $\hat{\sigma}_b$ before t_T. Brittle fracture occurs with a corresponding displacement δ_b in this case. The toughness associated with this brittle fracture mode is $\Gamma_b = 0.5\hat{\sigma}_b\delta_b$. On the other hand, if the toughened mode is triggered before the occurrence of brittle fracture, then the normal stress in the polymer is assumed to remain at a fairly constant level $\hat{\sigma}_t$ until the element fails at a critical displacement δ_t. The corresponding toughness for this toughened mode is then given by $\Gamma_t = (1-0.5\hat{\sigma}_t/\hat{\sigma}_b)\hat{\sigma}_t\delta_t$. In summary, the stress acting on the cohesive element can be expressed in the form of Eqn. 3.8 as

$$\sigma = \iota f(\delta) \ , \tag{4.4}$$

where

$$f = \begin{cases} f_b & \text{if } \varrho < \varrho_0 \\ f_t & \text{if } \varrho \geq \varrho_0 \end{cases} \tag{4.5}$$

and

$$\iota = \begin{cases} 0 & \text{if } \; f = f_x \; , \; \mathcal{W} \geq \Gamma_x \\ 1 & \text{otherwise} \end{cases} \tag{4.6}$$

with subscript $x = b$ or t. In this particular study, we assumed that the cohesive elements would not undergo an unloading process in either the brittle or the toughened mode, in order to minimize the severe computational instabilities at the transitions between quasi-static crack growth and dynamic fracture.

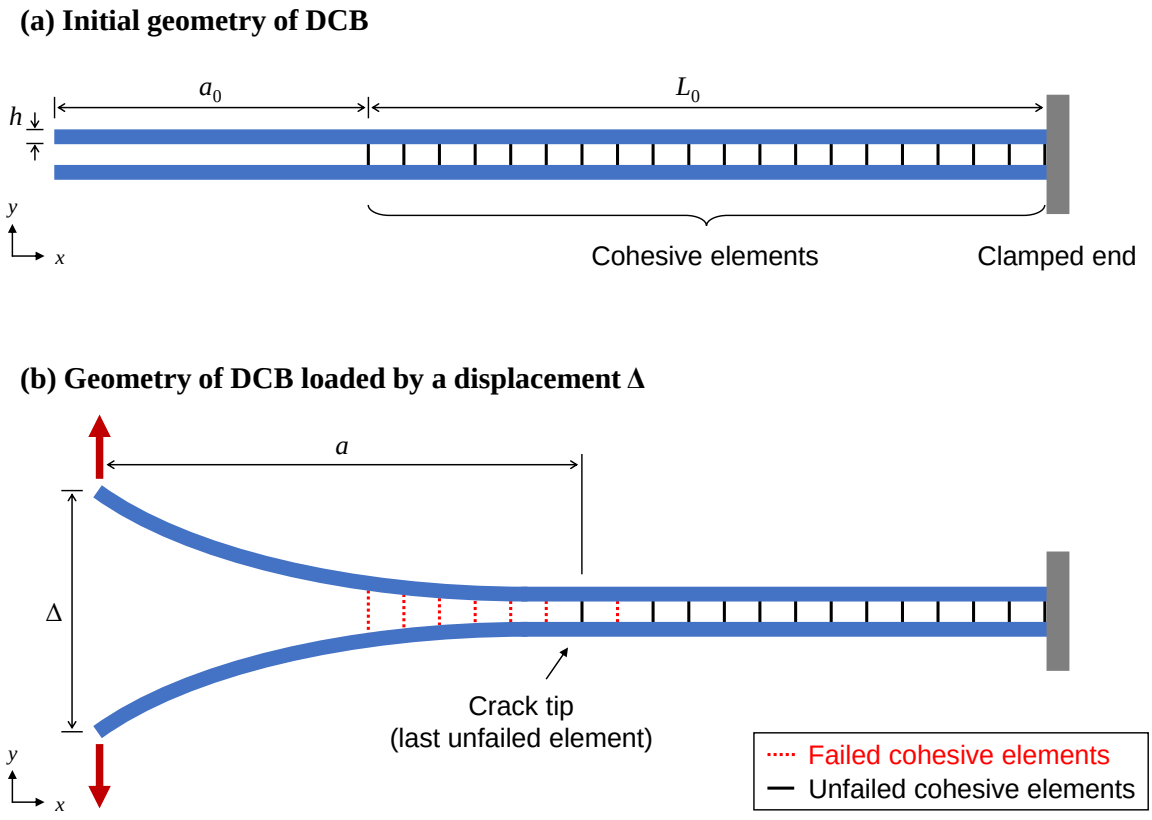

Figure 4.1: **(a)** Double-cantilever beam geometry with arms of thickness h is used for the cohesive-zone modeling of stick-slip fracture. The initial crack length is $a_o = 20h$, and the clamped end is far away from the crack-tip with $L_o = 200h$. **(b)** The beams are loaded by a displacement at a constant rate. Crack-tip is defined as being the location of the last unfailed element, and crack length a is measured as the horizontal distance from the loading to the crack-tip.

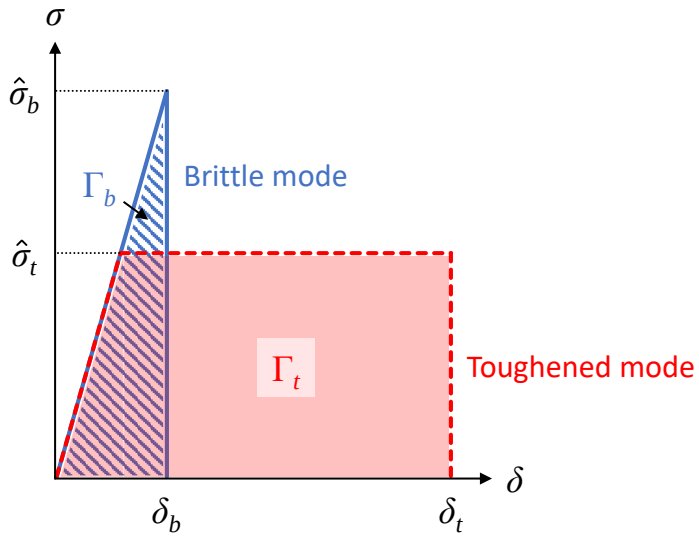

Figure 4.2: A linear traction-separation law with critical traction $\hat{\sigma}_b$ and displacement δ_b is assigned for the brittle mode. For the toughened mode, a law with constant peak stress $\hat{\sigma}_t$ and critical displacement δ_t is used. Both cohesive laws share the same initial slope and unloading is avoided to minimize computational difficulties.

4.2.2 Dimensional analysis

On the basis of the cohesive-zone model we set up in the preceding section, dimensional analysis can be performed with all the variables involved in this problem. From the angle of experimental observations, reaction force and crack length associated with displacement are crucial in the study. In general, the crack length a and the reaction force P should be of the form

$$(P, a) = F\left(h, \Delta, \dot{\Delta}, \rho, \bar{E}, \chi_m, \omega, \phi, \hat{\sigma}_b, \delta_b, \Gamma_b, \hat{\sigma}_t, \delta_t, \Gamma_t\right) \quad , \tag{4.7}$$

where (i). h characterizes the geometry since the ratio $a_0/h = 50$ is fixed; (ii). Δ and $\dot{\Delta}$ characterize the loading applied on the system; (iii). ρ and $\bar{E}$ are material properties of the beams; (iv). χ_m, ω and ϕ are factors controlling the nucleation rate; and (v). $\hat{\sigma}_b$, δ_b, Γ_b, $\hat{\sigma}_t$, δ_t and Γ_t are parameters of the cohesive laws and corresponding cohesive lengths are given by $\xi_b = \bar{E}\delta_b^2/\Gamma_b$ and $\xi_t = \bar{E}\delta_t^2/\Gamma_t$.

Dimensional analysis for this problem shows that the normalized crack length and reaction force should be of the form

$$\frac{P}{(\bar{E}h\Gamma_b)^{\frac{1}{2}}} = F_p\left(\frac{\Delta\bar{E}^{\frac{1}{2}}}{(h\Gamma_b)^{\frac{1}{2}}}, \frac{\dot{\Delta}\hat{\sigma}_b\bar{E}^{\frac{1}{2}}}{\chi_m\omega(h\Gamma_b)^{\frac{1}{2}}}, \frac{\bar{E}\hat{\sigma}_b^2}{\rho h^2\chi_m^2\omega^2}, \frac{\phi}{\hat{\sigma}_b^2}, \frac{\bar{E}}{\hat{\sigma}_b}, \frac{\xi_b}{h}, \frac{\Gamma_t}{\Gamma_b}, \frac{\hat{\sigma}_t}{\hat{\sigma}_b}\right) \tag{4.8}$$

and

$$\frac{a}{h} = F_a\left(\frac{\Delta\bar{E}^{\frac{1}{2}}}{(h\Gamma_b)^{\frac{1}{2}}}, \frac{\dot{\Delta}\hat{\sigma}_b\bar{E}^{\frac{1}{2}}}{\chi_m\omega(h\Gamma_b)^{\frac{1}{2}}}, \frac{\bar{E}\hat{\sigma}_b^2}{\rho h^2\chi_m^2\omega^2}, \frac{\phi}{\hat{\sigma}_b^2}, \frac{\bar{E}}{\hat{\sigma}_b}, \frac{\xi_b}{h}, \frac{\Gamma_t}{\Gamma_b}, \frac{\hat{\sigma}_t}{\hat{\sigma}_b}\right) \tag{4.9}$$

In this chapter, our focus is on the effects of loading rate, $\dot{\Delta}\hat{\sigma}_b\bar{E}^{\frac{1}{2}}/\chi_m\omega(h\Gamma_b)^{\frac{1}{2}}$, and toughening level, Γ_t/Γ_b, on the crack behavior. Therefore, other non-dimensional variables are kept constant for the calculations presented in following sections of this chapter for simplification, as listed in Table 4.1. The amount of variables in Eqns. 4.8 and 4.9 are then reduced to

$$\frac{P}{(\bar{E}h\Gamma_b)^{\frac{1}{2}}} = F_p\left(\frac{\Delta\bar{E}^{\frac{1}{2}}}{(h\Gamma_b)^{\frac{1}{2}}}, \frac{\dot{\Delta}\hat{\sigma}_b\bar{E}^{\frac{1}{2}}}{\chi_m\omega(h\Gamma_b)^{\frac{1}{2}}}, \frac{\Gamma_t}{\Gamma_b}\right) \tag{4.10}$$

and

$$\frac{a}{h} = F_a\left(\frac{\Delta \bar{E}^{\frac{1}{2}}}{(h\Gamma_b)^{\frac{1}{2}}}, \frac{\dot{\Delta}\hat{\sigma}_b \bar{E}^{\frac{1}{2}}}{\chi_m \omega (h\Gamma_b)^{\frac{1}{2}}}, \frac{\Gamma_t}{\Gamma_b}\right) \tag{4.11}$$

It should be noted that the normalized cohesive length associated to the brittle model was kept at $\xi_b/h = 0.8$, as given in Table. 4.1, such that the LEFM conditions were met for brittle fracture. To ensure the accuracy of calculation, mesh size were kept small enough ($\leq 0.05\xi_b$) to guarantee uncertainties not beyond the limits of error bars in all figures provided in following sections. Normalized reaction force and crack length are plotted as functions of displacement in Fig. 4.3 (a) and (b) for the crack growth associated with brittle mode only. The simulation results are compared with the analytical solutions obtained from LEFM [84] for verification of the accuracy of finite-element calculations presented in this chapter.

Table 4.1: In this chapter, we concentrate our attention on the effects of loading rates and toughening levels on the crack behavior, therefore other non-dimensional variables in Eqns. 4.8 and 4.9 are kept constant throughout this chapter to simplify the calculation.

Non-dimensional variable	**Preset value**
$\bar{E}\hat{\sigma}_b^2/\rho h^2 \chi_m^2 \omega^2$	1.44×10^{14}
$\phi/\hat{\sigma}_b^2$	1.5625×10^{-2}
$\bar{E}/\hat{\sigma}_b$	4166.7
ξ_b/h	0.8
$\hat{\sigma}_t/\hat{\sigma}_b$	0.5

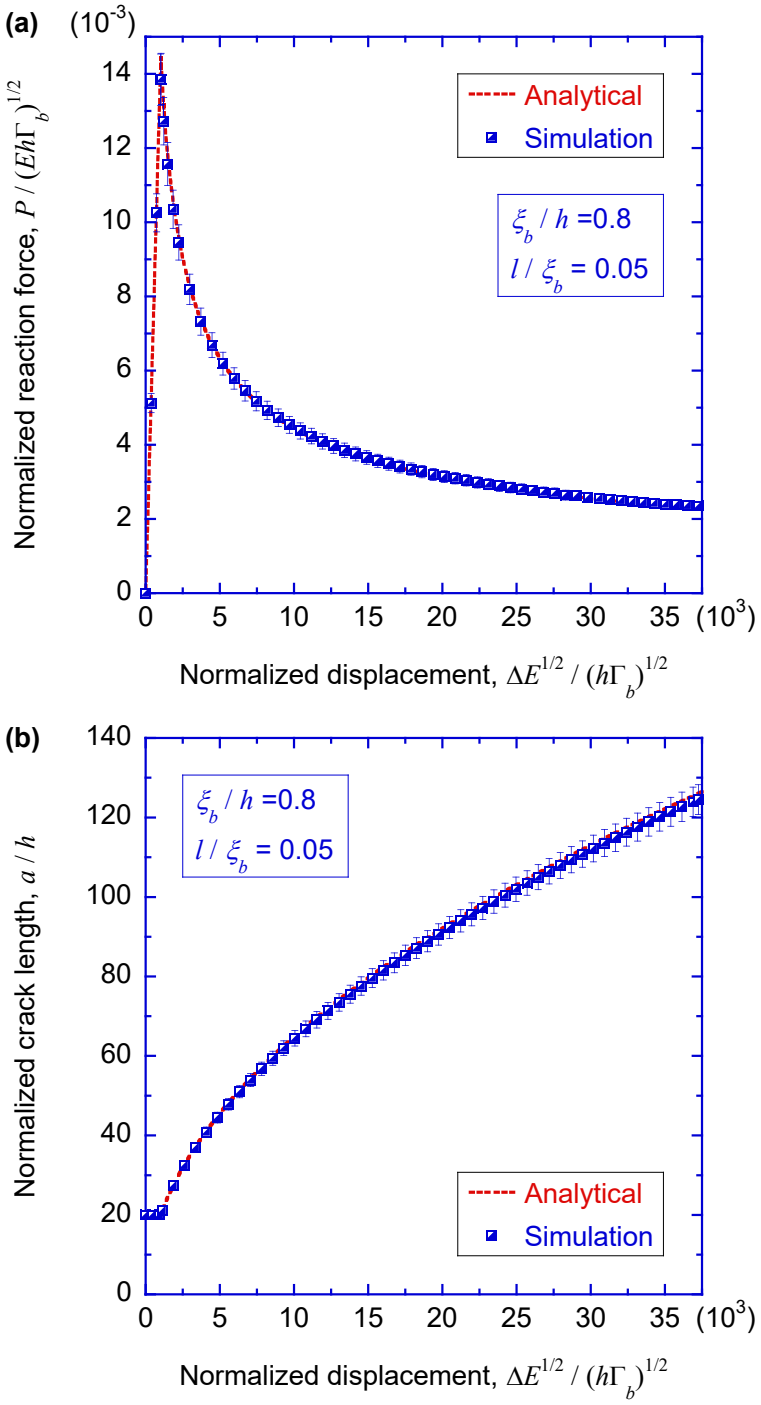

Figure 4.3: Normalized reaction force **(a)** and crack length **(b)** are plotted as functions of displacement for crack growth associated with the brittle mode only. The simulation results are compared with analytical solutions obtained from LEFM to verify the accuracy of finite-element calculations in this chapter. The discrepancies are less than 5% for reaction force and 3% for crack length.

4.3 Results and discussion

4.3.1 Effects of loading rates

Functions 4.10 and 4.11 are plotted in Fig 4.4 (a) and (b), respectively. The normalized reaction force and crack length are plotted with respect to the loading displacement, with a constant value of toughening $\Gamma_t/\Gamma_b = 5$ and varying normalized loading displacement rate $\dot{\Delta}\hat{\sigma}_b\bar{E}^{\frac{1}{2}}/\chi_m\omega(h\Gamma_b)^{\frac{1}{2}}$. For slow displacement rates, $\dot{\Delta}\hat{\sigma}_b\bar{E}^{\frac{1}{2}}/\chi_m\omega(h\Gamma_b)^{\frac{1}{2}} \leq 3.7$, only quasi-static crack growth associated with the toughened mode has been observed. As increasing the loading rate, dynamic propagations suddenly appear, corresponding to the abrupt drops in reaction force and increments in crack length in Fig 4.4 (a) and (b). The crack growth exhibits a quasi-static/dynamic pattern, with an increasing tendency for dynamic jumps to occur at higher loading rates. A limiting case of $\dot{\Delta}\hat{\sigma}_b\bar{E}^{\frac{1}{2}}/\chi_m\omega(h\Gamma_b)^{\frac{1}{2}} = 5.6 \times 10^4$ is also plotted, corresponding to the crack behavior under an excessively fast loading rate. In this case, the crack propagates so fast that the voiding mechanism has never have enough time to toughen the material, and hence the curves are in agreement with those in Fig. 4.3, showing that the crack growth is only associated with the brittle mode.

Except this limiting case, the cohesive elements close to the crack tip have been sufficiently toughened during the initial loading stage, therefore the crack grows in a quasi-static fashion at first, until the crack tip reaches a region where the elements has not been ready to switch to the toughened mode. The existence of such a region is owing to a fast crack growth rate associated with the loading speed, or to the inhomogeneous density of nucleation sites in the material, which is modelled by the random distribution of χ assigned to each individual cohesive element. Figure 4.5 shows a histogram that includes a count for amount of cohesive elements which are assigned a χ value, normalized by the average χ_m, for each cell range within $0 \leq \chi \leq 2\chi_m$, showing that the distribution is nearly uniform. When the instable transition happens, the crack jumps dynamically to a location associated with the toughness of the brittle mode, leading to a sudden decrease in reaction force at the loaded ends of DCB. For example, in Fig. 4.4, for $\dot{\Delta}\hat{\sigma}_b\bar{E}^{\frac{1}{2}}/\chi_m\omega(h\Gamma_b)^{\frac{1}{2}} = 5.6$, a dynamic jump occurs at a normalized displacement of $\Delta\bar{E}^{\frac{1}{2}}/(h\Gamma_b)^{\frac{1}{2}} = 7.3$, where the crack length increases abruptly from $a/h = 36.2 \pm 1.1$ to $a/h = 81.4 \pm 2.5$, and the normalized reaction force drops correspondingly from to $P/(\bar{E}h\Gamma_b)^{\frac{1}{2}} = 17.2 \pm 0.9$ to $P/(\bar{E}h\Gamma_b)^{\frac{1}{2}} = 1.6 \pm 0.1$. Similar behaviors appear twice for a higher loading rate $\dot{\Delta}\hat{\sigma}_b\bar{E}^{\frac{1}{2}}/\chi_m\omega(h\Gamma_b)^{\frac{1}{2}} = 11.2$, within the current range of loading displacement on this geometry.

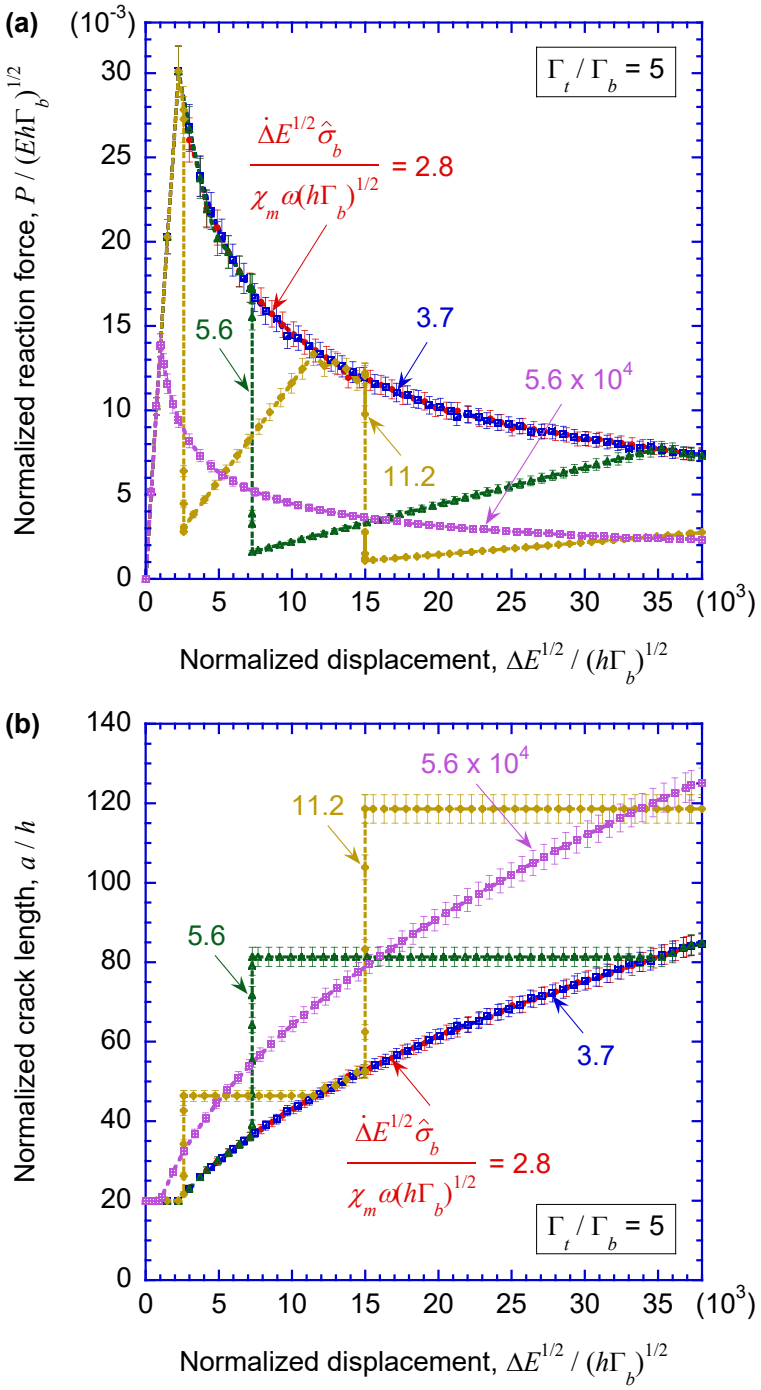

Figure 4.4: Representative plots of **(a)** normalized force and **(b)** crack length as functions of displacement. The toughening is held at a constant level of $\Gamma_t/\Gamma_b = 5$. If the loading rate is slow enough, the crack grows in a quasi-static fashion associated with the toughened mode only, however under an exceedingly high loading rate $\dot{\Delta}\hat{\sigma}_b\bar{E}^{\frac{1}{2}}/\chi_m\omega(h\Gamma_b)^{\frac{1}{2}} = 5.6 \times 10^4$ the toughening mechanism is never activated. With intermediate loading rates, the crack exhibits both quasi-static and dynamic growths, and occurrences of dynamic jumps tend to be more frequent as increasing the loading rate.

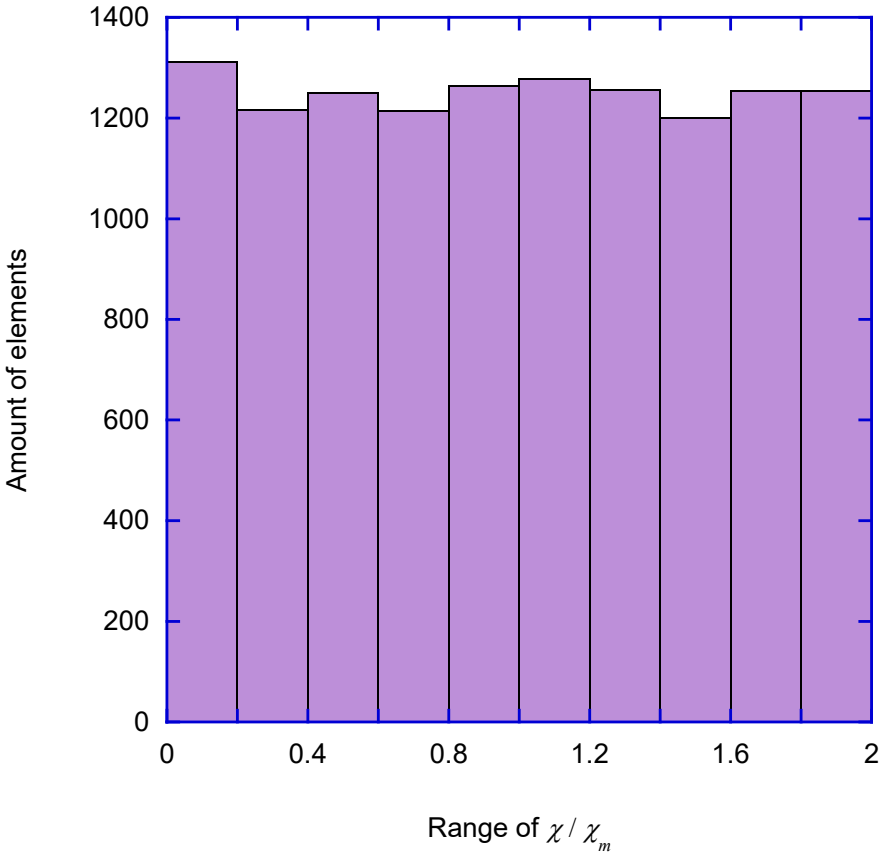

Figure 4.5: A histogram displays statistics of χ values assigned to the cohesive elements, showing that the random variable χ distributes uniformly between 0 and $2\chi_m$, corresponding to a mean value of χ_m and a standard deviation of $\chi_m/\sqrt{3}$.

The normalized work, $W/h\Gamma_b$, applied to the DCB system is given by the integral of reaction force over the displacement:

$$\frac{W}{h\Gamma_b} = \frac{1}{h\Gamma_b}\int P d\Delta = \int \frac{P}{(\bar{E}h\Gamma_b)^{\frac{1}{2}}}\, d\left(\frac{\Delta \bar{E}^{\frac{1}{2}}}{(h\Gamma_b)^{\frac{1}{2}}}\right) \quad , \tag{4.12}$$

i.e. the area under each curve in Fig. 4.4 (a). Comparing the load-displacement curve for $\dot{\Delta}\hat{\sigma}_b\bar{E}^{\frac{1}{2}}/\chi_m\omega(h\Gamma_b)^{\frac{1}{2}} = 5.6$ and that for the limiting case $\dot{\Delta}\hat{\sigma}_b\bar{E}^{\frac{1}{2}}/\chi_m\omega(h\Gamma_b)^{\frac{1}{2}} = 5.6 \times 10^4$ such that the cohesive elements are completely untoughened, the amounts of work applied to the system are $W/h\Gamma_b = 142.0 \pm 7.2$ and $W/h\Gamma_b = 57.8 \pm 3.0$ till the loading displacement at which crack jump occurs ($\Delta\bar{E}^{\frac{1}{2}}/(h\Gamma_b)^{\frac{1}{2}} = 7.3$), respectively. Such a discrepancy leads to an "overshoot" in the crack length after the dynamic jump, which can be observed in Fig. 4.4 (b). The crack tip stops at a position of $a/h = 81.4 \pm 2.5$ after the dynamic propagation, however the crack length associated with pure brittle mode fracture at this

corresponding loading displacement is $a/h = 54.7 \pm 1.7$.

Due to this overshoot in crack length, the energy-release rate at the crack tip is lower than both Γ_t and Γ_b after each dynamic jump. The crack is then arrested with no increment in size such that the nucleation mechanism has enough time to activate the toughened mode near the crack tip, as it does during the initial loading stage. Therefore, quasi-static growth continues when the energy-release rate reaches Γ_t, until interrupted again by another jump. The complete quasi-static/dynamic/arrest cycle is displayed in Fig. 4.6.

A statistical conclusion is that by increasing the loading rate, dynamic jumps tend to appear more frequently, as shown, representatively, in Fig. 4.4. However, for each individual test the pattern of quasi-static/dynamic crack propagation seems to be random and not to be subjected to a certain periodicity, due to the variance in the value of χ parameter (see Eqn. 4.3) assigned to each cohesive element. Such a phenomenon is manifested in Fig. 4.7 that simulation results with the same loading parameters and material properties exhibits completely different patterns. For statistical purposes, simulations were repeated five times at each loading rate for a maximum displacement $\Delta \bar{E}^{\frac{1}{2}}/(h\Gamma_b)^{\frac{1}{2}} = 38$. The statistics of occurrences of instabilities for each loading rate are provided in Table 4.2. There is evidence that the quasi-static to dynamic crack propagation transitions are more likely to occur at higher loading rates. These results are in good agreement with the experiments by Sun et al. [40].

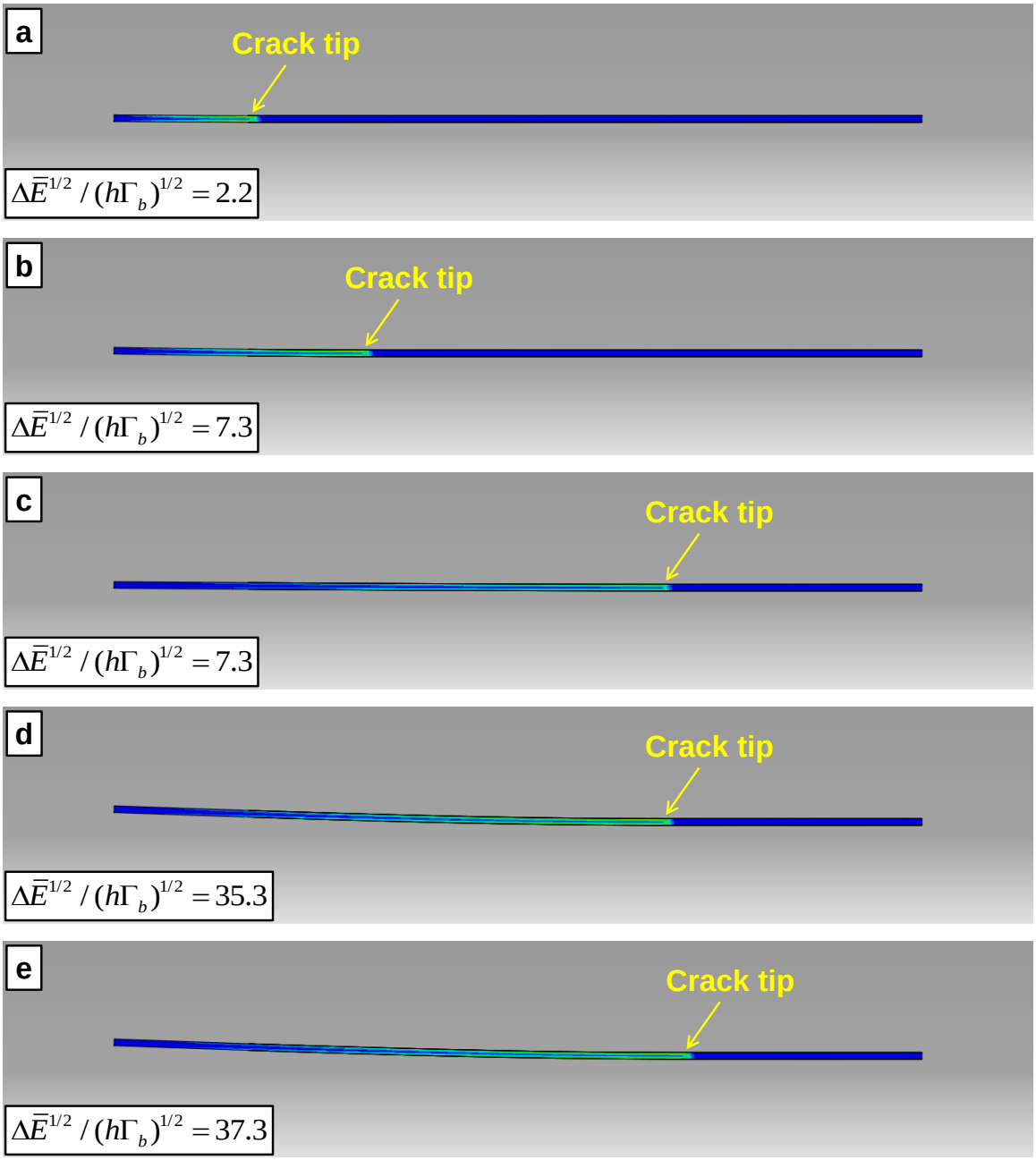

Figure 4.6: Contour plots of von Mises stress at each stage of a crack propagation cycle. Only half of the DCB is plotted due to symmetry. **(a)** Quasi-static crack starts to propagate when the energy-release rate reaches the toughness corresponding to the toughened mode, until **(b)** the crack tip reaches a region which has not been sufficiently toughened. Then **(c)** the crack jump forward dynamically, without additional work applied to the system (notice the same displacement before and after the jump). The crack is then **(d)** arrested at a position associated with the brittle mode toughness, until **(e)** another cycle started with quasi-static growth.

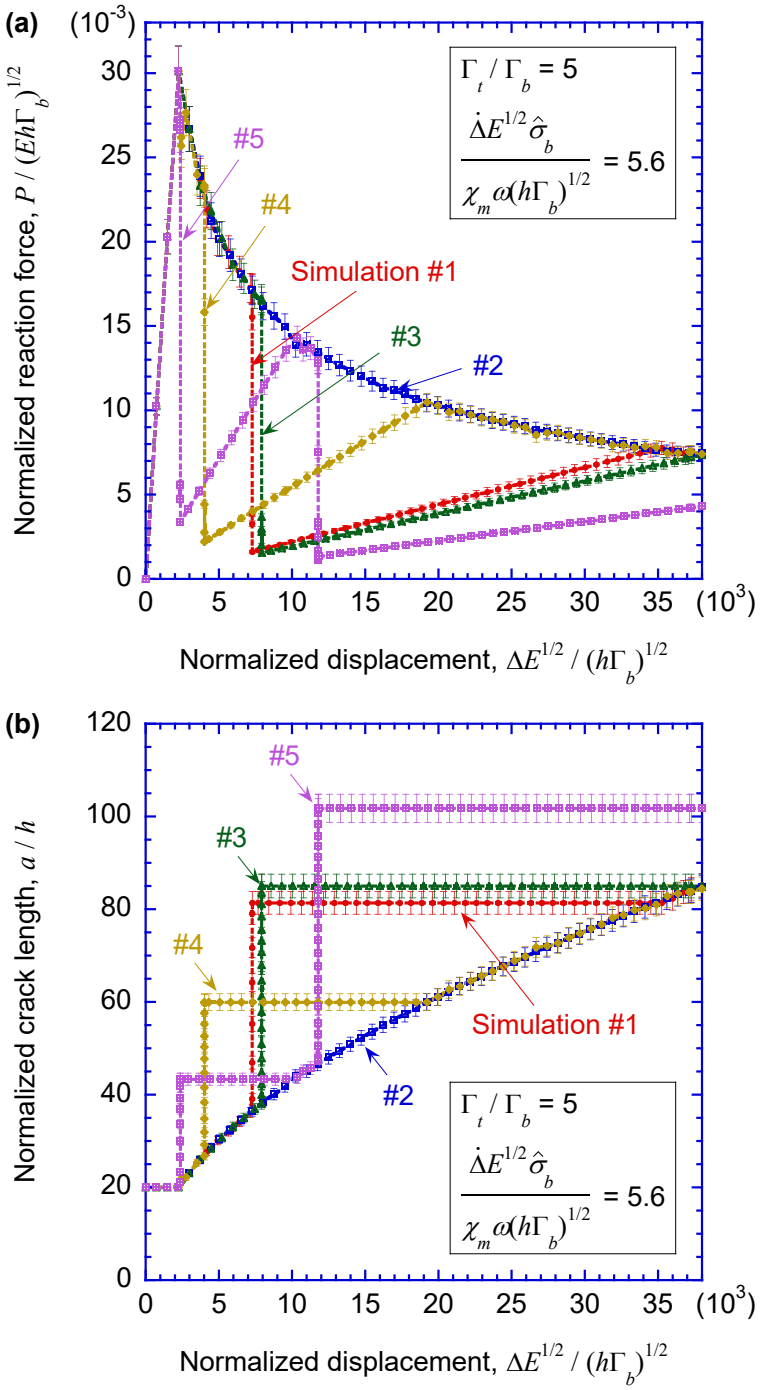

Figure 4.7: Simulations are repeated with the same loading parameters and material properties. The crack exhibits random quasi-static/dynamic propagation patterns in different tests, which is caused by the stochastic spatial variance in nucleation rate assigned to each cohesive element.

Table 4.2: Statistics of occurrence of dynamic jumps under different loading rates. The DCB is loaded to a maximum normalized displacement $\Delta \bar{E}^{\frac{1}{2}}/(h\Gamma_b)^{\frac{1}{2}} = 38$ and the toughening level is kept at $\Gamma_t/\Gamma_b = 5$ in every test. There is evidence that the quasi-static crack growth are more frequently interrupted by dynamic jumps at higher loading rates, which agrees with experimental observations.

Normalized loading rate $\dot{\Delta}\hat{\sigma}_b\bar{E}^{\frac{1}{2}}/\chi_m\omega(h\Gamma_b)^{\frac{1}{2}}$	**Average times of dynamic jumps** (occurrences/test)	**Standard deviation** (occurrences/test)
2.8	0.4	0.5
3.7	0.6	0.5
5.6	1.0	0.7
11.2	2.0	0.0

4.3.2 Effects of toughening levels

Recent experimental observations in rubber-toughened polymers demonstrated a positive correlation between the rubber particle content and the fracture toughness associated with the toughened mode. Polymers with different rubber contents, and correspondingly different levels of toughening, were used as adhesives in a DCB geometry, loaded at a constant displacement rate. It was found that when the rubber-toughening reached a certain level, the instabilities in crack growth could be eliminated such that only quasi-static crack growth was observed [42]. This phenomenon can be attributed to the fact that a higher volume fraction of rubber particles speeds up the toughening process, since there are more nucleation sites available for voiding and stress relaxation. In addition to this, it is shown in this section that a tougher system itself can also reduce the possibility of dynamic jumps to happen.

Simulation of this phenomenon can be achieved by fixing the loading rate but varying the ratio between the toughened and brittle fracture toughnesses, Γ_t/Γ_b, in Eqns. 4.10 and 4.11. Representative results are exampled in Fig. 4.8, where the value of Γ_t/Γ_b varies from 5 to 30, corresponding to different levels of rubber-toughening, and the DCB are loaded with a constant displacement rate $\dot{\Delta}\hat{\sigma}_b\bar{E}^{\frac{1}{2}}/\chi_m\omega(h\Gamma_b)^{\frac{1}{2}} = 5.6$. Results of finite-element modeling consist with the experimental observations qualitatively. In Fig. 4.8, dynamic jumps in crack growth are observed at lower levels of toughening, $\Gamma_t/\Gamma_b = 5$ and 10; but do not occurs for $\Gamma_t/\Gamma_b \geq 15$. Statistical results obtained from five simulations at each toughening level are given in Table 4.3, also indicating a negative correlation between frequency of these jumps and the toughening. This observation could be correlated with the results presented in Section 4.3.1. With the same displacement rate, Fig. 4.8 (b) shows that the crack velocity is effectively slowed down by increasing the value of Γ_t/Γ_b such that the toughening mechanism has advantage competing with the crack propagation process, therefore the system is stabilized accordingly.

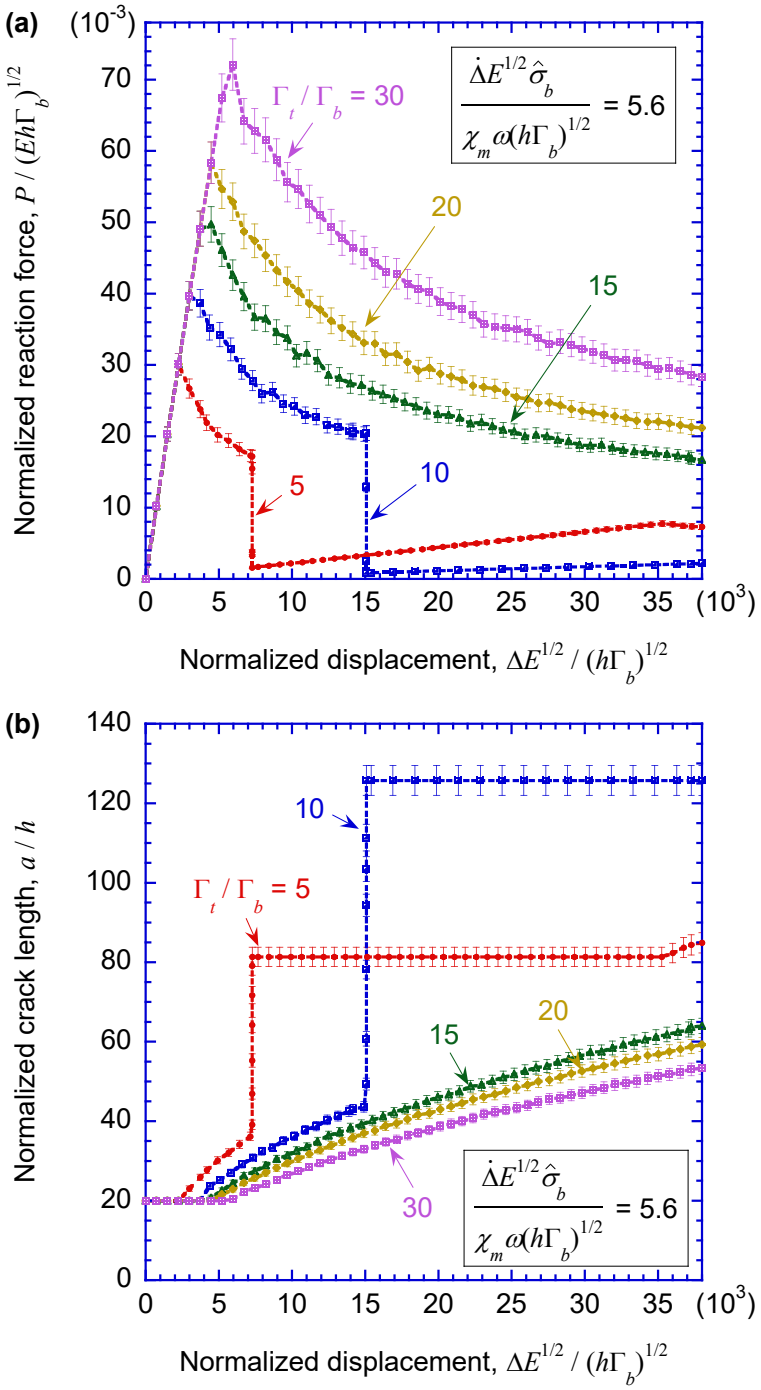

Figure 4.8: Representative plots of **(a)** normalized force and **(b)** crack length as functions of displacement for different levels of toughening. The loading rate of all the simulations are the same. The crack exhibits both quasi-static and dynamic growth when $\Gamma_t/\Gamma_b \leq 10$ and grows in the quasi-static fashion only when $\Gamma_t/\Gamma_b \geq 15$ in these tests, showing that instabilities are more unlikely to occur at higher levels of toughening.

Table 4.3: Statistics of occurrence of dynamic jumps for different levels of toughening, Γ_t/Γ_b. The DCB is loaded to a maximum normalized displacement $\Delta\bar{E}^{\frac{1}{2}}/(h\Gamma_b)^{\frac{1}{2}} = 38$ with a constant loading rate $\dot{\Delta}\hat{\sigma}_b\bar{E}^{\frac{1}{2}}/\chi_m\omega(h\Gamma_b)^{\frac{1}{2}} = 5.6$ in every test. Dynamic crack jumps are more likely to occur in a weakly toughened material.

Level of toughening Γ_t/Γ_b	**Average times of dynamic jumps** (occurrences/test)	**Standard deviation** (occurrences/test)
5	1.0	0.7
10	1.0	0.0
15	0.4	0.5
20	0.4	0.5
30	0.2	0.4

4.4 Summary

In this chapter, we have outlined a cohesive-zone based finite element model to explore the rate-dependent instabilities in crack growth in rubber-toughened polymers. Toughening mechanism is attributed to the plastic deformation associated with relaxation of hydrostatic stress near the crack tip, which is caused by the stress-driven void nucleation at the rubber particles. In a displacement-controlled DCB geometry, rubber-toughened quasi-static crack growth is interrupted by stochastic occurrences of dynamic, brittle mode crack tip jumps, which has been more frequently observed under a higher loading rate or a lower level of rubber-toughening. No applied work to the system is required during these dynamic jumps.

The modeling of crack behaviors in such a system combines the classical nucleation theory with cohesive-zone finite-element analysis, based on the assumption that transitions in fracture modes are owing to the choice between traction-separation laws associated with brittle and rubber-toughened fracture modes, respectively, affected by current density of void nucleations. It has been demonstrated that the simulation results are in good agreement with experimental observations in regards to both the effects of loading rate and rubber-toughening levels. A slow loading rate prolongs the time available for the toughening mechanism. A higher volume content of rubber particles permits more energy-absorption of the toughened mode, and at the same time speed up the cavitation process since more void nucleation sites are available per unit volume. All these factors reduce the possibility of occurrences of brittle crack jumps. The stochastic nature of crack behavior in this system has also been captured in this model, with a further assumption of spatial discrepancy in rubber content density, leading to non-uniform distribution of nucleation rate along the crack path. Methodology of this chapter also shows potential utility of cohesive-zone approach in the analysis of other systems associated with time-dependent intrinsic or extrinsic toughening mechanisms such as creep rupture of fiber-reinforced composites [85] or subcritical microcracking in brittle solids[86].

CHAPTER 5

Conclusions

In fracture mechanics, stochastic characteristics arise from various aspects. Cracks are commonly initiated from flaws in material, therefore cracking is usually considered as a stochastic process. Crack growth in brittle materials is always associated with thermally-activated processes such as bond breaking or pullout of molecules. In ductile materials, the damage in the highly-stressed volume ahead of the crack tip involves processes such as cleavage and void coalescence. The analysis of these mechanisms always refers to statistical mechanics. Similar processes also happen in many intrinsic or extrinsic toughening mechanisms such as micro-cracking toughening, rubber-cavitation toughening, ligament bridging and fiber toughening. Furthermore, crack patterns, densities and system reliabilities against fracture have also been studied statistically in numerous researches. In this dissertation, time and rate-dependent fracture behaviors associated with stochastic characteristics have been studied from the perspectives of both experiments and finite-element modeling.

In brittle materials, it is frequently observed that the crack can grow kinetically with driving-force sensitive velocities, which is a typical thermally-activated fracture process associated with stochastic bond breaking mechanisms at atomistic or molecular scales. The typical range of crack velocity in this condition is from $\approx$ m/s down to $\approx$ nm/s, such that dynamic effects are negligible in this process. For a kinetically propagating crack, the crack velocity exponentially diminishes with decreasing energy-release rate, until the growth stops at a threshold driving-force. There is also a higher threshold associated with the onset of dynamic crack propagations. By correlating the kinetic crack velocity and the corresponding energy-release rate, material properties associated with the fracture process, such as activation energy and bond spacings, can be estimated based on the model developed by Lawn. In Chapter 2, we studied the behavior of kinetic channeling cracks in a nano-composite polymeric thin film, coating on a stiff primer on a thick polycarbonate substrate. We demonstrated a technique to calculate the crack velocity as a function

of energy-release rate. It was recognized that the energy-release rate was sensitive to the crack depth, spacings to the neighboring cracks, the system geometry, elastic properties of material of each layer and residual strain in the cracked layer. The storage moduli, loss moduli and loss tangent were determined by nano-indentation DMA, for topcoat and primer, and DMA, for the polycarbonate substrate. The crack depth could be determined by SEM examination of cross-sections made by FIB milling down from sample surface. It was demonstrated that at a temperature sufficiently lower than the glass-transation temperature of the primer, the penetration depth of the crack was limited by the topcoat/primer interface, which was in consistent with the predictions of LEFM, given that the topcoat was bonded to a stiffer primer layer. However, at an elevated temperature close to the glass-transition temperature, creep of the primer layer led to an additional relaxation of stress, which was reflected on the SEM examinations, and correspondingly increased the energy-release rate of the channeling crack. The positions of crack tips were recorded by a high-speed camera in the experiments. The crack velocities were were measured using DIC, together with the distances to both of its neighboring cracks, and the current applied strain. Residual strains in the topcoat were determined by measuring the crack-opening displacements, and comparing with them to numerical calculations. For this particular system, the obtained crack velocity – energy-release rate curve showed characteristics of a thermally-activated fracture process, with a threshold toughness of about 7 J/m^2 and an estimated activation energy of about 0.6 eV/bond. Absence of stress-corrosion cracking was also demonstrated for the system, indicating that the bond-ruptures were less likely to occur at the silicon-oxygen bonds.

In Chapter. 3, we have outlined a use of stochastic cohesive-zone model to simulate kinetic crack growth. The model was originally formulated in terms of dimensions of finite-element mesh, representing the discrete nature of crack advance. However, it has been shown that if the mesh is sufficiently small compared to the cohesive length, a mesh independent result can be obtained. When the cohesive-length scale is large, the problem is controlled by the strength rather than the nominal toughness, which is beyond the assumptions of the original kinetic crack growth model. When the cohesive-length is small, the problem is controlled by singular stress field. In this case, the characteristic length is provided by the product of the cohesive length and a coefficient associated with the bond spacing and the activation energy of bond rupture. A lower bond density in the cohesive-zone, or alternatively, a small cohesive-zone containing fewer bonds, corresponds to a higher activation energy of bond rupture. As a result, the bonds tend to fail in a very narrow region near the crack tip. Conversely, if there is a dense population of bonds in the cohesive-zone,

the activation energy decreases such that the bonds tend to break in a more diffused zone ahead of the crack tip, but still smaller than the cohesive-zone. It is demonstrated that the kinetic model describes the crack velocity considerably well for the former case, and a decrease of activation energy diminishes the accuracy of the cohesive-zone calculation.

In addition to these thermally-activated fracture mechanisms associated with probabilistic processes occurring at microscopic scales, propagating cracks also exhibit stochastic phenomena at macroscopic scales in many systems. In rubber-toughened polymers, stable crack propagation associated with displacement-controlled geometry, such as DCB, is frequently observed to be interrupted by intermittent dynamic crack jumps. Occurrences of these instabilities appear to be completely random. Although in general, there is an increasing tendency for the dynamic jump to occur at higher loading rates or reduced rubber contents, there is no obvious critical rate at which this transition occurs. In a rubber-modified polymer, the toughening mechanism is attributed to cavitation due to the existence of rubber particles, which allows relaxation of hydrostatic stress near the crack tip, permits plastic deformation and results in an enhanced toughness. However, SEM examination of fracture surface shows a sign of abrupt cease of rubber-toughening when a dynamic crack jump occurs. Based on these observations, in Chapter 4 a cohesive-zone model was demonstrated to explore and simulate the crack behaviors in this system. The cohesive elements were allowed to make choice between two traction-separation laws, corresponding to the untoughened and toughened modes, respectively. The choice relied on the current void density, which was calculated based on the classical nucleation theory. It was assumed that the toughening mechanism occurred when the voids reached a critical density. If the conditions for matrix failure occurred before this critical void density was reached, then brittle fracture occurred. It was further assumed that the rubber content had spatial discrepancy, leading to a non-uniform distribution of nucleation rate along the crack path. Therefore, while the geometry was loaded at a controlled displacement rate, there was a competition between the onset of toughening mechanism and the crack propagation rate in the stressed zone ahead of the crack tip. The simulation results were in good agreement with experimental observations. A slower loading rate extended the time available for the toughening mechanism to be successfully triggered, and a higher volume content of rubber particles permitted more energy-absorption of the toughened mode and also slowed down the crack growth. The likelihood of occurrences of brittle crack jumps was conspicuously diminished under these conditions, with behavioral stochasticity owing to spatial inhomogenity of rubber concentration.

APPENDIX A

Fortran-based user-defined element subroutines

A.1 User-defined element used in Chapter 3

```
CCCCCCCCCCCCCCCCCCCCCCCCCCCCCCCCCCCCCCCCCCCCCCCCCCCCCCCCCCCCCCCCCCCCCC
C UEL.f CCZM C
C C
C THIS SUBROUTINE WILL APPLY MIX-MODE TRAPEZOIDAL CZM C
C MODEL TO A USER DEFINED ELEMENT FOR USE BY ABAQUS. C
C MODDIFIED FOR THE USE OF MODELING TIME-DEPENDENT CRACK
C BY ASSIGNING A PROBABILISTIC FRACTURE CRITERION
CCCCCCCCCCCCCCCCCCCCCCCCCCCCCCCCCCCCCCCCCCCCCCCCCCCCCCCCCCCCCCCCCCCCCC

SUBROUTINE UEL(RHS,AMATRX,SVARS,ENERGY,NDOFEL,NRHS,NSVARS,
1  PROPS,NPROPS,COORDS,MCRD,NNODE,U,DU,V,A,JTYPE,TIME,DTIME,
2  KSTEP,KINC,JELEM,PARAMS,NDLOAD,JDLTYP,ADLMAG,PREDEF,NPREDF,
3  LFLAGS,MLVARX,DDLMAG,MDLOAD,PNEWDT,JPROPS,NJPROP,PERIOD)

INCLUDE 'ABA_PARAM.INC'

DIMENSION RHS(MLVARX,*),AMATRX(NDOFEL,NDOFEL),PROPS(*),
1  SVARS(*),ENERGY(8),COORDS(MCRD,NNODE),U(NDOFEL),
2  DU(MLVARX,*),V(NDOFEL),A(NDOFEL),TIME(2),PARAMS(*),
3  JDLTYP(MDLOAD,*),ADLMAG(MDLOAD),DDLMAG(MDLOAD,*),
4  PREDEF(2,NPREDF,NNODE),LFLAGS(*),JPROPS(*)

DIMENSION C_COOR(2,4), R_COOR(2,4), R_F(8), R_MATRX(8,8),
1  UY(2),UX(2),UY_P(2),UX_P(2),CI(2),C(2),PHI(2,2),
2  STRN(2),STRT(2),SKNN(2),SKTT(2),SKNT(2),SKTN(2),FN(2),FT(2),
3  STFN(2,2),STFT(2,2),SYMBOL(2),F_CRT(2),G_I(2),G_II(2),
4  THIK(2), OVER_SHT(2),IDTF_1(2),IDTF_2(2),RR(2)

REAL*8 LAMBDAN1, LAMBDAN2, LAMBDAT1, LAMBDAT2, THLD, R_VAR, PROB
```

```
c INTEGER systime(8)
c INTEGER seed(2)

C  READ THE PROPERTIES OF CZM MODEL
SN1 = PROPS(1) !PEAK SHEAR STRESS
SN2 = PROPS(2) !PEAK SHEAR STRESS
LAMBDAN1 = PROPS(3) !SHAPE PARAMETER LAMBDA1
LAMBDAN2 = PROPS(4) !SHAPE PARAMETER LAMBDA2
DLTNC = PROPS(5) !CRATICAL SHEAR DISPLACEMENT
DLTN1 = LAMBDAN1
DLTN2 = LAMBDAN2
G_I0 = 0.5D0*(SN1*DLTN2-SN2*DLTN1+SN2*DLTNC)

ST1 = PROPS(6) !PEAK SHEAR STRESS
ST2 = PROPS(7) !PEAK SHEAR STRESS
LAMBDAT1 = PROPS(8) !SHAPE PARAMETER LAMBDA1
LAMBDAT2 = PROPS(9) !SHAPE PARAMETER LAMBDA2
DLTTC = PROPS(10) !CRATICAL SHEAR DISPLACEMENT
DLTT1 = LAMBDAT1
DLTT2 = LAMBDAT2
G_II0 = 0.5D0*(ST1*DLTT2-ST2*DLTT1+ST2*DLTTC)
SK = SN1/DLTN1 ! STIFFNESS DURING INTERPENETRATION
FC = 0.0D0 ! FRICTION COEFFICIENT

CCCCCCCCCCCCCCCCCCCCCCCCCCCCCCCCCCCCCCCCCCCCCCCCCCCCCCCCCCCCCCCCCCCCCCC
THLD = 1.0D0 !THRESHOLD
CCCCCCCCCCCCCCCCCCCCCCCCCCCCCCCCCCCCCCCCCCCCCCCCCCCCCCCCCCCCCCCCCCCCCCC

AA=SVARS(1)
C DT=SVARS(3)
AK=SVARS(5)
AG1=SVARS(6)
AG2=SVARS(7)

DT2=DTIME
X1=COORDS(1,1)
X2=COORDS(1,2)

BB1=SVARS(10)
KBB2=SVARS(11)
BB4=SVARS(13)

IF (BB1.GT.10.0D0) THEN
```

```
BB3=SVARS(12)
BB5=SVARS(14)
BB6=SVARS(15)
BB7=SVARS(16)
BB8=SVARS(17)

WRITE(*,2000) KBB2,BB3,BB4,BB5,BB6,BB7,BB8
2000 Format(I3," ",F10.6," ",F6.2," ",F6.3," ",F6.3," ",F6.3," ",F6.3)

END IF

DO 100 K1=1,NDOFEL
R_F(K1)=0.0D0
DO 110 KRHS=1,NRHS
RHS(K1,KRHS)=0.0D0
110  CONTINUE
DO 120 K2=1,NDOFEL
AMATRX(K2,K1)=0.0D0
R_MATRX(K2,K1)=0.0D0
120  CONTINUE
100  CONTINUE

C  READ THE STATE VARIABLES
C  SYMBOL(1)>=1.0 ==> 1ST LUMPED POINT HAS BEEN "SEPARATED"
C  SYMBOL(2)>=1.0 ==> 2ND LUMPED POINT HAS BEEN "SEPARATED"

SYMBOL(1)=SVARS(1)
SYMBOL(2)=SVARS(2)
IDTF_1(1)=SVARS(23)
IDTF_2(1)=SVARS(24)
IDTF_1(2)=SVARS(25)
IDTF_2(2)=SVARS(26)
RR(1)=SVARS(27)
RR(2)=SVARS(28)

C  CURRENT COORDINATES FOR THE FOUR POINTS OF AN ELEMENT

C_COOR(1,1)=COORDS(1,1)+U(1)
C_COOR(2,1)=COORDS(2,1)+U(2)
C_COOR(1,2)=COORDS(1,2)+U(3)
C_COOR(2,2)=COORDS(2,2)+U(4)
C_COOR(1,3)=COORDS(1,3)+U(5)
```

```
C_COOR(2,3)=COORDS(2,3)+U(6)
C_COOR(1,4)=COORDS(1,4)+U(7)
C_COOR(2,4)=COORDS(2,4)+U(8)

THIK1_0=SQRT((COORDS(1,1)-COORDS(1,4))**2
1  +(COORDS(2,1)-COORDS(2,4))**2.0)
THIK2_0=SQRT((COORDS(1,2)-COORDS(1,3))**2
1  +(COORDS(2,2)-COORDS(2,3))**2.0)

THIK(1) = THIK1_0
THIK(2) = THIK2_0

C  COMPUTE THE ROTATION ANGLE

P1_X=(C_COOR(1,1)+C_COOR(1,4))/2.0D0
P1_Y=(C_COOR(2,1)+C_COOR(2,4))/2.0D0
P2_X=(C_COOR(1,2)+C_COOR(1,3))/2.0D0
P2_Y=(C_COOR(2,2)+C_COOR(2,3))/2.0D0

ALEN=SQRT((P1_X-P2_X)**2.0D0 + (P1_Y-P2_Y)**2.0D0)
C ELEMENT LENGTH

IF((P2_Y-P1_Y).GE. 0.0D0) THEN

THETA= ACOS((P2_X - P1_X)/ALEN)

ELSE
THETA=-ACOS((P2_X - P1_X)/ALEN)

ENDIF

COS_PI = COS(THETA)
SIN_PI = SIN(THETA)

C  COORDINATES TRANSFORMATION

R_COOR(1,1)= C_COOR(1,1)*COS_PI+C_COOR(2,1)*SIN_PI
R_COOR(2,1)=-C_COOR(1,1)*SIN_PI+C_COOR(2,1)*COS_PI
R_COOR(1,2)= C_COOR(1,2)*COS_PI+C_COOR(2,2)*SIN_PI
R_COOR(2,2)=-C_COOR(1,2)*SIN_PI+C_COOR(2,2)*COS_PI
R_COOR(1,3)= C_COOR(1,3)*COS_PI+C_COOR(2,3)*SIN_PI
R_COOR(2,3)=-C_COOR(1,3)*SIN_PI+C_COOR(2,3)*COS_PI
R_COOR(1,4)= C_COOR(1,4)*COS_PI+C_COOR(2,4)*SIN_PI
```

```
R_COOR(2,4)=-C_COOR(1,4)*SIN_PI+C_COOR(2,4)*COS_PI

C  COMPUTE THE RELATIVE DISPLACEMENTS
C IN LOCAL COORDINATE SYSTEM

UX(1) = R_COOR(1,4) - R_COOR(1,1) !U(7)-U(1)
UX(2) = R_COOR(1,3) - R_COOR(1,2) !U(5)-U(3)
UY(1) = R_COOR(2,4) - R_COOR(2,1) - THIK1_0 !U(8)-U(2)
UY(2) = R_COOR(2,3) - R_COOR(2,2) - THIK2_0 !U(6)-U(4)

C  THE NODE FORCES AND STIFF MATRIX IS INTEGRATED
C USING 2 POINT LUMPED QUADRATURE SCHEME

CI(1) =-1.0D0 !LUMPED INTEGRATION POINT1
CI(2) = 1.0D0 !LUMPED INTEGRATION POINT2
C(1) =-1.0D0
C(2) = 1.0D0

DO 200 I=1, 2

UY_P(I) = 0.0D0
UX_P(I) = 0.0D0

DO 210 J=1, 2

!Jth INTERPOLATION FUNCTION EVALUATED IN Ith LUMPED POINT
PHI(J,I)= (1.0D0+C(J)*CI(I))/2.0D0
!RELATIVE DISPLACEMENT EVALUATED IN Ith LUMPED POINT
UY_P(I) = UY_P(I) + PHI(J,I)*UY(J)
UX_P(I) = UX_P(I) + PHI(J,I)*UX(J)
210  CONTINUE

C  CALCULATE THE NORMAL COHESIVE STRESS, SLOPE AND
C ENERGY RELEASE RATE IN Ith LUMPED POINT

CALL NOR(SN1,SN2,DLTN1,DLTN2,DLTNC,UY_P(I),
1 STRN(I),SKNN(I),G_I(I))

C  CALCULATE THE SHEAR COHESIVE STRESS, SLOPE AND
C ENERGY RELEASE RATE IN Ith LUMPED POINT

CALL SHR(ST1,ST2,DLTT1,DLTT2,DLTTC,UX_P(I),
1 STRT(I),SKTT(I),G_II(I))
```

```
C  FAILURE CRITERION IN Ith LUMPED POINT

F_CRT(I)=G_I(I)/G_I0 + G_II(I)/G_II0

CCCCCCCCCCCCCCCCCCCCCCCCCCCCCCCCCCCCCCCCCCCCCCCCCCCCCCCCCCCCCCCCCCCCCCC

C ENERGY OVERSHOOT IN Ith LUMPED POINT

OVER_SHT(I) = G_I(I)-THLD
PROB = DT2*SINH((OVER_SHT(I))/0.30D0)

C CALL RANDOM_SEED()
C CALL init_random_seed()
CALL RANDOM_NUMBER(HARVEST=R_VAR)

RR(I)=R_VAR

C IF THE STATUS IS (2,0), THEN LET IT BE (2,2).
IF(IDTF_1(I) .GE. 1.0D0) THEN
IDTF_1(I)=2.0D0
IDTF_2(I)=2.0D0
END IF

C 1) IN THE LODADING STEP, ALWAYS (0,0)
C 2) IN THE HOLDING STEP, IF STATUS IS (2,2), DO NOTHING
C 3) IF THE STATUS IS (0,0), THEN COMPARE R_VAR AND PROB
C 4) IF R_VAR < PROB, THEN (0,0) -> (2,0)
C 5) OTHERWISE, (0,0) -> (0,0)
IF(KSTEP .EQ. 1) THEN
IDTF_1(I)=0.0D0
IDTF_2(I)=0.0D0
ELSE IF (IDTF_1(I) .GE. 1.0D0) THEN
IDTF_1(I)=2.0D0
IDTF_2(I)=2.0D0
ELSE IF (R_VAR .LE. PROB) THEN
IDTF_1(I)=2.0D0
IDTF_2(I)=0.0D0
ELSE
IDTF_1(I)=0.0D0
IDTF_2(I)=0.0D0
END IF
```

```
C 1) IF SYMBOL=2, THEN SYMBOL=2
C 2) IF (2,2), THEN SYMBOL=2
C 3) IF (2,0) OR (0,0), THEN SYMBOL=0

IF(SYMBOL(I) .GE. 1.0D0) THEN
SYMBOL(I) = 2.0D0
ELSE IF(IDTF_2(I) .GE. 1.0D0) THEN
SYMBOL(I)=2.0D0
ELSE
SYMBOL(I)=0.0D0
END IF

CCCCCCCCCCCCCCCCCCCCCCCCCCCCCCCCCCCCCCCCCCCCCCCCCCCCCCCCCCCCCCCCCCCCCCC

C  Ith LUMPED POINT HAVE BEEN "SEPARATED"
C  PREVENT "BROKEN" ELEMENTS FROM BEING INVOLVED AGAIN

C IF((SYMBOL(I) .LE. 1.0D0)) THEN
C SYMBOL(I)=F_CRT(I)
C END IF

200 CONTINUE

DO 300 I=1,2
C  IF ONE OF THE LUMPED POINT IS BROKEN

IF(SYMBOL(I) .GE. 1.0D0) THEN
STRT(I) = 0.0D0
STRN(I) = 0.0D0
SKTT(I) = 0.0D0
SKNN(I) = 0.0D0

C  AVOID INTERPENETRATION IN LUMPED POINT

IF( UY_P(I) .LE. -1.0D-6) THEN
!NODES I HAVE BEEN "INTERPENETRATED"
STRN(I) = SK*UY_P(I)
SKNN(I) = SK
SYMBOL(I)= 10.0D0
END IF
END IF
300  CONTINUE
```

```
DO 400 I=1,2
FN(I) = 0.0D0
FT(I) = 0.0D0
DO 410 J=1,2
FN(I) = FN(I)+PHI(I,J)*STRN(J)*ALEN/2.0D0
FT(I) = FT(I)+PHI(I,J)*STRT(J)*ALEN/2.0D0
STFN(I,J) = 0.0D0
STFT(I,J) = 0.0D0
DO 420 K=1,2
STFN(I,J) = STFN(I,J)+PHI(I,K)*PHI(J,K)*SKNN(K)*ALEN/2.0D0
STFT(I,J) = STFT(I,J)+PHI(I,K)*PHI(J,K)*SKTT(K)*ALEN/2.0D0
420  CONTINUE
410  CONTINUE

C  MODIFIED TANGENTIAL STIFFNESS

IF (STFN(I,I) .LT. 0.0D0) THEN
STFN(I,I) = 0.0D0
END IF
IF (STFT(I,I) .LT. 0.0D0) THEN
STFT(I,I) = 0.0D0
END IF
400  CONTINUE

C  LOCAL STIFFNESS MATRIX AND RESIDUE FORCE VECTOR
DO 500 I = 1, 2
DO 510 J = 1, 2
C  LOCAL STIFFNESS MATRIX
R_MATRX(2*(I-1)+1, 2*(J-1)+1) = STFT(I,J)
R_MATRX(2*(I-1)+2, 2*(J-1)+2) = STFN(I,J)

R_MATRX(2*(4-I)+1, 2*(J-1)+1) =-STFT(I,J)
R_MATRX(2*(4-I)+2, 2*(J-1)+2) =-STFN(I,J)

R_MATRX(2*(I-1)+1, 2*(4-J)+1) =-STFT(I,J)
R_MATRX(2*(I-1)+2, 2*(4-J)+2) =-STFN(I,J)

R_MATRX(2*(4-I)+1, 2*(4-J)+1) = STFT(I,J)
R_MATRX(2*(4-I)+2, 2*(4-J)+2) = STFN(I,J)
510  CONTINUE
C  LOCAL RESIDUE FORCE VECTOR
R_F(2*(I-1)+1) = FT(I)
R_F(2*(4-I)+1) =-FT(I)
```

```
R_F(2*(I-1)+2) = FN(I)
R_F(2*(4-I)+2) =-FN(I)
C  UPDATE INTERNAL VARIABLES
SVARS(I) =SYMBOL(I)
500  CONTINUE

C  CCZM: factors

DK=THIK(1)/ALEN
ADK=-UX_P(1)/ALEN
ADK2=-UX_P(2)/ALEN

C  IF ONE OF THE LUMPED POINT IS BROKEN
IF((SYMBOL(1) .GE. 1.0D0).OR.(SYMBOL(2) .GE. 1.0D0)) THEN
DK = 0.0D0
ADK = 0.0D0
ADK2 = 0.0D0
IF( UY_P(I) .LE. -1.0D-6) THEN
ADK=-UX_P(1)/ALEN
ADK2=-UX_P(2)/ALEN
END IF
END IF

C  CCZM: BALANCING THE MOMENT EFFECTS

R_MATRX(2,1)=DK*SKTT(1)*ALEN/2.0D0
R_MATRX(2,7)=-DK*SKTT(1)*ALEN/2.0D0
R_MATRX(4,1)=-DK*SKTT(1)*ALEN/2.0D0
R_MATRX(4,7)=DK*SKTT(1)*ALEN/2.0D0

R_MATRX(8,3)=DK*SKTT(2)*ALEN/2.0D0
R_MATRX(8,5)=-DK*SKTT(2)*ALEN/2.0D0
R_MATRX(6,3)=-DK*SKTT(2)*ALEN/2.0D0
R_MATRX(6,5)=DK*SKTT(2)*ALEN/2.0D0

R_F(2)=R_F(2)+DK*FT(1)
R_F(4)=R_F(4)-DK*FT(1)
R_F(6)=R_F(6)-DK*FT(2)
R_F(8)=R_F(8)+DK*FT(2)

R_MATRX(2,2)=R_MATRX(2,2)+ADK*SKNN(1)*ALEN/2.0D0
R_MATRX(2,8)=R_MATRX(2,8)-ADK*SKNN(1)*ALEN/2.0D0
R_MATRX(4,2)=R_MATRX(4,2)-ADK*SKNN(1)*ALEN/2.0D0
```

```
R_MATRX(4,8)=R_MATRX(4,8)+ADK*SKNN(1)*ALEN/2.0D0

R_MATRX(8,4)=R_MATRX(8,4)+ADK2*SKNN(2)*ALEN/2.0D0
R_MATRX(8,6)=R_MATRX(8,6)-ADK2*SKNN(2)*ALEN/2.0D0
R_MATRX(6,4)=R_MATRX(6,4)-ADK2*SKNN(2)*ALEN/2.0D0
R_MATRX(6,6)=R_MATRX(6,6)+ADK2*SKNN(2)*ALEN/2.0D0

R_F(2)=R_F(2)+ADK*FN(1)
R_F(4)=R_F(4)-ADK2*FN(1)
R_F(6)=R_F(6)-ADK2*FN(2)
R_F(8)=R_F(8)+ADK*FN(2)

C  OUTPUT THE CRACK LENGTH AS THE CZ ELEMENT IS BROKEN

SVARS(3)=DT2
SVARS(6)=G_I(1)
SVARS(7)=G_II(1)
SVARS(21)=STRN(1)
SVARS(22)=STRT(1)
SVARS(5)=KINC
SVARS(16)=ATAN2(SQRT(G_II(1)),SQRT(G_I(1)))*180.0D0/3.14D0
IF ((AA.LT.1.0D0).AND.(SYMBOL(1).GE.1.0D0)) THEN

AC=100.0

SVARS(11)=AK
SVARS(12)=DT
SVARS(13)=X1
SVARS(14)=AG1
SVARS(15)=AG2
!SVARS(17)=G_II(1)

ELSE

AC=1.0

END IF
C  IF ELEMENT HAS FAILED, ASSIGN A 0 TO SDV(17)
IF (F_CRT(1).GE.1.0D0) THEN
SVARS(17)=F_CRT(1)
ELSE
SVARS(17)=F_CRT(1)
END IF
```

```
SVARS(10)=AC
SVARS(18)=STRT(1)
SVARS(19)=UY_P(1)
SVARS(20)=UX_P(1)
SVARS(23)=IDTF_1(1)
SVARS(24)=IDTF_2(1)
SVARS(25)=IDTF_1(2)
SVARS(26)=IDTF_2(2)
SVARS(27)=RR(1)
SVARS(28)=RR(2)

C  FORM THE GLOBAL STIFFNESS MATRIX AND RESIDUAL FORCE
DO 600 I=1,7,2
DO 610 J=1,7,2
AMATRX( I, J) = R_MATRX( I, J)*COS_PI**2.0D0 +
1  R_MATRX(I+1,J+1)*SIN_PI**2.0D0 -
2  R_MATRX( I,J+1)*SIN_PI*COS_PI -
3  R_MATRX(I+1, J)*SIN_PI*COS_PI

AMATRX(I+1, J) = R_MATRX( I, J)*SIN_PI*COS_PI -
1  R_MATRX(I+1,J+1)*SIN_PI*COS_PI -
2  R_MATRX( I,J+1)*SIN_PI**2.0D0 +
3  R_MATRX(I+1, J)*COS_PI**2.0D0

AMATRX( I,J+1) = R_MATRX( I, J)*SIN_PI*COS_PI -
1  R_MATRX(I+1,J+1)*SIN_PI*COS_PI +
2  R_MATRX( I,J+1)*COS_PI**2.0D0 -
3  R_MATRX(I+1, J)*SIN_PI**2.0D0

AMATRX(I+1,J+1) = R_MATRX( I, J)*SIN_PI**2.0D0 +
1  R_MATRX(I+1,J+1)*COS_PI**2.0D0 +
2  R_MATRX( I,J+1)*SIN_PI*COS_PI +
3  R_MATRX(I+1, J)*SIN_PI*COS_PI

610  CONTINUE
RHS(I ,1)= R_F(I)*COS_PI - R_F(I+1)*SIN_PI
RHS(I+1,1)= R_F(I)*SIN_PI + R_F(I+1)*COS_PI
600  CONTINUE

RETURN
END
```

```
C  CALCULATE THE NORMAL COHESIVE STRESS, SLOPE AND
C ENERGY RELEASE RATE IN Ith LUMPED POINT
SUBROUTINE NOR(SN1,SN2,DLTN1,DLTN2,DLTNC,UY,STRN,SKN,G_I)
IMPLICIT DOUBLE PRECISION(A-H, O-Z)
SN0 = 0.0D0
SN3 = 0.0D0
DLTN0= 0.0D0
SKN1 = (SN1-SN0)/(DLTN1-DLTN0)
SKN2 = (SN2-SN1)/(DLTN2-DLTN1)
SKN3 = (SN3-SN2)/(DLTNC-DLTN2)
STRN = 0.0D0
SKN = 0.0D0
G_I = 0.0D0
C0 = DLTN1*1.0D-3

IF(UY .LE. C0) THEN
STRN = UY*SKN1
SKN = SKN1
G_I = 0.0D0
ENDIF

IF((UY .GT. C0) .AND. (UY .LE. DLTN1)) THEN
STRN = UY*SKN1
SKN = SKN1
G_I = 0.5D0*SKN1*UY*UY
ENDIF
c  write(*,*) UY,DLTN1
IF((UY .GT. DLTN1).AND.(UY .LE. DLTN2)) THEN
STRN = SN1+SKN2*(UY-DLTN1)
SKN = SKN2
G_I = 0.5D0*(SN0+SN1)*(DLTN1-DLTN0)
1  +0.5D0*(SN1+STRN)*(UY -DLTN1)
ENDIF

IF((UY .GT. DLTN2).AND.(UY .LE. DLTNC)) THEN
STRN = SN2+SKN3*(UY-DLTN2)
SKN = SKN3
G_I = 0.5D0*(SN0+SN1)*(DLTN1-DLTN0)
1  +0.5D0*(SN1+SN2)*(DLTN2-DLTN1)
2  +0.5D0*(SN2+STRN)*(UY -DLTN2)
ENDIF

C  IF BROKEN WRT MODE I, SET G_I TO G_I0
```

```
IF(UY .GT. DLTNC) THEN
STRN = 0.0D0
SKN = 0.0D0
G_I = SN1*DLTNC
ENDIF

RETURN
END

C  CALCULATE THE SHEAR COHESIVE STRESS, SLOPE AND
C ENERGY RELEASE RATE IN Ith LUMPED POINT
SUBROUTINE SHR(ST1,ST2,DLTT1,DLTT2,DLTTC,UX,STRT,SKT,G_II)
IMPLICIT DOUBLE PRECISION(A-H, O-Z)

ST0 = 0.0D0
ST3 = 0.0D0
DLTT0= 0.0D0
SKT1 = (ST1-ST0)/(DLTT1-DLTT0)
SKT2 = (ST2-ST1)/(DLTT2-DLTT1)
SKT3 = (ST3-ST2)/(DLTTC-DLTT2)
STRT = 0.0D0
SKT = 0.0D0

IF(ABS(UX) .LE. DLTT1) THEN
STRT = UX*SKT1
SKT = SKT1
G_II = 0.5D0*SKT1*ABS(UX)*ABS(UX)
ENDIF

IF((ABS(UX) .GT. DLTT1).AND.(ABS(UX) .LE. DLTT2)) THEN
STRT =(ST1+SKT2*(ABS(UX)-DLTT1))*ABS(UX)/UX
SKT = SKT2
G_II = 0.5D0*(ABS(ST0)+ABS(ST1))*(DLTT1 -DLTT0)
1  +0.5D0*(ABS(ST1)+ABS(STRT))*(ABS(UX)-DLTT1)
ENDIF

IF((ABS(UX) .GT. DLTT2).AND.(ABS(UX) .LE. DLTTC)) THEN
STRT =(ST2+SKT3*(ABS(UX)-DLTT2))*ABS(UX)/UX
SKT = SKT3
G_II = 0.5D0*(ABS(ST0)+ABS(ST1))*(DLTT1 -DLTT0)
1  +0.5D0*(ABS(ST1)+ABS(ST2))*(DLTT2 -DLTT1)
2  +0.5D0*(ABS(ST2)+ABS(STRT))*(ABS(UX)-DLTT2)
ENDIF
```

```
C  IF BROKEN WRT MODE II, SET G_II TO G_II0
IF(ABS(UX) .GT. DLTTC) THEN
STRT = 0.0D0
SKT = 0.0D0
G_II = ST1*DLTTC
ENDIF

RETURN
END
```

A.2 User-defined element used in Chapter 4

```
CCCCCCCCCCCCCCCCCCCCCCCCCCCCCCCCCCCCCCCCCCCCCCCCCCCCCCCCCCCCCCCCCCCC
C UEL.f CCZM C
C C
C THIS SUBROUTINE WILL APPLY MIX-MODE TRAPEZOIDAL CZM C
C MODEL TO A USER DEFINED ELEMENT FOR USE BY ABAQUS. C
CCCCCCCCCCCCCCCCCCCCCCCCCCCCCCCCCCCCCCCCCCCCCCCCCCCCCCCCCCCCCCCCCCCC
SUBROUTINE UEL(RHS,AMATRX,SVARS,ENERGY,NDOFEL,NRHS,NSVARS,
1  PROPS,NPROPS,COORDS,MCRD,NNODE,U,DU,V,A,JTYPE,TIME,DTIME,
2  KSTEP,KINC,JELEM,PARAMS,NDLOAD,JDLTYP,ADLMAG,PREDEF,NPREDF,
3  LFLAGS,MLVARX,DDLMAG,MDLOAD,PNEWDT,JPROPS,NJPROP,PERIOD)

INCLUDE 'ABA_PARAM.INC'

DIMENSION RHS(MLVARX,*),AMATRX(NDOFEL,NDOFEL),PROPS(*),
1  SVARS(*),ENERGY(8),COORDS(MCRD,NNODE),U(NDOFEL),
2  DU(MLVARX,*),V(NDOFEL),A(NDOFEL),TIME(2),PARAMS(*),
3  JDLTYP(MDLOAD,*),ADLMAG(MDLOAD),DDLMAG(MDLOAD,*),
4  PREDEF(2,NPREDF,NNODE),LFLAGS(*),JPROPS(*)

DIMENSION C_COOR(2,4), R_COOR(2,4), R_F(8), R_MATRX(8,8),
1  UY(2),UX(2),UY_P(2),UX_P(2),CI(2),C(2),PHI(2,2),
2  STRN(2),STRT(2),SKNN(2),SKTT(2),SKNT(2),SKTN(2),FN(2),FT(2),
3  STFN(2,2),STFT(2,2),SYMBOL(2),F_CRT(2),G_I(2),G_II(2),THIK(2),
4 COUNTER_BREAK(2), COUNTER_LAW(2),
5 STRESS_TIME(2), STIME(2), IDTF_1(2), IDTF_2(2), OVER_SHT(2)

REAL*8 SN1, SN2, ST1, ST2, LAMBDAN1, LAMBDAN2, LAMBDAT1, LAMBDAT2
REAL*8 DLTN1, DLTN2, DLTNC, DLTT1, DLTT2, DLTTC, G_I0, G_II0
REAL*8 XN1, XN2, XT1, XT2, XAMBDAN1, XAMBDAN2, XAMBDAT1, XAMBDAT2
REAL*8 XLTN1, XLTN2, XLTNC, XLTT1, XLTT2, XLTTC, X_I0, X_II0
REAL*8 RR, RV, PROB, NUC_RATE, W_t, F_v, W_t_avg, R_Wt

CCCCCCCCCCCCCCCCCCCCCCCCCCCCCCCCCCCCCCCCCCCCCCCCCCCCCCCCCCCCCCCCCCCC
CCCCCCCCCCCCCCCCCCCCCCCCCCCCCCCCCCCCCCCCCCCCCCCCCCCCCCCCCCCCCCCCCCCC

C Tough cohesive properties
SN1 = 24.0000 !PEAK NORMAL STRESS
SN2 = SN1 !PEAK NORMAL STRESS
LAMBDAN1 = 0.00004800 !SHAPE PARAMETER LAMBDA1
LAMBDAN2 = 0.00050400 !SHAPE PARAMETER LAMBDA2
DLTNC = LAMBDAN2 !CRATICAL NORMAL DISPLACEMENT
DLTN1 = LAMBDAN1
```

```
DLTN2 = LAMBDAN2
G_I0 = 0.5D0*(SN1*DLTN2-SN2*DLTN1+SN2*DLTNC)

ST1 = SN1 !PEAK SHEAR STRESS
ST2 = SN2 !PEAK SHEAR STRESS
LAMBDAT1 = LAMBDAN1 !SHAPE PARAMETER LAMBDA1
LAMBDAT2 = LAMBDAN2 !SHAPE PARAMETER LAMBDA2
DLTTC = DLTNC !CRATICAL SHEAR DISPLACEMENT
DLTT1 = LAMBDAT1
DLTT2 = LAMBDAT2
G_II0 = 0.5D0*(ST1*DLTT2-ST2*DLTT1+ST2*DLTTC)
SK = SN1/DLTN1 ! STIFFNESS DURING INTERPENETRATION
FC = 0.0D0 ! FRICTION COEFFICIENT

C Brittle cohesive properties
XN1 = 48.0000 !PEAK NORMAL STRESS
XN2 = XN1 !PEAK NORMAL STRESS
XAMBDAN1 = 0.00009600 !SHAPE PARAMETER LAMBDA1
XAMBDAN2 = XAMBDAN1 !SHAPE PARAMETER LAMBDA2
XLTNC = XAMBDAN1 !CRATICAL NORMAL DISPLACEMENT
XLTN1 = XAMBDAN1
XLTN2 = XAMBDAN2
X_I0 = 0.5D0*(XN1*XLTN2-XN2*XLTN1+XN2*XLTNC)

XT1 = XN1 !PEAK SHEAR STRESS
XT2 = XN2 !PEAK SHEAR STRESS
XAMBDAT1 = XAMBDAN1 !SHAPE PARAMETER LAMBDA1
XAMBDAT2 = XAMBDAN2 !SHAPE PARAMETER LAMBDA2
XLTTC = XLTNC !CRATICAL SHEAR DISPLACEMENT
XLTT1 = XAMBDAT1
XLTT2 = XAMBDAT2
X_II0 = 0.5D0*(XT1*XLTT2-XT2*XLTT1+XT2*XLTTC)
XK = XN1/XLTN1 ! STIFFNESS DURING INTERPENETRATION
XC = 0.0D0 ! FRICTION COEFFICIENT

W_t_avg=16.0D0 ! NUCLEATION RATE (W_t/Stress=Prob)
F_v=36.0D0 ! POTENTIAL BARRIER: exp(-F_v/Stress^2)

IF ( KSETP .LT. 1.5 .AND. KINC .LT. 1.5 ) THEN
CALL RANDOM_NUMBER(HARVEST=R_Wt)
SVARS(27)=W_t_avg * R_Wt
END IF
```

```
IF ( KSTEP .LT. 1.5) THEN
SVARS(28)=SVARS(27)
END IF

CCCCCCCCCCCCCCCCCCCCCCCCCCCCCCCCCCCCCCCCCCCCCCCCCCCCCCCCCCCCCCCCCCCCCC
CCCCCCCCCCCCCCCCCCCCCCCCCCCCCCCCCCCCCCCCCCCCCCCCCCCCCCCCCCCCCCCCCCCCCC

(SEE APPENDIX A.1)
......
......
......
......

CCCCCCCCCCCCCCCCCCCCCCCCCCCCCCCCCCCCCCCCCCCCCCCCCCCCCCCCCCCCCCCCCCCCCC
CCCCCCCCCCCCCCCCCCCCCCCCCCCCCCCCCCCCCCCCCCCCCCCCCCCCCCCCCCCCCCCCCCCCCC

COUNTER_LAW(1)=SVARS(23) !LAW FOR THIS STEP
COUNTER_LAW(2)=SVARS(24) !LAW FOR THIS STEP
STRESS_TIME(1)=SVARS(25) !NUCLEATION
STRESS_TIME(2)=SVARS(26) !NUCLEATION
W_t=SVARS(28) !NUCLEATION RATE FOR THIS ELEMENT

COUNTER_BREAK(1)=SYMBOL(1) !COUNTER_BREAK INHERIT FROM LAST
COUNTER_BREAK(2)=SYMBOL(2) !COUNTER_BREAK INHERIT FROM LAST
STIME(1)=STRESS_TIME(1) !NUCLEATION
STIME(2)=STRESS_TIME(2) !NUCLEATION

CCCCCCCCCCCCCCCCCCCCCCCCCCCCCCCCCCCCCCCCCCCCCCCCCCCCCCCCCCCCCCCCCCCCCC
CCCCCCCCCCCCCCCCCCCCCCCCCCCCCCCCCCCCCCCCCCCCCCCCCCCCCCCCCCCCCCCCCCCCCC

(SEE APPENDIX A.1)
......
......
......
......

CCCCCCCCCCCCCCCCCCCCCCCCCCCCCCCCCCCCCCCCCCCCCCCCCCCCCCCCCCCCCCCCCCCCCC
CCCCCCCCCCCCCCCCCCCCCCCCCCCCCCCCCCCCCCCCCCCCCCCCCCCCCCCCCCCCCCCCCCCCCC

C CALCULATE STRESSES FROM THE CHOSEN LAW
C (1) IF COUNTER_LAW = 0.0, THEN TOUGH LAW
C (2) IF COUNTER_LAW = 2.0, THEN BRITTLE LAW
IF (COUNTER_LAW(I) .LE. 1.0D0) THEN !TOUGH MODE
```

```
CALL NOR(SN1,SN2,DLTN1,DLTN2,DLTNC,UY_P(I),STRN(I),SKNN(I),G_I(I))
CALL SHR(ST1,ST2,DLTT1,DLTT2,DLTTC,UX_P(I),STRT(I),SKTT(I),G_II(I))
F_CRT(I) = G_I(I)/G_I0 + G_II(I)/G_II0

ELSE

CALL NOR(XN1,XN2,XLTN1,XLTN2,XLTNC,UY_P(I),STRN(I),SKNN(I),G_I(I))
CALL SHR(XT1,XT2,XLTT1,XLTT2,XLTTC,UX_P(I),STRT(I),SKTT(I),G_II(I))
F_CRT(I) = G_I(I)/X_I0 + G_II(I)/X_II0

END IF

C JUDGING FAILURE
IF (COUNTER_BREAK(I) .GE. 1.0D0) THEN
COUNTER_BREAK(I) = 2.0D0
ELSE IF (F_CRT(I) .GE. 1.0D0) THEN
COUNTER_BREAK(I) = 2.0D0
ELSE
COUNTER_BREAK(I) = 0.0D0
END IF

C LET THE "SYMBOL" THE SAME AS "COUNTER_BREAK"
SYMBOL(I) = COUNTER_BREAK(I)

C ADDING TO THE STRESS_TIME COUNTER
IF (STRN(I) .GE. (XN1*0.001D0)) THEN
NUC_RATE = (W_t/STRN(I)) * EXP(-F_v/(STRN(I)**(2)))
STRESS_TIME(I) = STIME(I) + DTIME * NUC_RATE
END IF

STIME(I) = STRESS_TIME(I)

C SELECTING LAW FOR THE NEXT STEP
C IF STIME<1, IT FOLLOWS THE BRITTLE RULE (COUNTER_LAW=2.0)
IF (STIME(I) .LE. 1.0D0) THEN
COUNTER_LAW(I)=2.0D0 !BRITTLE
ELSE
COUNTER_LAW(I)=0.0D0 !TOUGH
END IF

200  CONTINUE
```

```
CCCCCCCCCCCCCCCCCCCCCCCCCCCCCCCCCCCCCCCCCCCCCCCCCCCCCCCCCCCCCCCCCCCC
CCCCCCCCCCCCCCCCCCCCCCCCCCCCCCCCCCCCCCCCCCCCCCCCCCCCCCCCCCCCCCCCCCCC

C IF ONE SYMBOL IS IN TOUGH MODE, THEN BOTH IN TOUGH MODE
IF ((COUNTER_LAW(1).LE.1.0).OR.(COUNTER_LAW(2).LE.1.0)) THEN
COUNTER_LAW(1)=0.0D0
COUNTER_LAW(2)=0.0D0
END IF

C IF ONE SYMBOL IS GREATER THAN 1.0, THEN LET BOTH BREAK
IF ((SYMBOL(1) .GE. 1.0D0) .OR. (SYMBOL(2) .GE. 1.0D0)) THEN
SYMBOL(1)=2.0D0
SYMBOL(2)=2.0D0
END IF

CCCCCCCCCCCCCCCCCCCCCCCCCCCCCCCCCCCCCCCCCCCCCCCCCCCCCCCCCCCCCCCCCCCC
CCCCCCCCCCCCCCCCCCCCCCCCCCCCCCCCCCCCCCCCCCCCCCCCCCCCCCCCCCCCCCCCCCCC

(SEE APPENDIX A.1)
......
......
......
......
```

BIBLIOGRAPHY

[1] A. A. Griffith. Vi. the phenomena of rupture and flow in solids. *Philosophical Transactions of the Royal Society of London A: Mathematical, Physical and Engineering Sciences*, 221(582-593):163–198, 1921.

[2] D. S. Dugdale. Yielding of steel sheets containing slits. *Journal of the Mechanics and Physics of Solids*, 8(2):100–104, 1960.

[3] G. I. Barenblatt. The mathematical theory of equilibrium cracks in brittle fracture. *Advances in Applied Mechanics*, 7:55–129, 1962.

[4] J. R. Willis. A comparison of the fracture criteria of griffith and barenblatt. *Journal of the Mechanics and Physics of Solids*, 15(3):151–162, 1967.

[5] J. R. Rice. A path independent integral and the approximate analysis of strain concentration by notches and cracks. *Journal of Applied Mechanics*, 35(2):379–386, 1968.

[6] J. R. Rice. Mathematical analysis in the mechanics of fracture. *Fracture: An Advanced Treatise*, 2:191–311, 1968.

[7] H. E. Andrews and A. J. Kinloch. Mechanics of adhesive failure. I. *Proceedings of the Royal Society of London A: Mathematical, Physical and Engineering Sciences*, 332(1590):385–399, 1973.

[8] R. J. Chang and A. N. Gent. Effect of interfacial bonding on the strength of adhesion of elastomers. I. Self-adhesion. *Journal of Polymer Science*, 19:1619–1633, 1981.

[9] J. G. Williams. *Fracture Mechanics of Polymers*. Ellis Horwood, Chichester, UK, 1984.

[10] J. G. Williams. Transient effects during rapid crack propagation. *International Journal of Fracture*, 93(1-4):51–61, 1998.

[11] C. M. Landis, T. Pardoen and J. W. Hutchinson. Crack velocity dependent toughness in rate dependent materials. *Mechanics of materials*, 32(11):663–678, 2000.

[12] P. Rahulkumar, A. Jagota, S. J. Bennison and S. Saigal. Cohesive element modeling of viscoelastic fracture: application to peel testing of polymers. *International Journal of Solids and Structures*, 37(13):1873–1897, 2000.

[13] A. C. F. Cocks and M. F. Ashby. The growth of a dominant crack in a creeping material. *Scripta Metallurgica*, 16:109–114, 1982.

[14] M. D. Thouless, C. H. Hsueh and A. G. Evans. A damage model of creep crack growth in polycrystals. *Acta Metallurgica*, 31(10):1675–1687, 1983.

[15] C. Y. Hui and V. Banthia. The extension of cracks at high temperature by growth and coalescence of voids. *International Journal of Fracture*, 25(1):53–67, 1984.

[16] D. Maugis. Subcritical crack growth, surface energy, fracture toughness, stick-slip and embrittlement. *Journal of Materials Science*, 20(9):3041–3073, 1985.

[17] K. Ravi-Chandar and M. Balzano. On the mechanics and mechanisms of crack growth in polymeric materials. *Engineering Fracture Mechanics*, 30(5):713–727, 1988.

[18] J. L. Bassani and D. E. Hawk. Influence of damage on crack-tip fields under small-scale-creep conditions. *International Journal of Fracture*, 42(2):157–172, 1990.

[19] H. Riedel. Creep crack growth under small-scale creep conditions. *International Journal of Fracture*, 42(2):173–188, 1990.

[20] T. W. Webb and E. C. Alfantis. Oscillatory fracture in polymeric materials. *International Journal of Solids and Structures*, 32(17-18):2725–2743, 1995.

[21] J. R. Rice. The mechanics of quasi-static crack growth. In R. E. Kelly, editor, *US. National Congress on Theoretical and Applied Mechanics*, pages 191–216. Western Periodicals Co., North Hollywood, CA, 1979.

[22] W. G. Knauss. Delayed failure - the Griffith problem for linearly viscoelastic materials. *International Journal of Fracture Mechanics*, 6(1):7–20, 1970.

[23] R. A. Schapery. A theory of crack initiation and growth in viscoelastic media I. Theoretical development. *International Journal of Fracture*, 11(1):141–159, 1975.

[24] R. A. Schapery. A theory of crack initiation and growth in viscoelastic media II. Approximate methods of analysis. *International Journal of Fracture*, 11(3):369–388, 1975.

[25] R. A. Schapery. A theory of crack initiation and growth in viscoelastic media III. Analysis of continuous growth. *International Journal of Fracture*, 11(4):549–562, 1975.

[26] H. Wang, W. Lu, J. R. Barber and M. D. Thouless. The roles of cohesive strength and toughness for crack growth in visco-elastic and creeping materials,. *Engineering Fracture Mechanics*, 160:226–237, 2016.

[27] S. M. Cox. A kinetic approach to the theory of the strength of glass. *Nature*, 162:947–949, 1948.

[28] S. M. Wiederhorn. Influence of water vapor on crack propagation in soda-lime glass. *Journal of the American Ceramic Society*, 50(8):407–414, 1967.

[29] S. M. Wiederhorn, H. Johnson, A. M. Diness, and A. H. Heuer. Fracture of glass in vacuum. *Journal of the American Ceramic Society*, 57(8):336–341, 1974.

[30] T. A. Michalske and S. W. Freiman. A molecular mechanism for stress corrosion in vitreous silica. *Journal of the American Ceramic Society*, 66(4):284–288, 1983.

[31] J. R. Rice. Thermodynamics of the quasi-static growth of griffith cracks. *Journal of the Mechanics and Physics of Solids*, 26(2):61–78, 1978.

[32] R. Thomson, C. Hsieh and V. Rana. Lattice trapping of fracture cracks. *Journal of Applied Physics*, 42(8):3154–3160, 1971.

[33] C. Hsieh and R. Thomson. Lattice theory of fracture and crack creep. *Journal of Applied Physics*, 44(5):2051–2063, 1973.

[34] B. R. Lawn. An atomistic model of kinetic crack growth in brittle solids. *Journal of Materials Science*, 10(3):469–480, 1975.

[35] B. R. Lawn. *Fracture of Brittle Solids*. Cambridge University Press, Cambridge, UK, 1993.

[36] J. L. Beuth Jr. Cracking of thin bonded films in residual tension. *International Journal of Solids and Structures*, 29(13):1657–1675, 1992.

[37] J. J. Vlassak. Channel cracking in thin films on substrates of finite thickness. *International Journal of Fracture*, 119(4):299–323, 2003.

[38] J. Du, M. D. Thouless and A. F. Yee. Development of a process zone in rubber-modified epoxy polymers. *International Journal of Fracture*, 92(3):271–286, 1998.

[39] J. Du, M. D. Thouless and A. F. Yee. Effects of rate on crack growth in a rubber-modified epoxy. *Acta materialia*, 48(13):3581–3592, 2000.

[40] C. Sun, M. D. Thouless, A. M. Waas, J. A. Schroeder and P. D. Zavattieri. Ductile-brittle transitions in the fracture of plastically-deforming, adhesively-bonded structures. part I: Experimental studies. *International Journal of Solids and Structures*, 45(10):3059–3073, 2008.

[41] C. Sun, M. D. Thouless, A. M. Waas, J. A. Schroeder and P. D. Zavattieri. Ductile-brittle transitions in the fracture of plastically-deforming, adhesively-bonded structures. part II: numerical studies. *International Journal of Solids and Structures*, 45(17):4725–4738, 2008.

[42] D. Quan, N. Murphy and A. Ivankovic. Fracture behaviour of epoxy adhesive joints modified with core-shell rubber nanoparticles. *Engineering Fracture Mechanics*, 182:566–576, 2017.

[43] D. L. Hunston and W. D. Bascom. *Failure behavior of rubber-toughened epoxies in bulk, adhesive, and composite geometries*, chapter 7, pages 83–99. 1984.

[44] M. E. Nichols and C. A. Peters. The effect of weathering on the fracture energy of hardcoats over polycarbonate. *Polymer Degradation and Stability*, 75(3):439–446, 2002.

[45] J. Dundurs. Edge-bonded dissimilar orthogonal elastic wedges. *Journal of Applied Mechanics*, 36:650–652, 1969.

[46] M. D. Thouless. Crack spacing in brittle films on elastic substrates. *Journal of the American Ceramic Society*, 73(7):2144–2146, 1990.

[47] M. D. Thouless, E. Olsson and A. Gupta. Cracking of brittle films on an elastic substrate. *Acta Metallurgica et Materialia*, 40(6):1287–1292, 1992.

[48] J. W. Hutchinson and Z. Suo. Mixed mode cracking in layered materials. *Advances in Applied Mechanics*, 29(63):191, 1992.

[49] V. B. Shenoy, A. F. Schwartzman and L. B. Freund. Crack patterns in brittle thin films. *International Journal of Fracture*, 103(1):1–17, 2000.

[50] M. D. Thouless, Z. Li, N. J. Douville and S. Takayama. Periodic cracking of films supported on compliant substrates. *Journal of the Mechanics and Physics of Solids*, 59(9):1927–1937, 2011.

[51] S. Takayama J. Huang, B. C. Kim and M. D. Thouless. The control of crack arrays in thin films. *Journal of Materials Science*, 49(1):255–268, 2014.

[52] R. Huang, J. H. Prévost and Z. Suo. Loss of constraint on fracture in thin film structures due to creep. *Acta Materialia*, 50(16):4137–4148, 2002.

[53] J. Liang, R. Huang, J. H. Prévost and Z. Suo. Thin film cracking modulated by underlayer creep. *Experimental Mechanics*, 43(3):269–279, 2003.

[54] A. S. Wineman and K. R. Rajagopal. *Mechanical Response of Polymers: An Introduction*. Cambridge University Press, Cambridge, UK, 2000.

[55] T. Y. Tsui, A. J. McKerrow and J. J. Vlassak. Constraint effects on thin film channel cracking behavior. *Journal of Materials Research*, 20(9):2266–2273, 2005.

[56] K. Kim, H. Luo, A. K. Singh, T. Zhu, S. Graham and O. N. Pierron. Environmentally assisted cracking in silicon nitride barrier films on poly(ethylene terephthalate) substrates. *ACS Applied Materials & Interfaces*, 8(40):27169–27178, 2016.

[57] K. Kim, S. Graham and O. N. Pierron. Note: A single specimen channel crack growth technique applied to brittle thin films on polymer substrates. *Review of Scientific Instruments*, 88(3):036102, 2017.

[58] M. W. Lane, J. M. Snodgrass and R. H. Dauskardt. Environmental effects on interfacial adhesion. *Microelectronics Reliability*, 41(9):1615–1624, 2001.

[59] J. J. Vlassak, Y. Lin and T. Y. Tsui. Fracture of organosilicate glass thin films: Environmental effects. *Materials Science and Engineering: A*, 391(1):159–174, 2005.

[60] E. P. Guyer and R. H. Dauskardt. Fracture of nanoporous thin-film glasses. *Nature Materials*, 3(1):53–57, 2004.

[61] R. F. Cook and E. G. Liniger. Kinetics of indentation cracking in glass. *Journal of the American Ceramic Society*, 76(5):1096–1105, 1993.

[62] Lexan™ 9034 product data sheet, 2012.

[63] M. Huang, Z. Suo and Q. Ma. Plastic ratcheting induced cracks in thin film structures. *Journal of the Mechanics and Physics of Solids*, 50(5):1079–1098, 2002.

[64] Z. Suo, J. J. Vlassak and S. Wagner. Micromechanics of macroelectronics. *China Particuology*, 3(6):321–328, 2005.

[65] D. R. Cairns and G. P. Crawford. Electromechanical properties of transparent conducting substrates for flexible electronic displays. *Proceedings of the IEEE*, 93(8):1451–1458, 2005.

[66] M. R. Begley and A. G. Evans. Progressive cracking of a multilayer system upon thermal cycling. *Journal of Applied Mechanics*, 68(4):513–520, 2000.

[67] M. Huang, Z. Suo, Q. Ma and H. Fujimoto. Thin film cracking and ratcheting caused by temperature cycling. *Journal of Materials Research*, 15(6):1239–1242, 2000.

[68] K. Kim, H. Luo,, T. Zhu, O. N. Pierron,, and S. Graham. Influence of polymer substrate damage on the time dependent cracking of sin x barrier films. *Scientific Reports*, 8(1):4560, 2018.

[69] R. B. Sills and M. D. Thouless. The effect of cohesive-law parameters on mixed-mode fracture. *Engineering Fracture Mechanics*, 109:353–368, 2013.

[70] R. B. Sills and M. D. Thouless. Cohesive-length scales for damage and toughening mechanisms. *International Journal of Solids and Structures*, 55:32–43, 2015.

[71] J. P. Parmigiani and M. D. Thouless. The effects of cohesive strength and toughness on mixed-mode delamination of beam-like geometries. *Engineering Fracture Mechanics*, 74(17):2675–2699, 2007.

[72] Q. D. Yang, M. D. Thouless and S. M Ward. Numerical simulations of adhesively-bonded beams failing with extensive plastic deformation. *Journal of the Mechanics and Physics of Solids*, 47:1337–1353, 1999.

[73] A. J. Kinloch and J. G. Williams. Crack blunting mechanisms in polymers. *Journal of Materials Science*, 15(4):987–996, 1980.

[74] K. Kim and J. Kim. Elasto-plastic analysis of the peel test for thin film adhesion. *Journal of Engineering Materials and Technology*, 110(3):266, 1988.

[75] A. J. Kinloch and M. L. Yuen. The mechanical behaviour of polyimide/copper laminates part 2: peel energy measurements. *The Journal of Adhesion*, 30(1-4):151–170, 1989.

[76] A. F. Yee, D. Li and X. Li. The importance of constraint relief caused by rubber cavitation in the toughening of epoxy. *Journal of Materials Science*, 28(23):6392–6398, 1993.

[77] A. J. Kinloch, S. J. Shaw, D. A. Tod and D. L. Hunston. Deformation and fracture behaviour of a rubber-toughened epoxy: 1. microstructure and fracture studies. *Polymer*, 24(10):1341–1354, 1983.

[78] A. F. Yee and R. A. Pearson. Toughening mechanisms in elastomer-modified epoxies. *Journal of Materials Science*, 21(7):2462–2474, 1986.

[79] A. C. Garg and Y. Mai. Failure mechanisms in toughened epoxy resinsa review. *Composites Science and Technology*, 31(3):179–223, 1988.

[80] R. Raj and M. F. Ashby. Intergranular fracture at elevated temperature. *Acta Metallurgica*, 23(6):653–666, 1975.

[81] R. Raj. Nucleation of cavities at second phase particles in grain boundaries. *Acta Metallurgica*, 26(6):995–1006, 1978.

[82] M. H. Yoo and H. Trinkaus. Crack and cavity nucleation at interfaces during creep. *Metallurgical and Materials Transactions A*, 14(3):547–561, 1983.

[83] Y. Huang and A. J. Kinloch. Modelling of the toughening mechanisms in rubber-modified epoxy polymers. *Journal of Materials Science*, 27(10):2753–2762, 1992.

[84] M. F. Kanninen. An augmented double cantilever beam model for studying crack propagation and arrest. *International Journal of Fracture*, 9(1):83–92, 1973.

[85] M. Ibnabdeljalil and S. L. Phoenix. Creep rupture of brittle matrix composites reinforced with time dependent fibers: scalings and monte carlo simulations. *Journal of the Mechanics and Physics of Solids*, 43(6):897–931, 1995.

[86] B. K. Atkinson. Subcritical crack growth in geological materials. *Journal of Geophysical Research: Solid Earth*, 89(B6):4077–4114, 1984.